A SLIDING MODE APPROACH TO CONTROL POWER SINKS AND POWER SOURCES IN DC-DC SWITCHING CONVERTERS

David Alejandro Zambrano Prada

UNIVERSITAT ROVIRA i VIRGILI

A sliding mode approach to control power sinks and power source in dc-dc switching converter

David Alejandro Zambrano Prada

DOCTORAL THESIS
2023

UNIVERSITAT ROVIRA I VIRGILI
A SLIDING MODE APPROACH TO CONTROL POWER SINKS AND POWER SOURCES IN DC-DC SWITCHING CONVERTERS
David Alejandro Zambrano Prada

David Alejandro Zambrano Prada

A sliding mode approach to control power sinks and power sources in dc-dc switching converters

Doctoral thesis
presented for the degree of
Doctor of Philosophy

Supervised by
Prof. Luis Martinez Salamero
Prof. Abdelali El Aroudi

Department of Electronic, Electric and Automatic Control Engineering

UNIVERSITAT ROVIRA i VIRGILI

Tarragona - Spain
2023

UNIVERSITAT ROVIRA I VIRGILI
A SLIDING MODE APPROACH TO CONTROL POWER SINKS AND POWER SOURCES IN DC-DC SWITCHING CONVERTERS
David Alejandro Zambrano Prada

UNIVERSITAT ROVIRA i VIRGILI

Departament d'Enginyeria Electrònica, Elèctrica i Automàtica
Avda. Països Catalans, 26 Campus Sescelades
43007 Tarragona, Spain
Tel.: + 34 977 55 96 10
Fax: + 34 977 55 96 05
Email: secelec@urv.cat

We state that the present study, entitled "**A sliding mode approach to control power sinks and power sources in dc-dc switching converters,**" presented by David Alejandro Zambrano Prada for the award of the degree of Doctor, has been caried out under our supervision at the Department of Electrical, Electronics and Automatic Control Engineering of this university.

Tarragona, 15th September 2023

Doctoral Thesis supervisor

Professor Luis Martinez Salamero.

Doctoral Thesis supervisor

Professor Abdelali El Aroudi.

UNIVERSITAT ROVIRA I VIRGILI
A SLIDING MODE APPROACH TO CONTROL POWER SINKS AND POWER SOURCES IN DC-DC SWITCHING CONVERTERS
David Alejandro Zambrano Prada

Acknowledgements

I would like to express my gratitude to my supervisors, Dr. Luis Martinez Salamero and Dr. Abdelali El Aroudi for letting me be part of their team and guiding me in the progress of this work. A special thanks to Dr. Luis, who, without him, this whole adventure would not have started and continued until the end. I have only words of gratitude for him.

For my family I have just love. I have left them behind in my country to advance in my professional career but I have never felt away from them. They have been here for me always. To my mother Maria, my father Helver, my siblings Camilo, Kevin and Sofia, thank you for everything.

Finally, I would like to thank with a hug to my mentor Oswaldo Lopez, without him I would not be here; to my colleagues Xavi Genero, Max Sebastiá and Marc Lázaro for the coffee talks and laughs; to Alexandra Blanc and Martín Gállego for letting me be a part of their education and guiding them; and to everyone that, due to bad memory or ingratitude, I do not mention here.

UNIVERSITAT ROVIRA I VIRGILI
A SLIDING MODE APPROACH TO CONTROL POWER SINKS AND POWER SOURCES IN DC-DC SWITCHING CONVERTERS
David Alejandro Zambrano Prada

Thesis written by David Alejandro Zambrano Prada.
A sliding mode approach to control power sinks and power sources in dc-dc switching converters.
Ph.D. in Technologies for Nanosystems, Bioengineering and Energy.

This reasearch has been funded by the Agencia de Gestio dAjuts Universitaris i de Recerca (AGAUR).
This work was supported by the Spanish Ministerio de Ciencia e Innovación under Grant PID2019-111443RB-I00 and Grant PID2020-120151RB-I00.

Table of Content

UNIVERSITAT ROVIRA I VIRGILI
A SLIDING MODE APPROACH TO CONTROL POWER SINKS AND POWER SOURCES IN DC-DC SWITCHING CONVERTERS
David Alejandro Zambrano Prada

List of Figures

List of Tables

Nomenclature

Acronyms

BOF	Boost with Output Filter
CC	Constant Current
CCL	Constant Current Load
CCM	Continuous Conduction Mode
$CPphase$	Constant Power Interval
CP	Constant Power
CPL	Constant Power Load
$CVphase$	Constant Voltage Interval
CV	Constant Voltage
DCM	Discontinuous Conduction Mode
EP	Equilibrium Point
EPL	Equilibrium Point Locus
ESM	Existence of Sliding Motions
EV	Electric Vehicle
$GNSL$	Generic Nonlinear Static Load
LFR	Loss-Free Resistor
MCC	Multistage Constant Current
MPP	Maximum Power Point
$MPPT$	Maximum Power Point Tracking
PET	Power Element Transformer
PFC	Power Factor Correction
$POPI$	Power Output Power Input
PRC	Parallel Resonant Converter
PV	Photovoltaic
PWM	Pulse-Width Modulation

$SCIM$	Squirrel Cage Induction Motor
$SLFR$	Series Loss-Free Resistor
SMC	Sliding Mode Control
SOC	State of Charge
SRC	Series Resonant Converter

Chapter 1

An introduction to the concept of power elements

DC-to-DC switching converters are variable structure systema that can be represented by a repetitive sequence of topological configurations; namely, 2 configurations for continuous conduction mode (CCM) or, 3 or more configurations for discontinuous conduction mode (DCM). When operating in CCM, they are often represented in compact form by an equivalent circuit where topology is equally valid to describe the switched in the average behavior of the converter, the difference being established by a control variable that can be a binary signal u taking 0 or 1 values in a continuous signal $\langle u \rangle$ corresponding to the average value of u.

The main elements of a circuit describing in compact form a switching power converter in CCM are the classical element found in linear circuit theory plus new elements that have emerged in power processing. The classical elements are the passive ones, i.e., resistor, inductor, and capacitor plus the ideal transformer. The controlled sources are not linear since the gain, i.e., the multiplicative factor is not a constant but a function of the control u. Due to the product of the controlling variable and the function of u, the resulting controlled source is of bilinear nature [1]. The exception of this modelling is the buck converter, which is strictly a linear system. In addition to the bilinear sources, there are two elements that specifically appear in power processing systems. They are

the constant power sink and the constant power source, which are represented respectively in Fig. 1.1a and Fig. 1.1b.

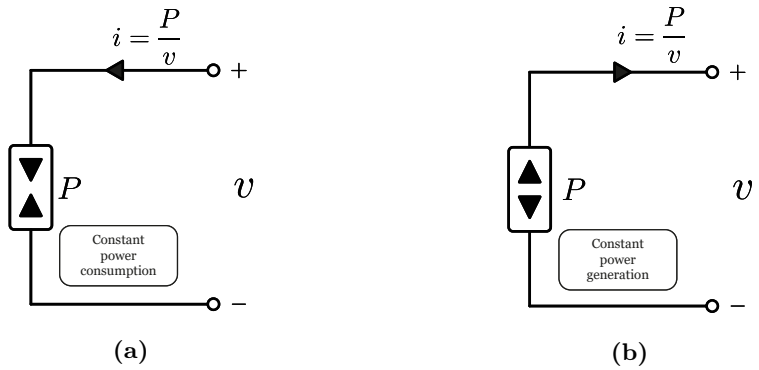

Fig. 1.1: Power elements. (a) Constant power sink and (b) Constant power source.

To summarize the peculiarity of the circuit-based modelling of power converters, Fig. 1.2 illustrates a compact representation of a boost converter feeding a constant power load (CPL), or constant power sink in our terminology. The circuit corresponds to a switched model assuming that variable u takes the values 1 and 0 during ON and OFF states respectively.

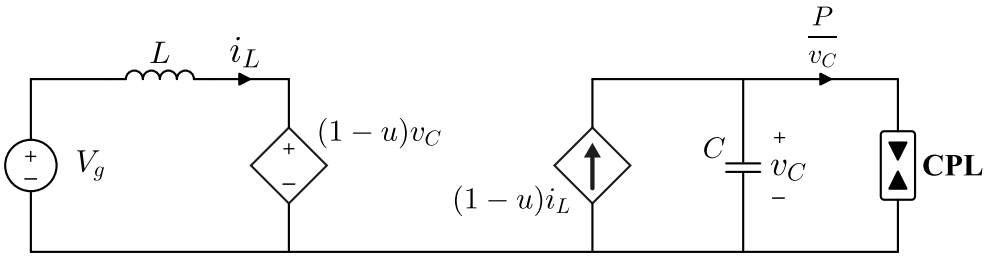

Fig. 1.2: Switched model of a boost converter supplying a CPL.

1.1 Power processing systems modelled by power elements

Power elements exhibit the natural behavior of sink or source in certain power processing applications, but they can be also the result of forced behavior in certain converters imposed by an appropriate control law.

1.1.1 Natural behavior

1.1.1.1 Power sinks

CPL behavior arises naturally in the cascaded connection of two converters with tight voltage regulation in the second converter. The first converter is referred to as source converter while the second one is named load converter as illustrated in Fig. 1.3. The cascade connection can be modelled as depicted in Fig 1.4 by modelling the load converter by means of a CPL [2], [3].

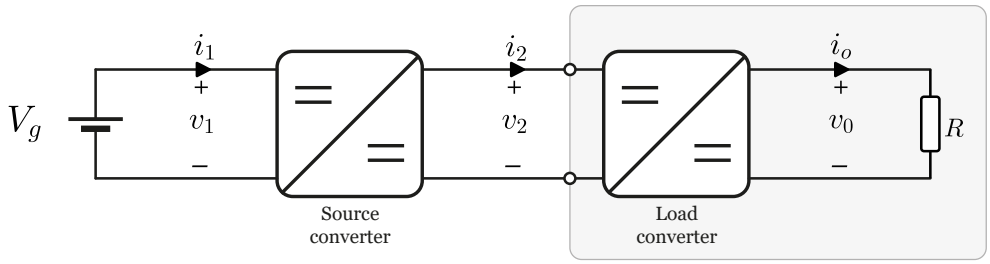

Fig. 1.3: Cascade connection of two converters.

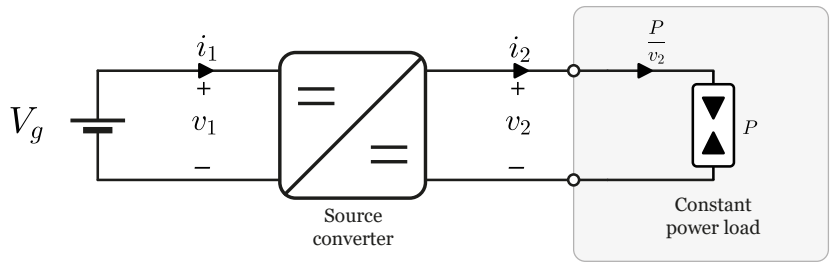

Fig. 1.4: Equivalent system of Fig. 1.3 when the load converter has tight voltage regulation.

CPL behavior also appears in the powertrain of an electric vehicle (EV) when the motor operates simultaneously at constant torque and constant speed, and therefore at constant mechanical power at the motor axis. The mechanical constant power is transmitted backwards to the output of the three-phase inverter depicted in Fig. 1.5, and then to the output of the bidirectional converter in the same figure. Hence, the DC bus of the powertrain supplies constant power to the inverter and can be modelled as shown in Fig. 1.6 [4]–[6].

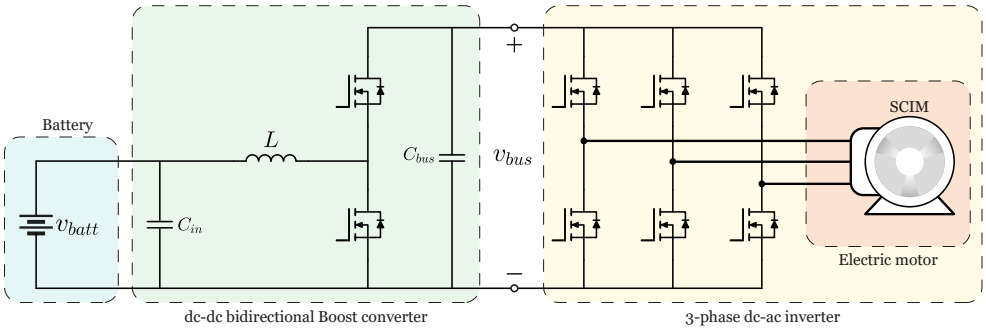

Fig. 1.5: Typical powertrain of an electric vehicle where SCIM stands for squirrel cage induction motor.

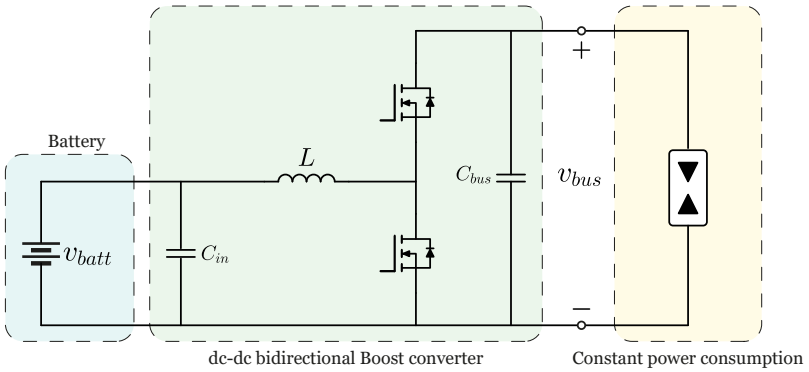

Fig. 1.6: Model of the dc port of the EV powertrain when the motor operates at constant torque - constant speed.

1.1.1.2 Power sources

Power source behavior arises in the output port of a buck-boost converter operating in DCM [7], [8]. The output port of the converter can be modelled by a virtual resistor because the steady-state values of input voltage and input current are proportional in DCM. Due to the POPI nature of the converter (P_{dc} input power = P_{dc} output power) [9], the power absorbed by the input port is totally transferred to the output port and modelled by a power source. Fig. 1.7 shows a buck-boost converter and Fig. 1.8 illustrates its behavior in DCM by means of a two-port representation, in which the input port is characterized by a virtual resistor where resistance is given by $R_e = 2Lf_s/D^2$, D being the duty cycle and f_s the switching frequency. The output port is modelled by a power source with $P = V_g^2/R_e$, i.e., the input power absorbed by the virtual resistor. The two-port of Fig. 1.8 is known as loss-free resistor (LFR) because

the input resistor is not a real resistive element, but it is rather a virtual one, and therefore there are no conduction losses in the conversion of energy [10].

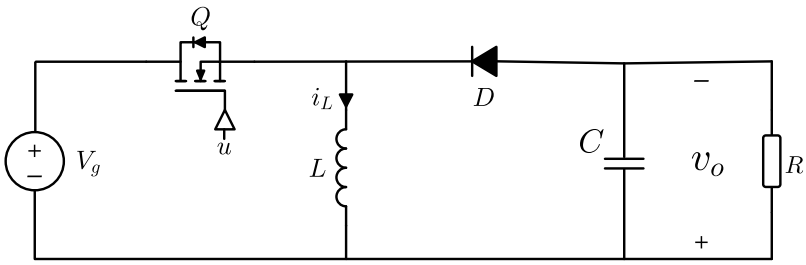

Fig. 1.7: Buck-boost converter.

The equivalent circuit shown in Fig. 1.8 corresponds to a parallel LFR because the virtual resistor and the power source are connected in parallel with input source and output load, respectively. A topological variation of the positive output voltage buck-boost converter shown in Fig. 1.9 result in the equivalent circuit depicted in Fig. 1.10 when the converter works in DCM. The model in Fig. 1.10 is denominated series loss-free resistor (SLFR) because the virtual resistance R_e is connected between the input and output ports and therefore has not ground connection [11]. The expression of the virtual resistance the same than the buck-boost converter, i.e., $R_e = 2Lf_s/D^2$.

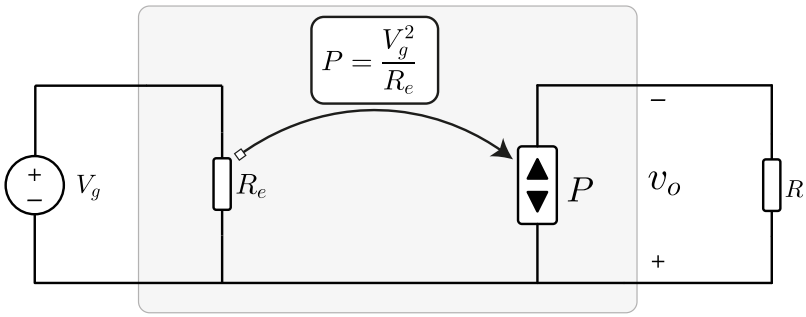

Fig. 1.8: LFR model of a buck-boost converter in steady-state and DCM.

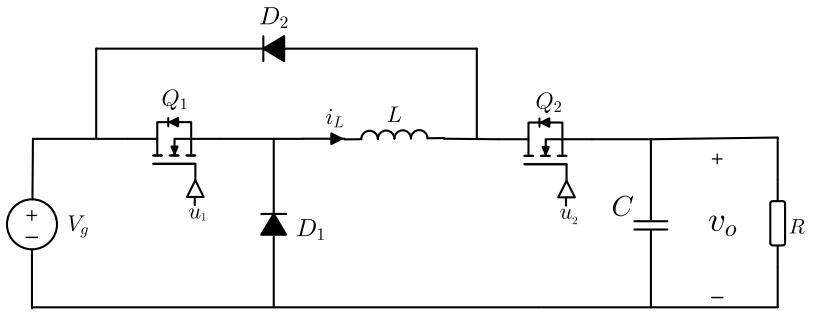

Fig. 1.9: Topological variation of the positive output voltage buck-boost converter.

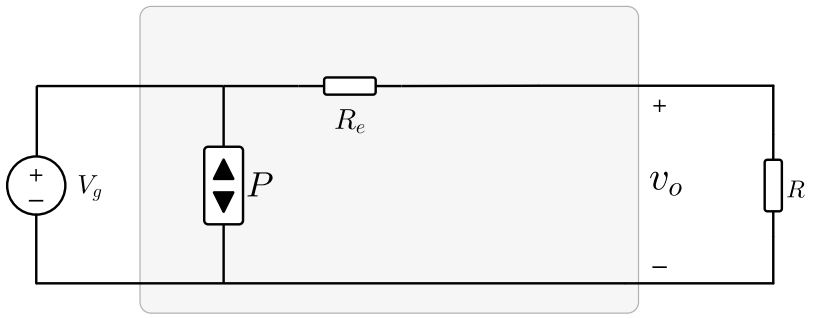

Fig. 1.10: SLFR model of the converter of Fig. 9 in steady-state and DCM.

1.1.2 Forced behavior (Synthesis)

1.1.2.1 Power element transformer

A power element transformer (PET) is a two-port circuit where input port is a power sink and its output port is a power source, the power ratio being one since the dc power input and dc power output are equal. Fig. 1.11 shows a PET terminated at a resistor, which is the results of the electronic implementation represent in Fig. 1.12. The block diagram in the figure corresponds to a generic dc-dc switching converter with an inductor L in series with the input port. The control law is implemented by a sliding mode regulation loop where switching surface $\Sigma = \{x|\ S(x) = 0\}$, when $S(x)$ is given by $S(x) = v_1 i_1 - P$ [12]. It is shown in [12] that the power sink-power source transformer can be synthetized in the boost, boost with output filter (BOF), Ćuk and SEPIC converters.

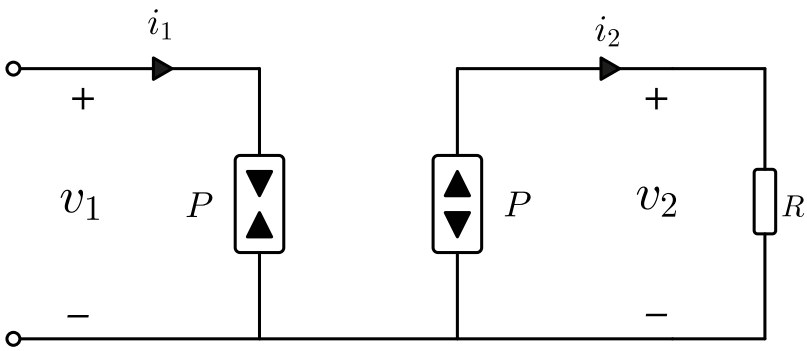

Fig. 1.11: PET model in steady-state terminated at a resistive load.

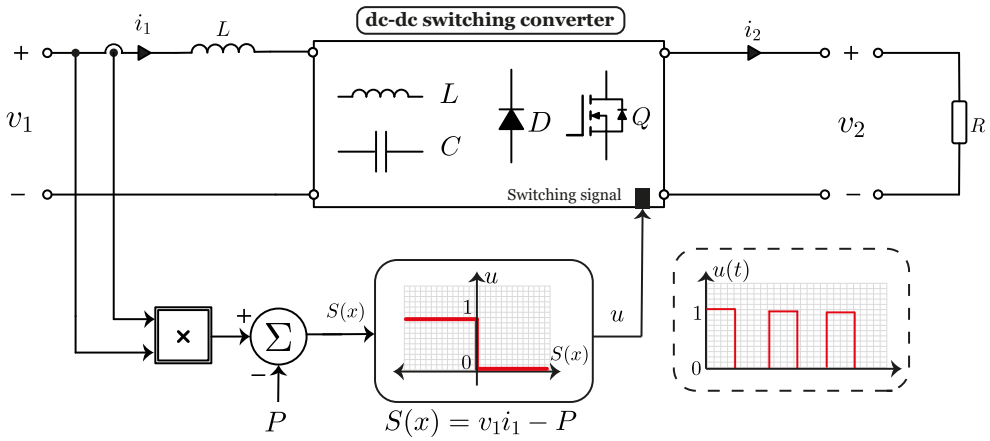

Fig. 1.12: Block diagram of a generic dc-dc switching converter with series inductor in the input port and SMC imposing a CPL behavior in such port.

1.1.2.2 LFR of parallel type

The naturally behavior of the buck-boost converter in DCM characterized by the LFR model of Fig. 1.9 can be also synthesized in the same converter with a series inductor in the input port above mentioned using the block diagram depicted in Fig. 1.13 [13]. The SMC imposes the proportionality between the input voltage and input current, which eventually results in the emulated resistor of the LFR.

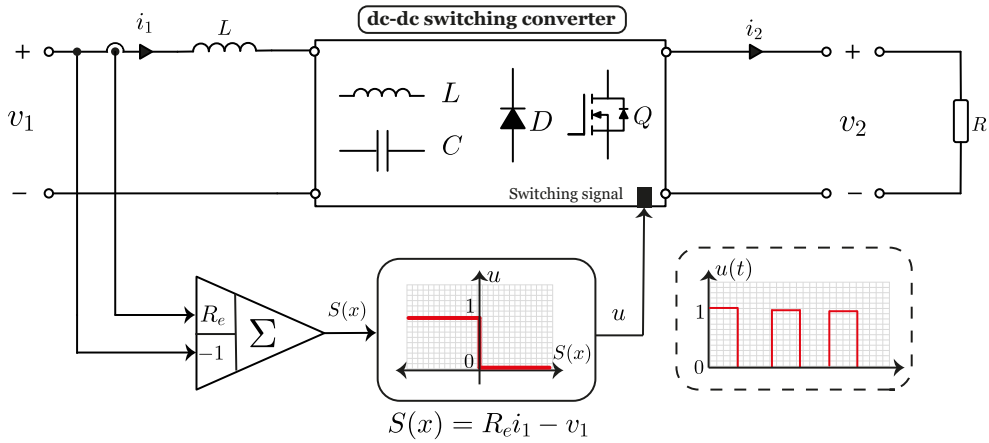

Fig. 1.13: Block diagram of a dc-dc switching converter with LFR characteristics imposed by SMC.

1.1.2.3 LFR of parallel type in self-oscillating resonant converters

In self-oscillating resonant converters, the change of polarity of the input square waveform is determined by the change of sign of the current in the inductor in series with the input port as illustrated in Fig. 1.14 [14]. As a result, the input current and the first harmonic of the input voltage are in phase, which ensures a unity power factor to the steady-state operation of the resonant converter.

This fact confers a nature of LFR of the type depicted in Fig. 1.8 to the series resonant converter (SRC), parallel resonant converter (PRC), LCC resonant converter, LLC resonant converter, and LCLC resonant converter [15].

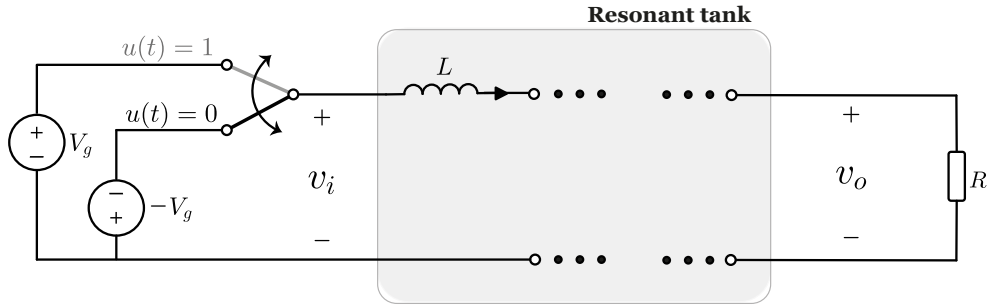

(a)

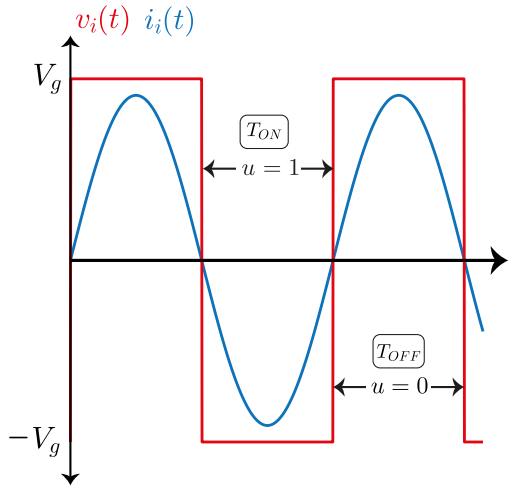

(b)

Fig. 1.14: (a) Operating principle of self-oscillating resonant converters with LFR characteristics; using $u = 1$ to $i_1 \leq 0$ and $u = 0$ to $i_1 < 0$ and (b) Steady state behavior.

1.1.2.4 Photovoltaic chain with maximum power point tracking

A basic photovoltaic (PV) chain consists in the cascade connection of a PV generator, a dc-dc power converter and a dc load as depicted in a Fig. 1.15 [16]. The control loop in the figure ensures the maximum power point tracking of the PV panel irrespective of the changes in solar irradiance or temperature [17]. The maximum power point (MPP) is characterized of the voltage and current coordinates (V_{MPP}, I_{MPP}) as illustrated in the voltage-current ($v - i$) and voltage-power ($v - p$) characteristics in the figure. The power P of MPP is completely transferred to the dc load due to the POPI nature of the converter. The steady-state operating point in the output port is characterized by the current and voltage coordinates given by (V_o^*, I_o^*), which corresponds to the intersection point of the $v_o - i_o$ characteristics of the MPPT controlled converter and the $v_o - i_o$ straight line representing the dc load. This is illustrated in Fig. 1.16 where the output port of the converter is modelled by a power source P and its corresponding $v_o - i_o$ characteristic curve is the hyperbola $v_o i_o = P$.

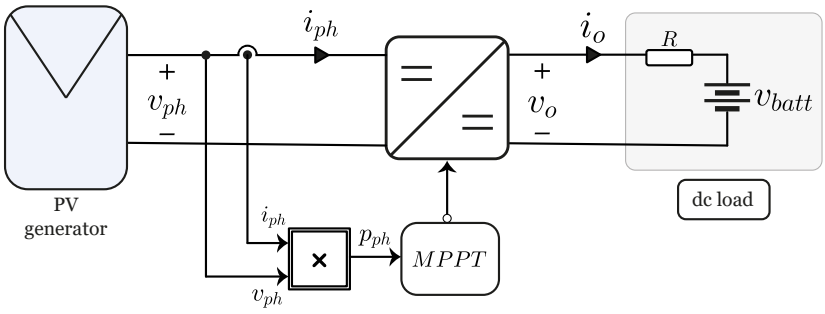

(a)

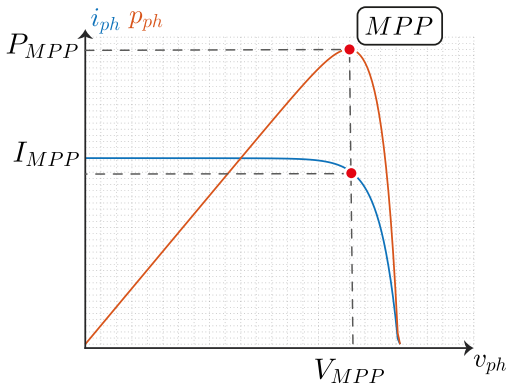

(b)

Fig. 1.15: (a) Basic PV chain with MPPT and (b) $v-i$ and $v-p$ curves of the PV generation.

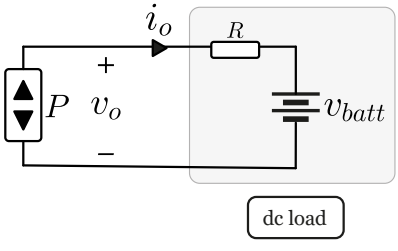

(a)

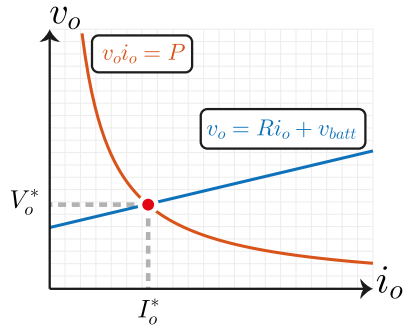

(b)

Fig. 1.16: Steady-state output port: (a) circuit model and (b) Operating point.

1.2 Association of power elements

1.2.1 Series connection

Power elements can be associated in series as illustrated in Fig. 1.17 for the particular case of power series connection. The result of the series connection is a power source where power is the sum of the power of each source.

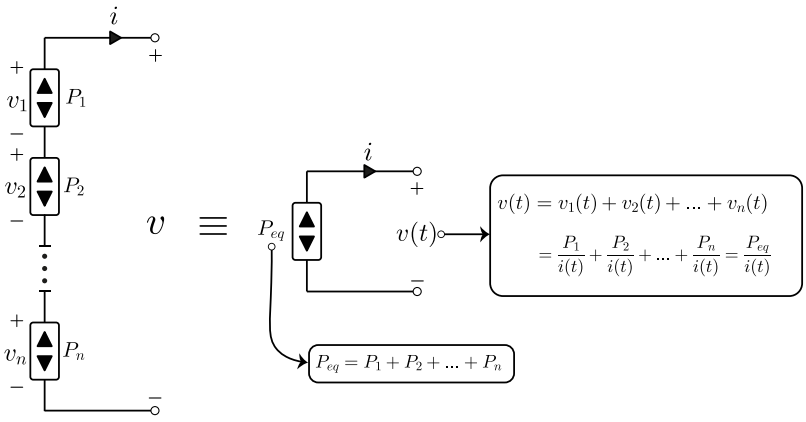

Fig. 1.17: Series connection of power sources.

The sum of the power is algebraic, so the series connection can present equally sinks or source or a combination of them as shown in Fig. 1.18 for the case of two elements.

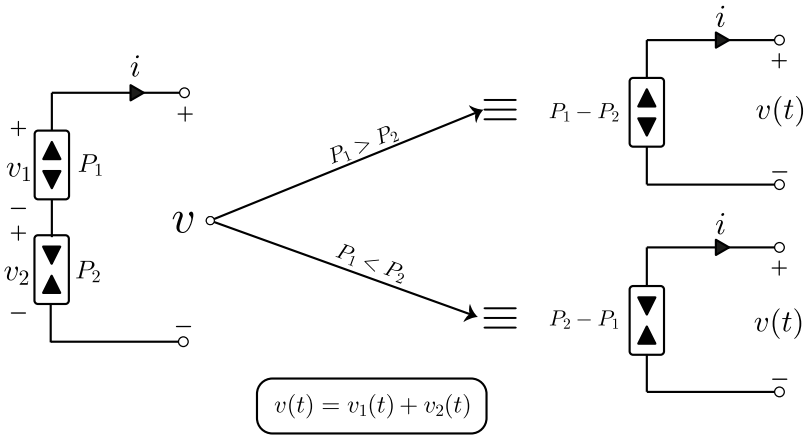

Fig. 1.18: Series connection of a power source and power sink.

Series connection of power source has been used to model the output series connection of n transformer-less SEPIC converter, each of them supplied by an individual solar panel with its own MPPT. The resulting system allows maximum power extraction from each PV source even in cases of non-uniform irradiance [18]. Fig. 1.19a shows the interconnection supplying a regulated dc bus while Fig. 1.19b illustrates the steady-state model of the output series connection.

1.2.2 Parallel connection

Connecting in parallel n power elements results in an equivalent power source, which supplies the algebraic sum of the corresponding n currents and the algebraic addition of the power of each source while supporting the same original voltage as depicted in Fig 1.20.

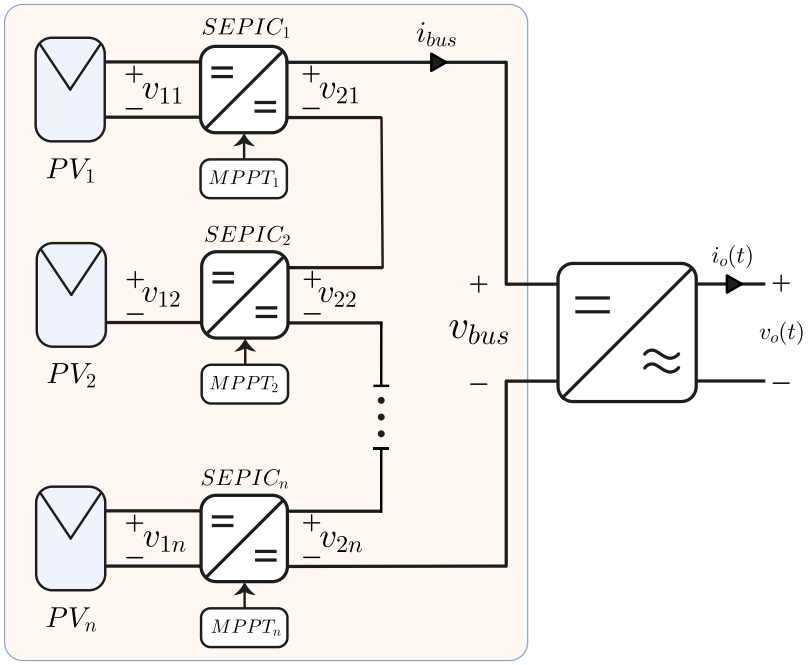

(a)

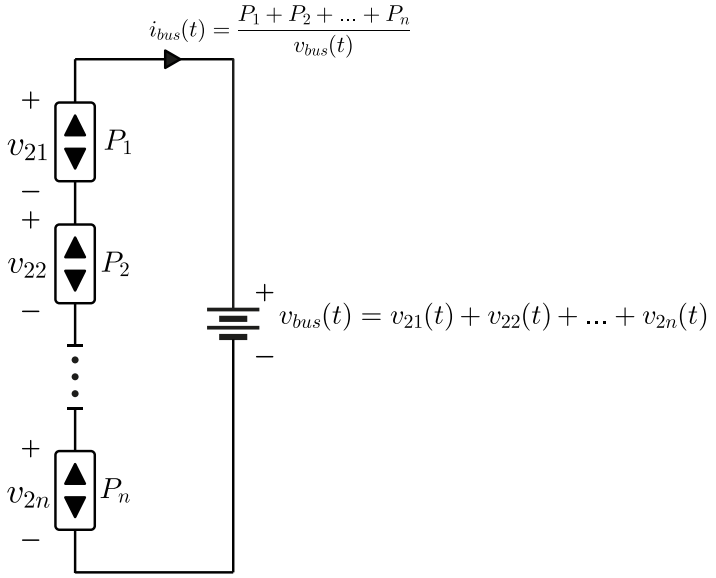

(b)

Fig. 1.19: (a) Output series connection of SEPIC converter with individual PV panel and MPPT and (b) steady-state output port model.

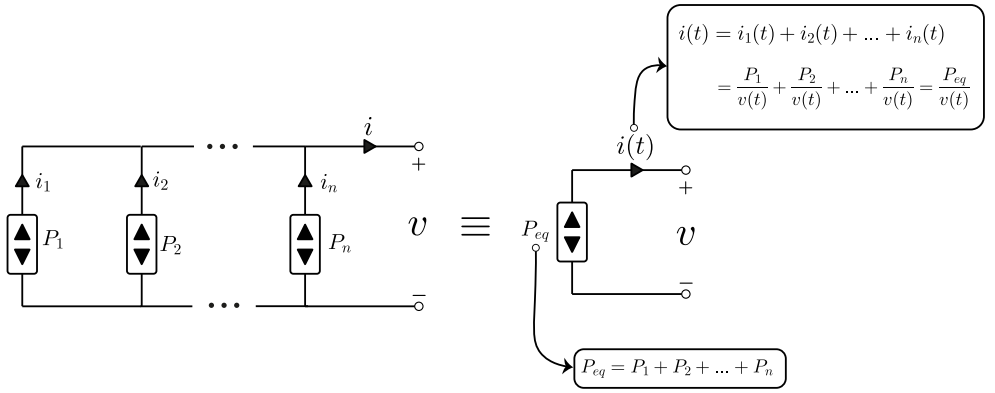

Fig. 1.20: Parallel connection of power sources.

The parallel connection can exhibit equally sinks or source or a combination of them as shown in Fig. 1.21 for the case of two elements.

Paralleling of power sources has been reported in the modular implementation of a dc nanogrid that uses the notion of LFR as the main building block [19]. The nanogrid uses n PV generators and the ac grid to supply a domestic dc bus of $380V$, which feeds dc loads of different type. A storage battery sup-

ports the nanogrid ensuring uninterruptible power supply and controls the dc bus through a bidirectional LFR as illustrated in Fig. 1.22.

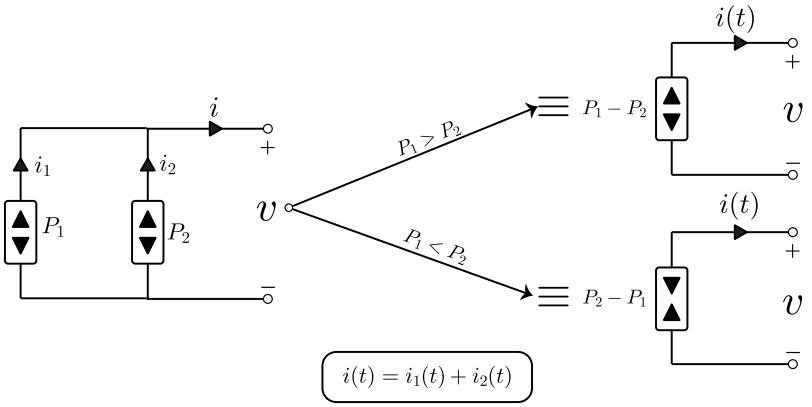

Fig. 1.21: Parallel connection of a power source and power sink.

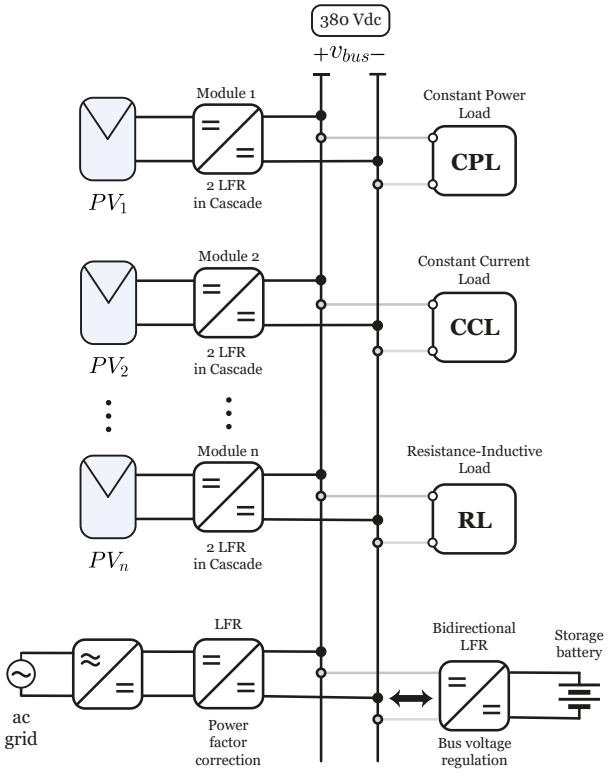

Fig. 1.22: LFR-based dc nanogrid.

1.3 Motivation

It has been shown that power elements model the transference of power in PV systems, microgrids or electric vehicles. They appear in the form of one-port circuits, i.e., a single CPL or a power source, or in the form of two port devices like the LFR or the PET.

In both cases, the literature review has demonstrated that sliding mode control (SMC) [20] is an essential element in the regulation of the power transference due to its versatility, robustness, and systematic design.

A recent report of SMC regulating the output voltage of a boost converter supplying a CPL has been published in [21], where the unstable ON and OFF open-loop trajectories are appropriately combined to yield a stable trajectory using a switching function based on a linear combination of inductor current error and capacitor voltage error.

With the latter work as main antecedent, it makes sense to explore other alternatives exploiting the same principle, i.e., disclosing sliding surfaces with an appropriate switching policy that yields a stable trajectory leading to the desired equilibrium point (EP) from zero initial conditions and keeps the coordinate of the output voltage constant in spite of input voltage or output power disturbances.

In addition, it could be interesting that SMC copes with the problem of uncertainty in the power of the CPL by providing mechanisms of power estimation. Moreover, the SMC in this context should be flexible, so a simple particularization of the switching function for the voltage regulation in the CPL supply should result in the switching function for either LFR or PET implementation.

It has to be pointed out that all LFRs or PETs reported in the literature terminate at a resistor, and it has not been proved that they can exhibit the same performance if the resistor is substituted by other types of loads. Resistive load has been the classical approach to model the one-port device supplied by a centralized converter in telecom or computer equipment, but the increased use of multi-converter systems in EVs and microgrids has introduced the notion of constant current load (CCL) plus the concept of CPL introduced at the beginning of this chapter. Besides, the existing interest for fast charging of EVs [22] has brought up lithium-ion batteries as candidate for new type of loads in power converter systems [23].

Charging techniques consist in a first phase of either constant current (CC), constant power (CP) or other profiles, followed by a phase of constant voltage (CV) [24]. Hence, the first phase of the battery charging system can be modelled in some cases by a constant current source or by a constant power source in other. In both situations, the active source feeds a battery that can be effectively modelled as a voltage source in series with a resistor.

Therefore, the study of a SMC-based LFR loaded by the parallel connection of a CPL, a CCL and a battery with internal resistance could give a valuable insight in the transferences of power to these new types of load.

Power regulation based on the LFR concept, or the PET notion could be studied in the first phase of a CP-CV protocol for battery charging. Adding an outer loop for voltage regulation to ensure the CV phase would be the first step for the power-mode control of dc-dc switching converters, a name taken for similarity with the current-mode control.

1.4 Objectives

The main goal of this research is to propose SMC strategies that can improve the performance of the existing ones in the voltage regulation of power converter supplying CPLs. In addition, the SMC should cope with the uncertain value of the CPL power and should be flexible enough to be adapted for LFR operation with different types of loads. The thesis is organized as follows:

Chapter 2 proposes polynomial surfaces of inductor current and capacitor voltage to regulate the output voltage of a boost converter with CPL.

In chapter 3, an estimation loop of CPL power is inserted in a SMC based on one of the polynomials surfaces analyzed in chapter 2.

Chapter 4 presents the SMC of a boost converter operating as a LFR, which supplies a constant power to the parallel connection of three canonical elements, namely, CPL, CCL, and a dc source with internal resistance. The studied load is defined as generic nonlinear static load (GNSL).

Chapter 5 studies the implementation of a CP-CV battery charging protocol and compares its performance with that of the standard CC-CV on equal basis in electronics terms.

Finally, the conclusions of the thesis are summarized in chapter 6.

Part I

Power sink elements

UNIVERSITAT ROVIRA I VIRGILI
A SLIDING MODE APPROACH TO CONTROL POWER SINKS AND POWER SOURCES IN DC-DC SWITCHING CONVERTERS
David Alejandro Zambrano Prada

Chapter 2

Sliding surfaces to control a boost converter with constant power load

Introduction

The introductory chapter has presented the concept of power elements, categorizing them according to the model of a one-port circuit or a two-port device, or by describing them by the effects they generate in the electronic systems either as constant power sink (CPL) or constant power source.

In the classical model approach of power converters, the load is resistive, so the power demand is variable and depends on the operating point. In addition, the load introduces the necessary damping in the dc-dc converters making them stable in the open loop, so classical regulation techniques can be applied to design closed control loops.

When considering power elements as dc loads, power converters supplying a CPL are unstable in open-loop and continuous conduction mode (CCM) because their state-vector trajectories are open and unbounded in both ON and OFF states and their combination does not result in a stable trajectory irrespective of the duty cycle value [25]. Nonetheless, they are stable in open loop and discontinuous conduction mode (DCM) within a limited operation region [26] and can operate in CCM in closed-loop with an appropriate feedback strategy.

In the linear approach, the power converter models are based on a linear

averaged model of the converter, in which the CPL has been substituted by a negative resistor representing its linearized model around the steady-state operating point as shown in Fig. 2.1.

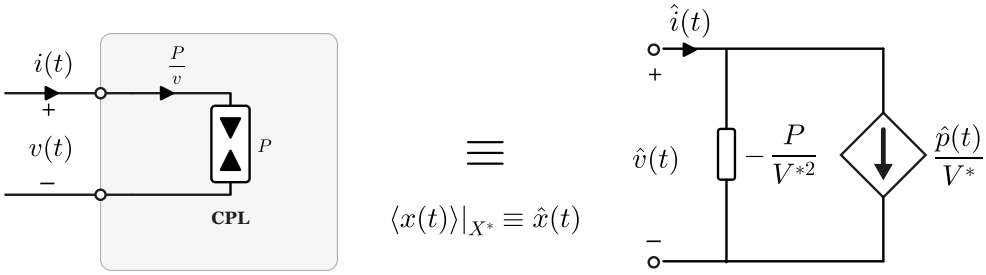

Fig. 2.1: Small-signal model of a CPL from linearization of the large-signal model around steady-state X^*.

As a consequence, the resulting transfer functions relating the control to output voltage or the control to inductor current are unstable. It is worth noting that the steady-state values of the state variables required in the converter transfer functions are the ones desired for its closed-loop operation provided that an appropriate controller stabilizes it.

Thus, the necessary damping to stabilize the unstable effect of the negative resistance can be introduced by means of current control [27], i.e., by cascade control using inductor current feedback in an inner loop whose reference is given by an outer loop processing the output voltage error [28]. However, the transfer function relating the output voltage to the control signal can be unstable for certain values of the converter parameters, so the design of the outer loop must cope with the stabilization of an unstable plant, resulting from the insertion of the current loop constraint in the power stage dynamics, and the specifications for output voltage regulation [29].

Nonlinear approaches to control power converters with CPL use feedback linearization [30]–[32] boundary control [33], [34] or SMC [35]–[40].

Feedback linearization controllers are based on pulse-width modulation (PWM) and designed either to directly compensate the nonlinearity introduced by the CPL [30], [31] or to indirectly create a virtual mesh to both stabilize the system and regulate the output voltage [32].

Boundary control [33], [34] uses the converter state variables to establish a

linear boundary with negative slope where switching takes place. ON and OFF states correspond to trajectories below and above the boundary respectively, which ensures that trajectories on one side of the boundary are directed to the other side eventually resulting in a good degree of output voltage regulation.

SMC constitutes a reliable and efficient solution for many open problems in the control of power converters by offering robustness in the face of parametric uncertainty and a systematic approach in the controller design [41].

It has been used to regulate the output voltage of a boost converter supplying a CPL in parallel with a resistive load by means of a sliding surface based on a linear combination of the capacitor voltage error and the difference between the inductor current and its high frequency component [35]. In that work simulations have shown the existence of bifurcations for certain values of the gain of the current error. SMC has also been used as starting point for a PWM nonlinear control implementation in [36], in which a nonlinear switching function made up of the product of inductor current and capacitor voltage in a boost converter was proposed to regulate the output voltage. That function was modified in [37] by adding a linear term proportional to the output voltage error to improve the voltage regulation, and by substituting the PWM device by an ideal comparator, which resulted in a highly variable switching frequency.

Besides, a high-order SMC based on a super-twisting algorithm has been proven by simulation to be effective in the output voltage regulation of a buck converter with a CPL [39] while sliding surfaces based either on the current error or on a linear combination of current and voltage error have been successfully used to regulate a 380 V dc bus voltage of an islanded DC microgrid with multiple photovoltaic generators, several boost converters and a battery bank [38].

A digital cascade sliding mode–based control with PWM was proposed in [40] reporting a high degree of output voltage regulation and the suppression of the inrush current in a boost converter prototype with a CPL of 1 kW. In most of the cited examples, the use of the boost converter is of particular interest as a case study for its non-linear non-minimum phase behavior in a clear-cut contrast with the linear dynamic features of the buck converter.

The work reported in [21] has been presented in the introduction as the main antecedent of this research. It introduced a linear switching function that can be classified as a one-degree polynomial surface and outperformed previous control

reports on the subject. Considering that feature, it makes sense to explore polynomial surfaces with a more general perspective and systematic approach in an attempt to analyze the potential benefits in terms of stability, disturbance rejection, conduction losses and inrush current.

As a starting point, this chapter presents an analysis of trajectories of the boost converter with CPL under SMC and the associated procedure to choose suitable surfaces. With this aim, it covers exhaustingly the analysis of polynomial surfaces until two-degree by providing their sliding mode existence conditions and resulting characteristics. Simulation and experimental results will validate the analysis.

Finally, some ideas are presented for the extension of the proposed method to other types of loads, i.e., CCL or RL, and other types of surfaces.

2.1 Overview of the sliding surface definition

2.1.1 Natural trajectories of a boost converter with constant power load

Fig. 2.2 shows the circuit diagram of a unidirectional boost converter supplying a CPL. The converter supplies to the load a current $i_{CPL} \leq 0$, which is defined by the nonlinear relation P/v_C, P being the non-negative power absorbed by the load and $v_{CPL} = v_C$ the output voltage.

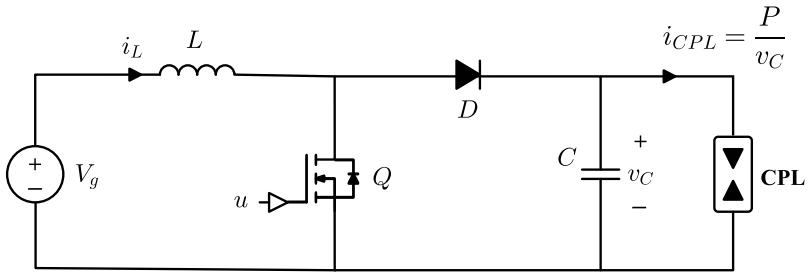

Fig. 2.2: Boost converter with CPL.

The converter state equations can be expressed as follows

$$L\,\frac{di_L}{dt} = V_g - (1-u)\;\; v_C \tag{2.1a}$$

$$C\frac{dv_C}{dt} = i_L\,(1-u) - \frac{P}{v_C} \tag{2.1b}$$

where $i_L \geq 0$ is the inductor current, V_g is the input voltage and u is a driving signal that changes the converter structure, so that $u = 1$ for ON state and $u = 0$ for OFF state.

It was analytically demonstrated in [21] that the trajectory during on state is of parabolic type while it was predicted without a proof in the same work that the trajectory corresponding to off state would result in a growing spiral. A complete analysis of the trajectories is carried out in the following paragraphs in order to understand the dynamic behavior of the boost converter with CPL in open-loop. With this aim, numerical simulations are used, with the set values shown in Table 2.1.

Table 2.1: Parameter values for numerical simulation of boost with CPL.

Parameter	**Values**
L	500 μH
C	20 μF
P_{CPL}	1 kW
V_g	200 V

Fig. 2.3 illustrates the simulation result of the trajectory of state vector $x = [i_L, v_C]^\intercal$ during ON-state in the phase-plane $i_L - v_C$.

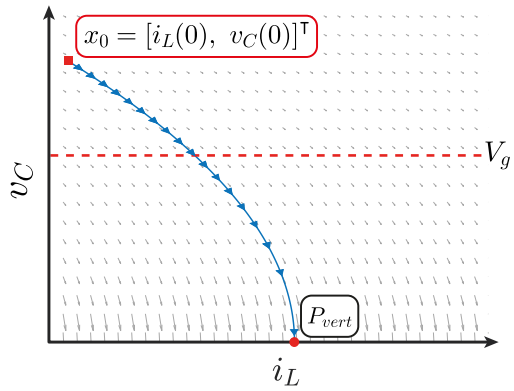

Fig. 2.3: State-plane trajectory for ON state of a boost converter with CPL.

For this case, an analytical expression of the trajectory was reported in [21] and given by

$$i_L(t) = i_L(0) - \frac{v_C^2(t) + v_C^2(0)}{\lambda} \tag{2.2a}$$

$$v_C^2(t) + \lambda\, i_L(t) - \left(v_C^2(0) + \lambda i_L(0)\right) = 0 \tag{2.2b}$$

where

$$\lambda = \frac{2PL}{CV_g} > 0 \tag{2.3}$$

In the figure, $i_L(0)$ and $v_C(0)$ are the initial values of inductor current and capacitor voltage, respectively. Equations (2.2) corresponds to a parabolic curve with vertex in $P_{vert} = \left[i_L(0) + v_C^2(0)/\lambda, 0\right]^\intercal$ and negative slope $-\lambda/2v_C$ exhibiting a decreasing behavior in voltage and increasing behavior in current irrespective of the initial condition until the trajectory reaches P_{vert} as shown in Fig. 2.3, which means a short circuit in the input power source.

On the other hand, the OFF-state trajectory can be described by the following equations:

$$i_L(t) = \frac{V_g}{L}t + i_L(0) - \frac{1}{L}\int_0^t v_C(\tau)\, d \tag{2.4a}$$

$$C\frac{d^2 v_C}{dt^2} - \frac{P}{v_C^2}\frac{dv_C}{dt} + \frac{v_C}{L} = \frac{V_g}{L} \tag{2.4b}$$

Although it is not possible to find an analytical solution for (2.4), an equilibrium point (EP) in $x_{eq} = [P/V_g, V_g\}^\intercal$ can be predicted. Besides, the first equation in (2.4) suggests the existence of a harmonic solution with an unbounded behavior since the term $-P/v_C^2$ on the first time-derivative of v_C is always negative. Fig. 2.4 illustrates a numerical solution of (2.4) showing a growing spiral with focus in x_{eq}, which turns out to be an unstable EP. The spiral grows until it collapses at $v_C = 0$.

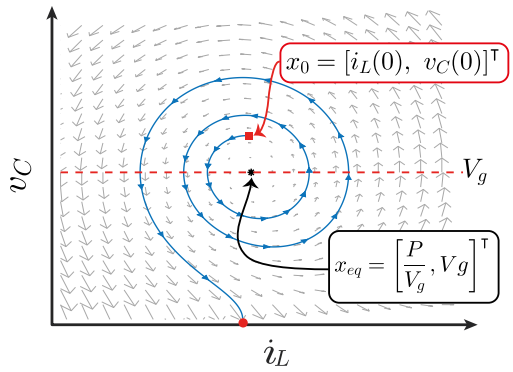

Fig. 2.4: State-plane trajectory for OFF state of a boost converter with CPL.

2.1.2 Equilibrium point locus and forced trajectories

The analysis of the natural trajectories of ON and OFF states has revealed that both are unstable. However, an appropriate transition between states under a correct choice of a control law would allow a stable trajectory leading the converter to a desired EP. That point must be contained within the equilibrium point locus EPL if the latter exists. This can be obtained assuming that the derivatives of the trajectories in the state-plane for ON and OFF states are opposite with equal absolute value [42]. Therefore

$$\left|\frac{dv_C}{di_L}\right|_{\text{ON}} = \left|\frac{dv_C}{di_L}\right|_{\text{OFF}} \tag{2.5}$$

Fig. 2.5 shows graphically the EPL in the phase-plane overlapping the vector field of both states of the converter. From Equation (2.5) and Fig. 2.2, we deduce that the EPL will be given by $I_L = P/V_g$ and $v_C \geq V_g$. Note that this EPL equation reflects the POPI nature of the converter in steady-state regime, i.e., the dc output power P equals the dc input power $I_L V_g$ [9].

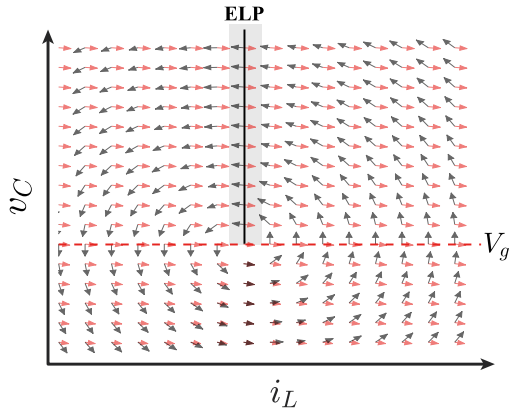

Fig. 2.5: Equilibrium point locus after overlapping ON and OFF vector field.

Within the sliding mode frame, it is apparent that an EP can result from the intersection of a sliding surface $\Sigma = \{x|\ S(x) = 0\}$ and the EPL provided that an appropriate switching policy can be imposed to the converter. The switching policy has to combine the ON and OFF unstable trajectories to create a stable trajectory that slides on average along Σ to attain the desired EP. This idea is illustrated in Fig. 2.6 for an arbitrary sliding surface, the switching policy consisting in turning ON the converter when the state vector trajectory is below the sliding surface and turning OFF the converter when it is above the surface.

The ideal sliding behavior in Fig. 2.6 requires an infinite switching frequency, so in order to relax this constraint, a hysteresis band is introduced around the sliding surface as illustrated in Fig. 2.7.

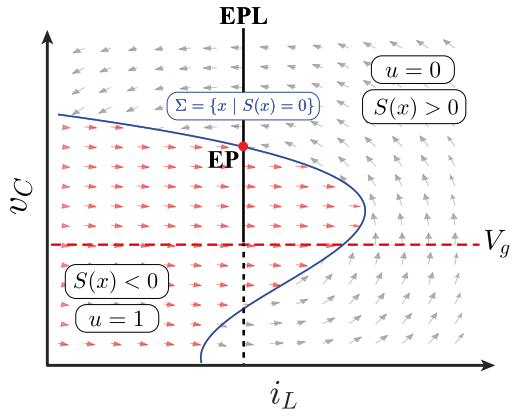

Fig. 2.6: Combining unstable trajectories results in a stable trajectory leading to the EP.

By adding this hysteresis band, the control law outside the hysteresis band can be expressed as follows

$$u = \begin{cases} 0, & \text{if, } S(x) > +\delta \\ 1, & \text{if, } S(x) < -\delta \end{cases} \tag{2.6}$$

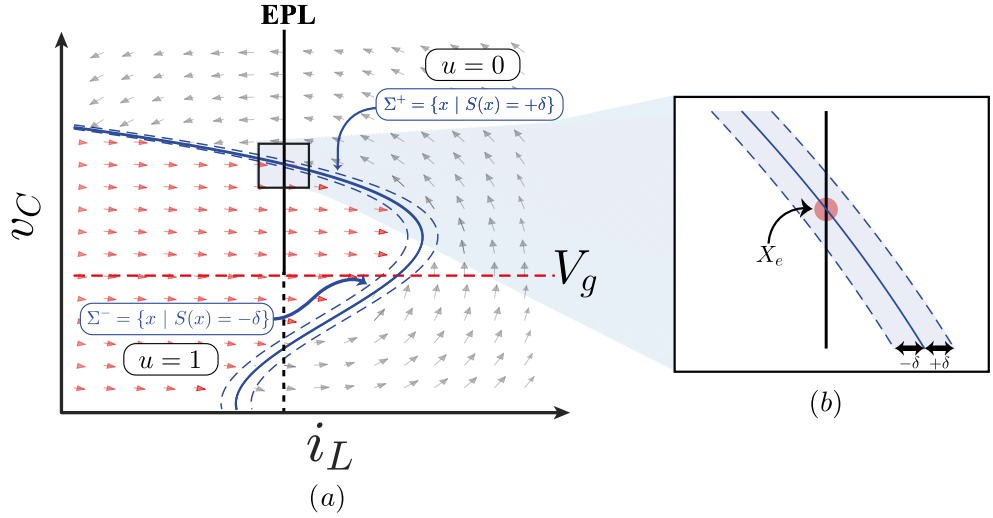

Fig. 2.7: Modified sliding surface by a hysteresis band adding a) state-plane vector field and switching policy b) zoom around EP.

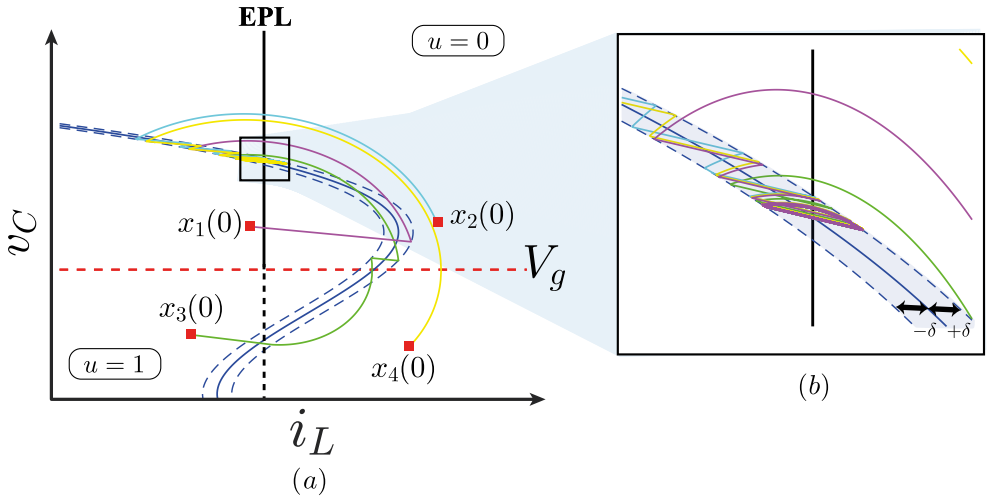

Fig. 2.8: (a) Forced trajectories reaching the EP for four different initial conditions. (b) Zoom in the vicinity of the EP.

Inside the hysteresis band u maintains its previous value when the last switching has taken place. Fig. 2.8 shows the resulting trajectories for four different initial conditions reaching the EP in finite time.

2.1.3 Operating region

The closed-loop trajectories presented in the examples in Fig. 2.8 reveal the advantage of constraining the converter start-up within the operating region $v_C = V_g$; it is high likely that initial points below V_g will imply a high peak current surge. In the case of a start-up with null initial conditions $x_{null} = [0,\ 0]^T$, the converter will handle a large input current.

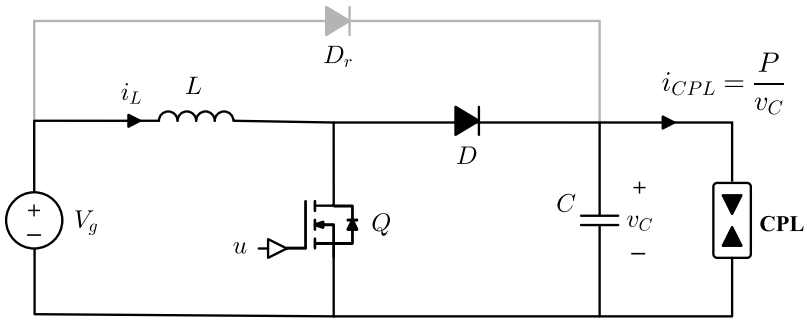

Fig. 2.9: Boost converter with complementary diode.

Adding a complementary diode between ports of the converter as shown in Fig. 2.9, the starting point will be actually $x_0 = [0, V_g]^\intercal$, which eventually guarantees sliding mode motion for the first instant when trajectories intersect the switching boundaries.

2.2 Polynomial sliding surfaces and conditions for existence and stability of sliding motions

As can be inferred from Fig. 2.6-2.7 the first requirement for the switching surface is to contain the EP $[I_e = P/V_g, V_e]^\intercal$ in its analytical expression and, at the same time, divide the state-plane in two regions so that an appropriate switching policy can eventually drive the forced trajectory to that point irrespective of the initial conditions. A first attempt to substitute the generic sliding surface $\Sigma = \{x|S(x) = 0\}$ of the previous figures by a concrete mathematical description consists in considering a surface of polynomial type according to the following general expression

$$S(x) = \sum_{i=1}^{n} \left(\frac{n}{i}\ a_i\ i_L^i \right) + \sum_{j=1}^{n} \left(\frac{n}{j}\ b_j\ {v_C}^j \right) + \sum_{i=1}^{n-1} \sum_{j=1}^{n-1} \left(\frac{n}{ij}\ h_{ij} i_L^i v_C^j \right) + e \quad (2.7)$$

Where n is the degree of the polynomial. The first and the second terms correspond to only i_L and v_C components. The third term is the multiplication between the state variables, and finally $e = f(I_e, V_e)$ determinates the desired EP. The coefficients a_i, b_j and h_{ij} will be selected according to the sliding motion conditions as shown in the paragraphs that follow.

Surfaces described by polynomials of degree zero, one and two are next analyzed in depth checking their capability to generate stable sliding motions.

2.2.1 Surfaces of degree zero

The surfaces of degree zero are defined here as those where only one of the sate variables is present. Thus, two sliding surfaces Σ_{0a} and Σ_{0b} of degree zero are possible:

$$\Sigma_{0a} = \{x | S_{0a}(x) = 0\} \tag{2.8a}$$

$$S_{0a}(x) = i_L - I_e = i_L - \frac{P}{V_g} \tag{2.8b}$$

$$\Sigma_{0b} = \{x |\ S_{0b}\ (x) = 0\} \tag{2.9a}$$

$$S_{0b}(x) = v_C - V_e \tag{2.9b}$$

The first case represents a current mode control and results in stable sliding mode behavior while the second one corresponds to a voltage mode control leading to unstable sliding mode motions when considering in both cases a resistive load [43]. In the CPL case here analyzed, $S_{0b}(x)$ still results in unstable behavior while the ideal sliding dynamics yielded by $S_{0a}(x)$ will evolve through the EPL line but the resulting voltage coordinate of the EP can take infinite possible values since the expression of $S_{0a}(x)$ coincides with that of the EPL. This is in a clear-cut contrast with the case of a resistive load in which there is only one EP that is always stable.

2.2.2 Surfaces of degree one

The general expression of a sliding surface Σ_1 of degree one is described by particularizing the expression (2.7) with $n = 1$, resulting in the following affine function

$$\Sigma_1 = \{x |\ S_1\ (x) = 0\} \tag{2.10a}$$

$$S_1(x) = a_1 i_L + b_1 v_C + e \tag{2.10b}$$

In order to make the notation of $S_1(x)$ simpler, the subindices will be omitted from now onward in the coefficients. The value of e is derived from the coordinates of EP following the description in (2.8) and (2.9), and is given by

$$e = -\left(aI_e + bV_e\right) = -\left(\frac{aP}{V_g} + bV_e\right) \tag{2.11}$$

Sliding motions will exist if the condition $S_1(x)\,\dot{S}_1(x) < 0$ is satisfied [20]. From (2.1) and (2.10), the expression for $\dot{S}_1(x)$ is obtained

$$\dot{S}_1(x) = \left(\frac{aV_g}{L} - \frac{bP}{Cv_C}\right) - \left(\frac{av_C}{L} - \frac{bi_L}{C}\right)(1-u) \tag{2.12}$$

Imposing $S_1(x)\,\dot{S}_1(x) < 0$ and particularizing expression (2.12) for $u = 0$ and $u = 1$ leads respectively to expressions (2.13a) and (2.13b).

$$\lim_{S(x)\to 0^+} \dot{S}_1\ (x)\Big|_{u=0} = \left(\frac{aV_g}{L} - \frac{bP}{Cv_C}\right) + \left(\frac{bi_L}{C} - \frac{av_C}{L}\right) < 0 \tag{2.13a}$$

$$\lim_{S(x)\to 0^-} \dot{S}_1(x)\Big|_{u=1} = \left(\frac{aV_g}{L} - \frac{bP}{Cv_C}\right) > 0 \tag{2.13b}$$

Expressions can be compacted as follows

$$i_L < \frac{P}{v_C} + \frac{aC}{bL}\left(v_C - V_g\right) \tag{2.14}$$

Inequality (2.14) establishes the region for the existence of sliding motions (ESM), in which the combination of ON and OFF trajectories can be described on average by a sliding trajectory along the switching surface. The sliding motion along the switching surface implies the fulfilment of the invariance conditions $S_1(x) = 0$ and $\dot{S}_1(x) = 0$ [20], which results in the equivalent control $u_{1_{eq}}$ with $0 \le u_{1_{eq}} \le 1$, and corresponding ideal sliding dynamics given by

$$u_{1\ eq} = 1 - \frac{\frac{\mathrm{aV}_g}{L} - \frac{bP}{\mathrm{Cv}_C}}{\frac{\mathrm{av}_C}{L} - \frac{\mathrm{bi}_L}{C}} \tag{2.15a}$$

$$i_L = \frac{P}{V_g} - \frac{b\left(v_C - V_e\right)}{a} \tag{2.15b}$$

$$C\frac{dv_C}{dt} = \frac{-\frac{bV_g}{L}\left(v_C - V_e\right)}{\frac{av_C}{L} - \frac{b}{C}\left(\frac{P}{V_g} - \frac{b(v_C - V_e)}{a}\right)} \tag{2.15c}$$

It is worth to note that (2.15) is nonlinear and linearizing around its EP $v_C = V_e$ leads to the following small signal dynamics.

$$\frac{d\widetilde{v_C}}{dt} \approx \frac{-\frac{\mathrm{bV}_g}{L}}{C\left(\frac{\mathrm{aV}_e}{L} - \frac{bP}{\mathrm{CV}_g}\right)}\widetilde{v_C} = -\frac{B}{\Lambda}\widetilde{v_C} \tag{2.16}$$

where the superscript $(\sim)$ means small variations around the EP, and B a Λ are given by

$$B = \frac{\mathrm{bV}_g}{LC} \tag{2.17a}$$

$$\Lambda = \frac{aV_e}{L} - \frac{bP}{CV_g} \tag{2.17b}$$

Since $B > 0$ we deduce from (2.16) that the system will be stable if $\Lambda > 0$, which implies the existence of an upper limit P_{max} the power of the CPL. Therefore, for stability the follow condition must be satisfied.

$$P < \frac{a}{b}\frac{CV_gV_e}{L} \triangleq P_{max} \tag{2.18}$$

Besides, condition (2.18) requires that $\frac{a}{b} > 0$. A geometrical interpretation of this result can be associated with the slope of $S_1\left(x\right)$ in the phase plane. The

slope of the surface is defined as

$$\Delta_{S_1}\Big|_{X_e} \triangleq -\frac{\frac{\partial S_1(x)}{\partial i_L}}{\frac{\partial S_1(x)}{\partial v_c}}\Bigg|_{X_e} = -\frac{a}{b} < 0 \tag{2.19}$$

If the condition ab>0 is satisfied, the choice of an affine surface is limited to any straight line with negative slope in the phase plane $i_L - v_C$ and whose absolute value satisfies (2.18). Since the switching surface is a straight line, the slope is constant and stability is guaranteed at any point on the surface within the ESM region. From (2.19), it can be established the relation between the slope of the surface and $\frac{\partial v_c}{\partial i_L}$ of the converter in EP. The absolute value of $\Delta_{S_1}\Big|_{X_e}$ and $\frac{\partial v_c}{\partial i_L}\Big|_{X_e}$ are equal, and to be define by

$$R_1 \triangleq \frac{a}{b} \tag{2.20}$$

We can use as an estimate value of the inrush current the value of the current corresponding to the first intersection of the state trajectory and the switching surface [44], [45]. Since the converter starts up from $x_{(t_0)} = [0, V_g]^\intercal$ due to the action of the complementary diode D_r, the inrush current I_{inrush} can be estimated as

$$I_{inrush} = \frac{(V_e - V_g)}{R_1} + \frac{P}{V_g} \tag{2.21}$$

2.2.2.1 Special case: Linear surface

The expression (2.10) is an affine surface, where the coefficients a_1 and b_1 are independent of EP according to e in the expression (2.11). This is a systematic procedure in order to generalize the surface of degree one for any operating condition. Nevertheless, there exists a special case when e=0 resulting in a linear surface given by

$$\Sigma_{1b} = \{x | S(x) = 0\} \tag{2.22a}$$

$$S_{1b}(x) = a i_L + b v_C \tag{2.22b}$$

Here, in order to ensure the intersection of EP and the linear surface, the coefficients must take the following values

$$a = -V_e \tag{2.23a}$$

$$b = \frac{P}{V_g} \tag{2.23b}$$

Applying the same control law and method as in the previous section, the following results are obtained.

Surface time-derivative:

$$\dot{S}_{1b}(x) = \left(\frac{V_g V_e}{L} + \frac{P^2}{C V_g v_c}\right) - \left(\frac{P}{C V_g} i_L + \frac{V_e}{L} v_c\right)(1-u) \tag{2.24}$$

Invariance condition:

$$i_L = \frac{P v_C}{V_g V_e} \tag{2.25a}$$

$$u_{1b_{eq}} = 1 - \frac{\frac{V_e V_g}{L} + \frac{P^2}{C V_g v_C}}{\frac{V_e}{L} v_C + \frac{P^2 v_C}{C V_g^2 V_e}} \tag{2.25b}$$

Ideal sliding dynamics:

$$C\frac{dv_C}{dt} = \frac{\frac{P}{L}(v_C - V_e)}{v_C\left(\frac{V_e}{L} + \frac{P^2}{C V_g^2 V_e}\right)} \tag{2.26}$$

Linearizing around its EP:

$$\frac{d}{dt}\widetilde{v_C} = \frac{\frac{P}{L}}{C\left(\frac{V_e}{L} + \frac{P^2}{CV_g^2V_e}\right)}\widetilde{v_C} \tag{2.27}$$

From (2.27), it is easy to determine that the boost converter supplying a CPL controlled with a linear surface is unstable. This validates the conclusion obtained from the analysis for the affine surface, since

$$\Delta_{S_{1b}}\Big|_{X_e} = \frac{V_eV_g}{P} > 0 \tag{2.28}$$

2.2.3 Surface of degree two

Particularizing (2.7) for $n = 2$, equation (2.29) is obtained. This is the general expression of a conic curve illustrating the sliding surface of second degree considered below in the analysis.

$$\Sigma_2 = \{x|\ S_2\ (x) = 0\} \tag{2.29a}$$

$$S_2\,(x) = a_2i_L^2 + b_2v_C^2 + 2h_{11}i_Lv_C + 2a_1i_L + 2b_1v_C - e \tag{2.29b}$$

To simplify the notation, h_{11} is written as h. The intersection of the surface and EP implies

$$e = a_2\frac{P^2}{V_g^2} + b_2V_e^2 + 2h\frac{PV_e}{V_g} + 2a_1\frac{P}{V_g} + 2b_1V_e \tag{2.30}$$

In this case, the ESM region can be expressed as

$$\alpha \left(i_L\right)^2 - \beta i_L - \gamma < 0 \tag{2.31}$$

where parameters α, β and γ are given by

$$\alpha = \frac{h}{C} \tag{2.32a}$$

$$\beta = \left(\frac{a_2}{L} - \frac{b_2}{C}\right) v_C - \frac{b_1}{C} - \frac{a_2 V_g}{L} - \frac{hP}{C v_C} \tag{2.32b}$$

$$\gamma = \frac{h V_g v_C + a_1}{L} \left(v_C - V_g\right) + \frac{b_2 P}{C} + \frac{b_1 P}{C v_C} \tag{2.32c}$$

In that region, the ideal sliding dynamics can be expressed by

$$u_{2_{eq}} = 1 - \frac{\frac{V_g}{L}\left(a_2 i_L + h v_C + a_1\right) - \frac{P}{C v_C}\left(b_2 v_C + h i_L + b_1\right)}{v_C i_L \left(\frac{a_2}{L} - \frac{b_2}{C}\right) + h\left(\frac{v_C^2}{C} - \frac{i_L^2}{L}\right) + \left(\frac{a_1 v_C}{L} - \frac{b_1 i_L}{C}\right)} \tag{2.33a}$$

$$i_L = -\frac{h v_C + a_1}{a_2} \pm \sqrt{\left(\frac{h v_C + a_1}{a_2} + \frac{P}{V_g}\right)^2 + \frac{2Ph(V_e - v_C)}{a_2 V_g} - \frac{\left(b_2 + 2b_1\right)\left(v_C^2 - V_e^2\right)}{a_2}} \tag{2.33b}$$

$$\frac{dv_C}{dt} = \frac{1}{LC} \frac{\left(a_2 i_L + h v_C + a_1\right)\left(V_g i_L - P\right)}{\left(\frac{a_2}{L} - \frac{b_2}{C}\right) i_L v_C + h\left(\frac{v_C^2}{L} - \frac{i_L^2}{C}\right) + \left(\frac{a_1 v_C}{L} - \frac{b_1 i_L}{C}\right)} = \frac{N\left(i_L, v_C\right)}{D\left(i_L, v_C\right)} \triangleq g\left(x\right) \tag{2.33c}$$

Note, on the one hand, that (2.33) is a 1-dimensional system, since i_L is related to v_C through the sliding surface expression (2.29). Observe, on the other hand, that the EP of that expression is given by $i_L = P/V_g$, which, after substitution in (2.29), leads to the equation

$$\left(v_C - V_e\right)\left[b_2\left(v_C + V_e\right) + \frac{2hP}{V_g} + 2b_1\right] = 0 \tag{2.34}$$

Equation (2.34) has two solutions. The first one is $v_C = V_e$ and the second one is $v_C = -V_e - (2hP + 2b_1V_g)/(b_2V_g)$. With the assumption that b_1, b_2 and h are all positive, the second solution has no physical meaning.

Linearization of (2.33) around the EP requires the calculation of $\partial g(x)/\partial v_C$ at the EP. Differentiating $g(x)$ with respect to v_C, one gets

$$\frac{\partial g(x)}{\partial v_C} = \frac{\left(\frac{\partial N(i_L,v_C)}{\partial v_C} + \frac{\partial N(i_L,v_C)}{\partial iL}\frac{\partial i_L}{\partial v_C}\right) D(i_L,v_C) - \left(\frac{\partial D(i_L,v_C)}{\partial v_C} + \frac{\partial D(i_L,v_C)}{\partial iL}\frac{\partial i_L}{\partial v_C}\right) N(i_L,v_C)}{D^2(i_L,v_C)} \tag{2.35}$$

Since at the EP $P = V_g i_L$, $N(i_L, v_C) = 0$ and consequently (2.35) becomes

$$\left.\frac{\partial g(x)}{\partial v_C}\right|_{X_e} = \left.\frac{\left(\frac{\partial N(i_L,v_C)}{\partial v_C} + \frac{\partial N(i_L,v_C)}{\partial iL}\frac{\partial i_L}{\partial v_C}\right)}{D(i_L,v_C)}\right|_{X_e} \tag{2.36}$$

Developing the numerator of (2.36) yields

$$\left.\frac{\partial g(x)}{\partial v_C}\right|_{X_e} = \frac{(a_2P + hV_gV_e + a_1)\left(\left.\frac{\partial i_L}{\partial v_C}\right|_{X_e}\right)}{\frac{V_g}{L}\left(a_2\frac{P}{V_g} + hV_e + a_1\right) - \frac{P}{CV_g}\left(b_2V_e + h\frac{P}{V_g} + b_1\right)} \tag{2.37}$$

In order to obtain the term $\left.\partial i_L/\partial v_C\right|_{X_e}$, observe that the ideal sliding dynamics in the inductor current is given by

$$LC\frac{di_L}{dt} = -\frac{(b_2v_C + hi_L + b_1)(V_gi_L - P)}{\left(\frac{a_2}{L} - \frac{b_2}{C}\right)i_Lv_C + h\left(\frac{v_C^2}{L} - \frac{i_L^2}{C}\right) + \left(\frac{a_1v_C}{L} - \frac{b_1i_L}{C}\right)} \tag{2.38}$$

Dividing (2.38) by v_C in (2.33) and particularizing the result at EP results in

$$\left.\frac{\partial\, i_L}{\partial\, v_C}\right|_{X_e} = -\frac{b_2V_e + \frac{hP}{V_g} + b_1}{\frac{a_2P}{V_g} + hV_e + a_1} \triangleq -\frac{1}{R_2} < 0 \tag{2.39}$$

Note that we have assumed in (2.39) that numerator and denominator are both positive

$$\left(b_2 V_e + \frac{hP}{V_g} + b_1\right)\left(\frac{a_2 P}{V_g} + hV_e + a_1\right) > 0 \tag{2.40}$$

Finally, the small signal dynamics around EP will be expressed as follows

$$\frac{d\tilde{v_C}}{dt} = -\frac{1}{R_2}\frac{\frac{V_g}{LC}\left(\frac{a_2 P}{V_g} + hV_e + a_1\right)}{\frac{V_e}{L}\left(\frac{a_2 P}{V_g} + hV_e + a_1\right) - \frac{P}{CV_g}\left(b_2 V_e + \frac{hP}{V_g} + b_1\right)}\tilde{v_C} \tag{2.41}$$

From (2.40) and (2.41), it can be deduced that the system will be stable if the following condition is satisfied.

$$0 < \frac{LP}{CV_g V_e} < \frac{\frac{a_2 P}{V_g} + hV_e + a_1}{b_2 V_e + \frac{hP}{V_g} + b_1} \tag{2.42}$$

Note that the conic sliding surface given by $S_2(x)$ becomes the sliding surface $S_1(x)$ of degree one when $a_2 = b_2 = h = 0$. Indeed, one has

$$S_2(x)\Big|_{a_2=b_2=h=0} = 2\left(a_1 i_L + b_1 v_C - a_1\frac{P}{V_g} - b_1 V_e\right) \tag{2.43}$$

By calculating the slope of the curve at the equilibrium point, we obtain

$$\Delta_{S_2}\Big|_{X_e} \triangleq -\frac{\frac{\partial\ S_2(x)}{\partial\ i_L}}{\frac{\partial\ S_2(x)}{\partial\ v_c}}\Bigg|_{X_e} = -\frac{\frac{a_2 P}{V_g} + hV_e + a_1}{b_2 V_e + \frac{hP}{V_g} + b_1} = -R_2 < 0 \tag{2.44}$$

From (2.40), it can be deduced than R_2 is always positive. Therefore, the system controlled in sliding mode through the surface given by a general conic curve will be stable if the slope of the curve at EP is negative and smaller than

the bound given in (2.42) in terms of the system parameters.

These results allow establishing the stability necessary condition, i.e. for any higher order geometric curve used as the sliding surface, the slope of the surface on the trajectory and at the desired equilibrium point must be negative to ensure the stability of the system.

The conditions (2.18) and (2.42) can be unified in a unique stability condition, where the maximum power limit is defined by

$$P < R\frac{CV_gV_e}{L} \triangleq P_{max} \tag{2.45}$$

where

$$R = \left| r\left(x\right)\Big|_{X_e} \right| \tag{2.46}$$

Here, R is the absolute value at EP of the incremental resistance $r\left(x\right)$ of the converter. When the boost converter with CPL is in sliding motion, its incremental resistance and the slope of the surface are equivalent.

$$r\left(x\right) \triangleq \frac{\partial\ v_c}{\partial\ i_L} = -\frac{\frac{\partial\ S(x)}{\partial\ i_L}}{\frac{\partial\ S(x)}{\partial\ v_c}} \tag{2.47}$$

Thus, from the general expression for surface of degree n presented in (2.7), the general incremental resistance is equal to

$$r\left(x\right) = -\frac{\sum_{i=1}^{n}\left(a_i\ i_L^{i-1}\right) + \sum_{i=1}^{n-1}\ \sum_{j=1}^{n-1}\ \left(\frac{1}{j}\ h_{ij}i_L^{i-1}v_C^{j}\right)}{\sum_{j=1}^{n}\ \left(b_j\ {v_C}^{j-1}\right) + \sum_{i=1}^{n-1}\ \sum_{j=1}^{n-1}\ \left(\frac{1}{i}\ h_{ij}i_L^{i}v_C^{j-1}\right)} \tag{2.48}$$

In the case of surfaces of degree two ($n = 2$), expression (2.39) is derived from (2.48) particularizing at EP.

$$r\left(x\right)\Big|_{n=2}\Big|_{X_e} = -\left.\frac{a_2 i_L + h v_C + a_1}{b_2 v_C + h i_L + b_1}\right|_{X_e} = -\frac{\frac{a_2 P}{V_g} + h V_e + a_1}{b_2 V_e + \frac{hP}{V_g} + b_1} = -R_2 \tag{2.49}$$

Similarly, for the case of surface of degree one, expression (2.50) is obtained

$$r\left(x\right)\Big|_{n=1}\Big|_{X_e} = -\frac{a_1}{b_1} = -R_1 \tag{2.50}$$

2.2.3.1 Types of conic curves

The general expression of a conic curve given by (2.29) can be represented as follows

$$\begin{aligned} S_3\left(x\right) = {} & a_2\left(i_L - \frac{P}{V_g}\right)\left(i_L + \frac{P}{V_g}\right) + 2a_1\left(i_L - \frac{P}{V_g}\right) \\ & + b_2\left(v_C - V_e\right)\left(v_C + V_e\right) + 2b_1\left(v_C - V_e\right) \\ & + 2h\left(i_L v_C - \frac{PV_e}{V_g}\right) \end{aligned} \tag{2.51}$$

which will reduce the number of arithmetic operations eventually required in its implementation. Note that $h^2 < ab$ implies that $S_3\left(x\right)$ corresponds to an ellipse while $h^2 = ab$ represents a parabola, and $h^2 > ab$ leads to a hyperbola.

Table 2.2 summarizes 4 particular cases of expression (2.51), which result from (i) $b_2 = a_1 = h = 0$ (current parabola), (ii) $a_2 = b_1 = h = 0$ (voltage parabola), (iii) $a_2 = b_2 = a_1 = a_2 = 0$; $h = 1/2$ (cross power hyperbola), and (iv) $h = a_1 = b_1 = 0$ (ellipse in Cartesian form centered at the origin of the plane $i_L - v_C$). The stability condition (2.45) and the estimated value of the inrush current I_{inrush} are shown in the four cases.

It is worth mentioning the case $a_2 = b_2 = a_1 = 0$ and $h = 1/2$, which results in the following sliding surface, similar to the one reported in [39].

$$S_{3e}\left(x\right) = i_L v_C - \frac{PV_e}{V_g} + 2b_1\left(v_C - V_e\right) \tag{2.52}$$

Table 2.2: Surfaces of Degree Two Based on Four Canonic Conic Curves

Type of conic curve	**Surface**	**R**	**Stability**	$\mathbf{I_{inrush}}$
Current parabola	$S_{3a}(x) = a\left(i_L^2 - \frac{P^2}{V_g^2}\right) + 2n\left(v_C - V_e\right)$	$\frac{a_2 P}{b_1 V_g}$	$V_e > \frac{b_1}{a_2}\frac{L}{C} \triangleq V_{e_{min}}$	$\sqrt{\frac{2b_1\left(V_e - V_g\right)}{a_2} + \left(\frac{P}{V_g}\right)^2}$
Voltage parabola	$S_{3b}(x) = b\left(v_C^2 - V_e^2\right) + 2m\left(i_L - \frac{P}{V_g}\right)$	$\frac{a_1}{b_2 V_e}$	$P < \frac{a_1}{b_2}\frac{C V_g}{L} \triangleq P_{max}$	$\frac{b_2\left(V_e^2 - V_g^2\right)}{2a_1} + \frac{P}{V_g}$
Cross-power hyperbola	$S_{3c}(x) = i_L v_C - \frac{P V_e}{V_g}$	$\frac{V_e V_g}{P}$	$P < V_e V_g \sqrt{\frac{C}{L}} \triangleq P_{max}$	$\frac{P V_e}{V_g^2}$
Ellipse	$S_{3d}(x) = a_2\left(i_L^2 - \frac{P^2}{V_g^2}\right) + b_2\left(v_C^2 - V_e^2\right)$	$\frac{a_2 P}{b_2 V_e V_g}$	$\frac{a_2}{b_2} > \frac{L}{C}$	$\sqrt{\frac{b_2\left(V_e^2 - V_g^2\right)}{a_2} + \left(\frac{P}{V_g}\right)^2}$

2.2.4 Analysis summary

Fig. 2.10 summarizes the analysis of the sliding surfaces of degrees zero, one and two by illustrating the main features associated to eight surfaces corresponding respectively to expressions (2.8)-(2.10), and (2.22) plus the four ones shown in Table 2 and expression (2.51). Ideal sliding behavior, i.e., infinite switching frequency has been assumed in the represented trajectories. Besides, only trajectories for surfaces of degree one and degree two are considered since trajectories of degree zero either result in an infinite number of EPs or are unstable. The set of parameter values used for converter and sliding surface coefficients are collected in Table 2.3 and Table 2.4, respectively.

Table 2.3: The used converter's parameter values.

Parameter	**Values**
L	500 μH
C	20 μF
P_{CPL}	1 kW
V_g	200 V
V_e	380 V

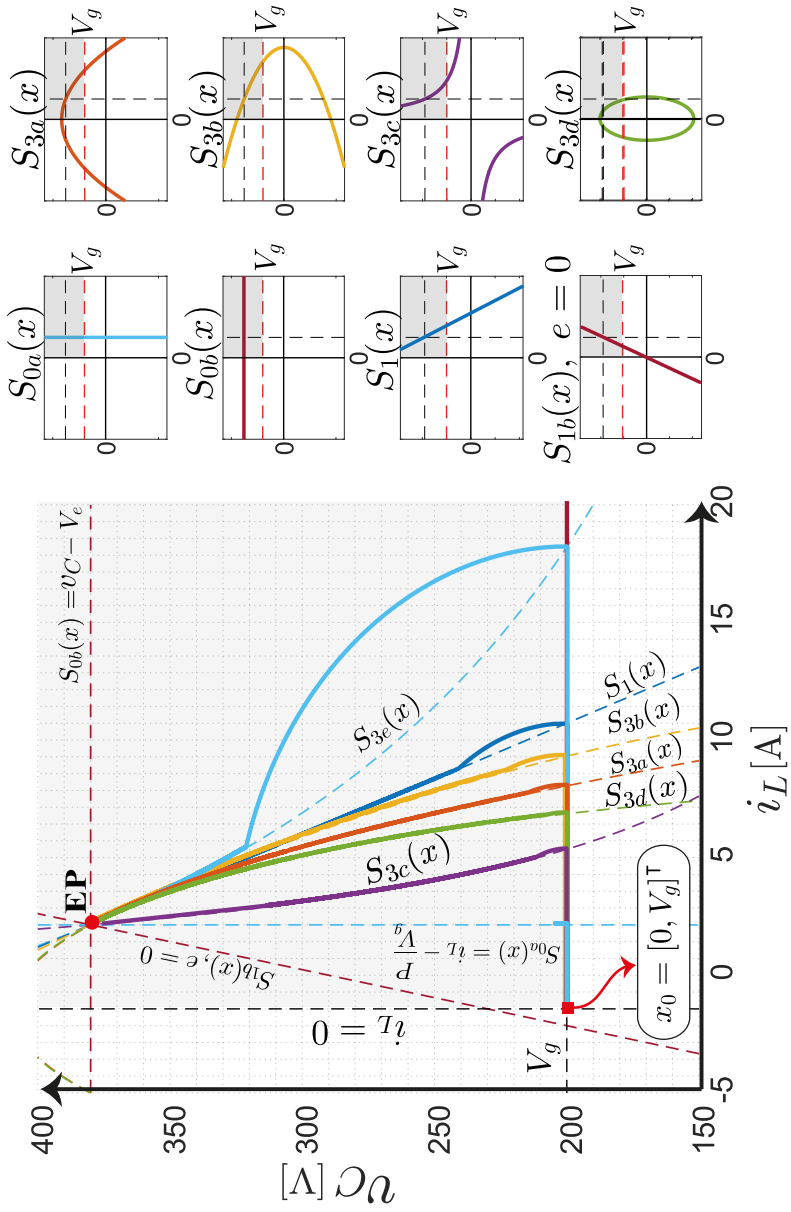

Fig. 2.10: Trajectory of the state vector from zero initial conditions to the EP for different sliding surfaces.

Table 2.4: Surface coefficients used in Fig. 2.10.

Surface	a_2	b_2	h	a_1	b_1	Stability status
$S_{0a}(x)$	0	0	0	P/V_g	0	Infinite number of EPs
$S_{0b}(x)$	0	0	0	0	V_e	Unstable
$S_1(x)$	0	0	0	4	0.26	Stable
$S_{1b}(x)$	0	0	0	$-V_e$	P/V_g	Unstable
$S_{3a}(x)$	1	0	0	0	0.42	Stable
$S_{3b}(x)$	0	0.001	0	5.2	0	Stable
$S_{3c}(x)$	0	0	1	0	0	Stable
$S_{3e}(x)$	1.9	0.002	0	0	0	Stable
$S_{3e}(x)$	0	0	1	0	1.25	Stable

2.3 Characteristics of polynomial sliding surfaces

2.3.1 Incremental resistance

In all the cases above studied, the dynamics of the system is of first order in sliding motion. Thus, expressions (2.16) and (2.41) can be described in a unified form as follows

$$\frac{d\tilde{v_C}}{dt} = -\frac{V_g}{Cv_C\left(r\left(x\right) - \frac{LP}{CV_gV_e}\right)}\bigg|_{X_e} \tilde{v_C} \tag{2.53}$$

Similar ideal sliding dynamics can be expected in all surfaces if we select the parameter values resulting in the same incremental resistance at EP. This fact can be observed in Fig. 2.10 for the five surfaces $S_1\left(x\right)$, $S_{3a}\left(x\right)$, $S_{3b}\left(x\right)$, $S_{3d}\left(x\right)$ and $S_{3e}\left(x\right)$ yielding stable trajectories, whose incremental resistance at EP is $r\left(x\right)\Big|_{X_e} = -15\ \Omega$. The exception is surface $S_{3c}\left(x\right)$, which in spite of yielding a stable trajectory, its incremental resistance $r\left(x\right)$ does not depend on the surface coefficients. In general, quadratic functions yield smaller values of

estimated inrush current than the affine function, the exception being surfaces $S_{3c}(x)$ and $S_{3e}(x)$ since they use the multiplicative term $i_L v_C$. Besides, note that $S_{3c}(x)$ coefficients are fixed, so that I_{inrush} only depends on the converter parameters.

Furthermore, Fig. 2.11a illustrates a complementary approach based on imposing the same value of the estimated inrush current I_{inrush} in all surfaces to facilitate the comparison, and to reduce the reaching time of the sliding surface. The value corresponding to surface $\Sigma_{3c}(x)$ has been chosen, i.e., a value of $I_{inrush} = PV_e/V_g^2 = 9.5$ A has been used in all cases. The exception is $\Sigma_{3e}(x)$, which results in a value of $I_{inrush} = 0.5$ A higher than the established reference as it can be deduced from (2.52) and the value of parameter b_1 in Table 2.5.

Table 2.5: Surface coefficients used in Fig. 2.10.

Surface	$\mathbf{a_2}$	$\mathbf{b_2}$	**h**	$\mathbf{a_1}$	$\mathbf{b_1}$
$S_1(x)$	0	0	0	4	0.1
$S_{3a}(x)$	1	0	0	0	0.1812
$S_{3b}(x)$	0	0.001	0	11.5	0
$S_{3c}(x)$	0	0	1	0	0
$S_{3e}(x)$	3.2	0.002	0	0	0
$S_{3e}(x)$	0	0	1	0	0.5

On the other hand, Fig. 2.11b shows the variation of $r(x)$ all along the trajectory from the inrush point ($i_L = I_{inrush}$, $v_C = V_g$) to the EP for the different surfaces considered in Fig. 2.11a. The horizontal axis corresponds to the number of points (i_L, v_C) considered in the calculation of $r(x)$ given by expression (2.48).

Other observation is that the initial value of $r(x)$ in the quadratic surfaces is higher than that in linear surfaces, ensuring a small value of the inrush current. The corresponding behavior of the output voltage in the time-domain is illustrated in a PSIM© simulation in Fig. 2.12, the fastest response being the one corresponding to the elliptical sliding surface $S_{ed}(x)$.

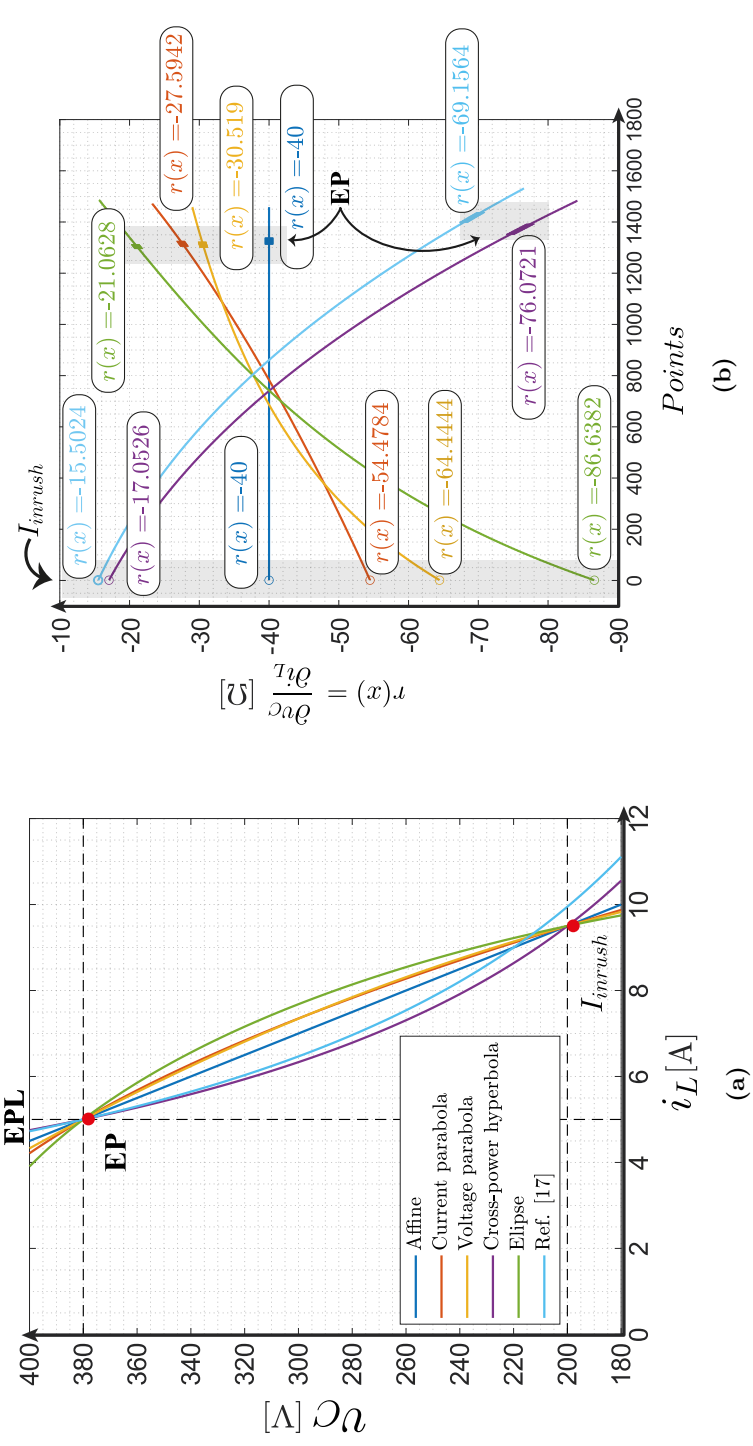

Fig. 2.11: (a) Sliding surfaces with the same value of the estimated inrush current. (b) Incremental resistance along the trajectory.

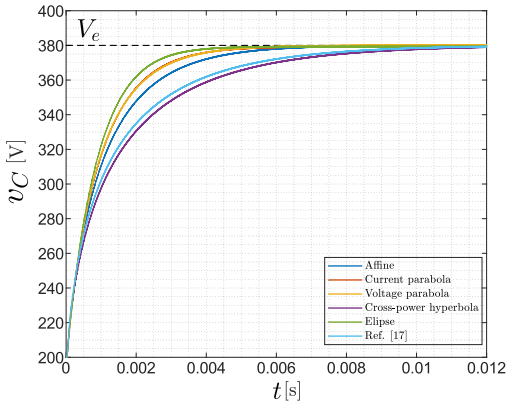

Fig. 2.12: Simulation of output voltage during start-up for different sliding surfaces.

2.3.2 Existence of sliding motion region

It can also be observed from Fig. 2.10 that a high value of inrush current will imply a large region in which the converter follows its natural dynamics before it reaches the surface and slides to the EP. It would therefore seem that a high inrush current value corresponds to a smaller ESM region. However, the inrush current is a consequence of the shape of the surfaces in the state-plane and the condition imposed by the complementary diode, and it is more appropriate to associate the ESM region to the type of surface rather than just to the surface intersection point. Taking the surface $S_1(x)$ for example, condition (2.14) of its EMS region can be rewritten in terms of its incremental resistance as follows

$$i_L < l\left(v_C\right) = \frac{P}{v_C} - \frac{C}{L} r\left(x\right)\left(v_C - V_g\right) \tag{2.54}$$

Where $l\left(v_C\right)$ is the limit function of EMS dividing the phase plane in two sides, and $r\left(x\right) = R$ along the affine surfaces when the converter is in sliding motion. Fig. 2.13 shows three trajectories from null initial conditions to EP for three different values of R and their respective EMS regions appropriately highlighted.

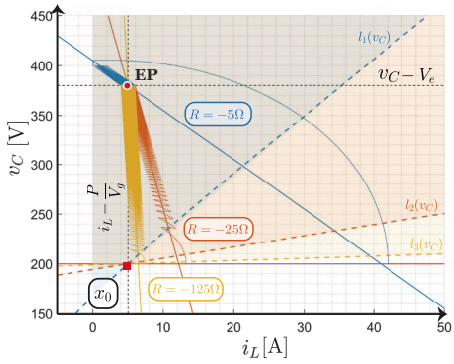

Fig. 2.13: ESM region of the surface $S_1(x)$ for three values of R.

The function $l\,(vc)$ approximates a linear relation with slope equal to R. Consequently, a lower value of R, means a smaller ESM region, and given that the surface is a straight line, such lower values of R will generate an intersection with $v_C = V_g$ further away from the null initial conditions together with a higher I_{Inrush}. If the converter takes longer to reach the surface and follows its natural trajectories, this will allow a faster reaching of the equilibrium point as shown in Fig. 2.14, at the cost of an increment in the initial current and power.

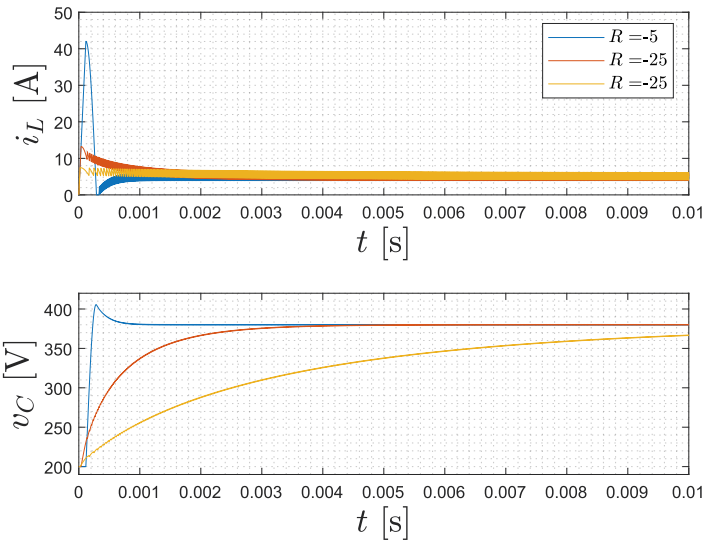

Fig. 2.14: Start-up of boost converter with CPL using the surface $S_1(x)$ for three values of R.

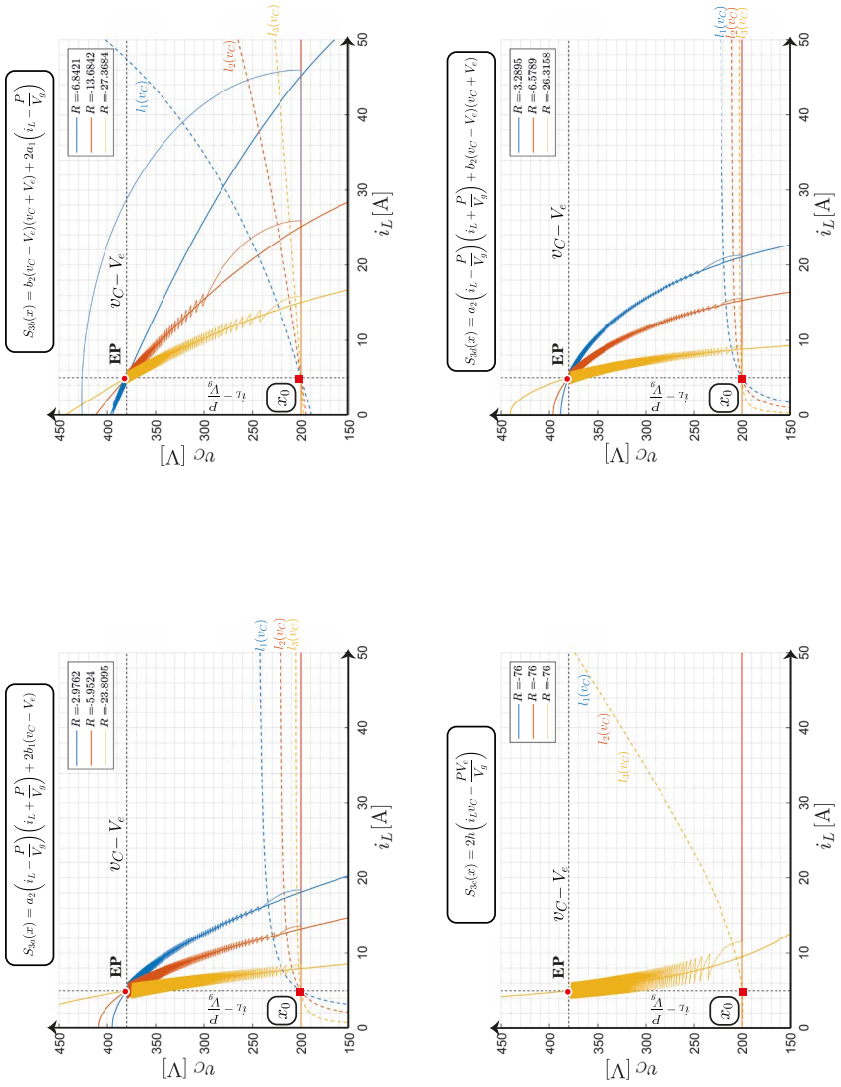

Fig. 2.15: ESM region of the conic surfaces $S_3(x)$ for three values of R.

The same results can be seen with the conical surfaces $S_3(x)$ expressed in (2.51) and seen as a set in Figure 2.15. If the expressions (2.31) and (2.32) are rearranged in terms of the incremental resistance, the expression (2.54) is retained, which guarantees a general description for ESM region for the polynomial surfaces that have been studied so far.

Regarding the quick reaching of the surface, the quadratic surfaces yield a larger ESM region with respect to the affine ones under similar $r(x)\Big|_{Xe}$ values, the ones with the best results being those with quadratic term of current such as the surfaces $S_{3a}(x)$ and $S_{3d}(x)$. The surface $S_{3c}(x)$ leads a to unique region.

2.3.3 Effect of conduction losses at EP

It has to be pointed out that our analysis is based on the lossless model given by (2.1), so it can be expected that parasitic resistances modify the theoretical start-up trajectory in a laboratory prototype. In order to estimate the influence of the parasitic resistances in reaching the EP, we have introduced a resistance R_L in series with the inductor in the converter model, and defined the steady-state errors $E_i = I_L - P/V_g$ and $E_v = V_C - V_e$, where I_L and V_C are the actual coordinates of the EP. Thus, E_i and E_v will give a measure of the deviation of the actual EP with respect to the ideal EP as illustrated in Fig. 2.16 for E_i, where different values of input voltage and output power together with three values of parasitic resistance R_L have been considered. Note that the expected maximum error is below 3.5%, which for $I_e = 5$ A will be 175 mA.

In addition, error E_v can be derived as a function of E_i from expression (2.51) for the five main surfaces. The results are illustrated in Table 6. Fig. 17 shows the voltage error E_v for the mentioned five curves assuming $R = -15\ \Omega$ and $R = -76\ \Omega$ in all of them. It is worth noting that E_v is mainly defined by R as it was the case in the ideal sliding dynamics. For the operating range illustrated in Fig. 17, no significant differences of E_v can be observed in Fig. 17 for the same value of R, i.e., 1% in the worst case. For small values of either E_i or R, the approximation $E_v = RE_i$ can be used.

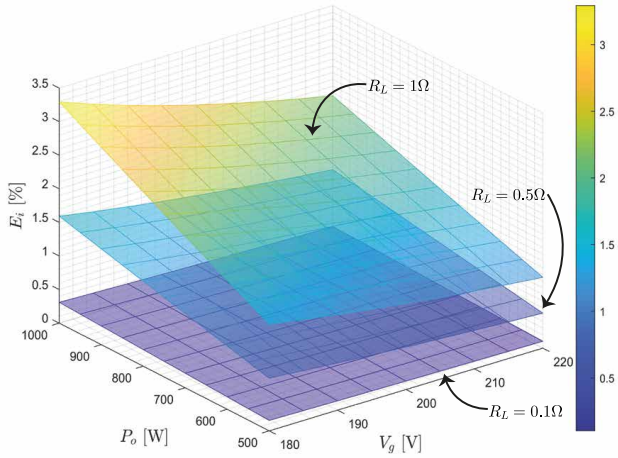

Fig. 2.16: Percentage steady-state current as a function of input voltage and output power, and three values of parasitic resistance.

Table 2.6: Voltage error equation at steady-state.

Surface	**Voltage Error, E_v**	
	Coefficient in (2.29)	**Respect to R**
$S_1(x)$	$-\frac{a_1}{b_1}E_i$	$-RE_i$
$S_{3a}(x)$	$-\frac{a_2}{2b_1}E_i\left(E_i+\frac{2P}{V_g}\right)$	$-RE_i\left(\frac{V_g}{2P}E_i+1\right)$
$S_{3b}(x)$	$-V_e\left(1-\sqrt{1-\frac{2a_1E_i}{b_2V_e}}\right)$	$-V_e\left(1-\sqrt{1-2RE_i}\right)$
$S_{3c}(x)$	$-\frac{V_eE_i}{E_i+\frac{P}{V_g}}$	$-\frac{RE_i}{\left(\frac{V_g}{P}E_i+1\right)}$
$S_{3e}(x)$	$-V_e\left(1-\sqrt{1-\frac{a_2E_i}{b_2V_e}\left(E_i+\frac{2P}{V_g}\right)}\right)$	$-V_e\left(1-\sqrt{1-RE_i\left(\frac{V_g}{2P}E_i+1\right)}\right)$

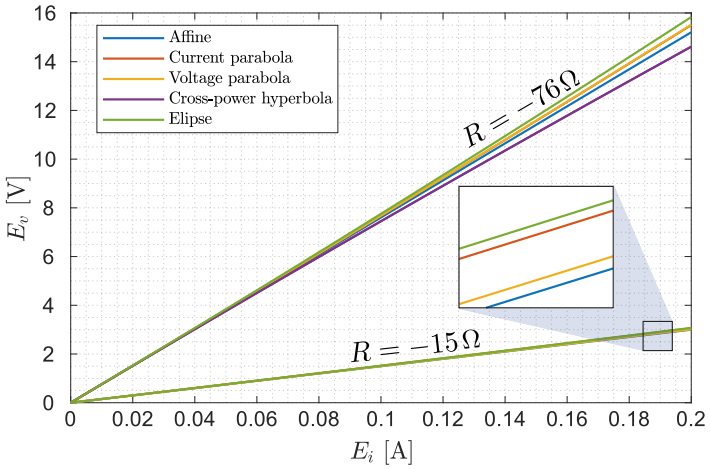

Fig. 2.17: Steady-state voltage error E_v versus steady-state current error E_i for two different values of the incremental resistance R at the EP.

2.4 Experimental results

In order to validate the theoretical analysis in Section 2.3, a 1 kW prototype has been built with the set of parameters sliding surface values shown in Table 2.2. The circuit schematic of the boost converter with CPL and control circuit are illustrated in Fig. 2.18 and Fig. 2.19 respectively. Also, a detailed implementation of switching functions $S_1(x)$ and $S_{3a}(x)$ is depicted in Fig. 2.20. The power semiconductors are a dual diode STPSC40H12C-Y (both D and D_r) in the Fig. 2.9 and a MOSFET STW25NM60ND, which is activated by an isolated driver TLP350.

The currents i_L and i_{CPL} are measured by sensors LEM LA25 with gains of 1/5 and 1/2, respectively, while the input and output voltages are both sensed with LEM LV-25 with a gain of 1/100. The power generator PSI-9750-40 has been used as input voltage source and the CPL has been emulated by the electronic load ELR-9750-44.

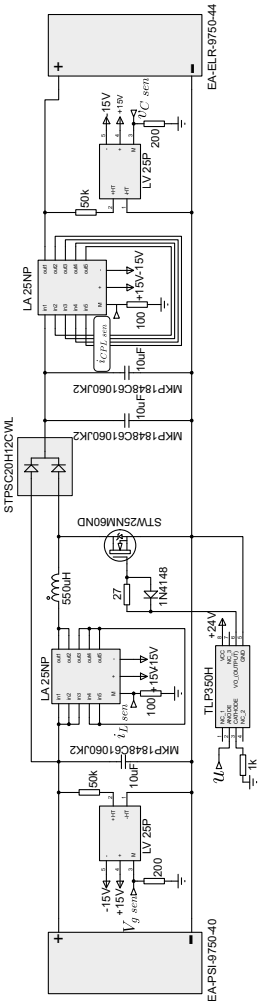

Fig. 2.18: Power stage schematic.

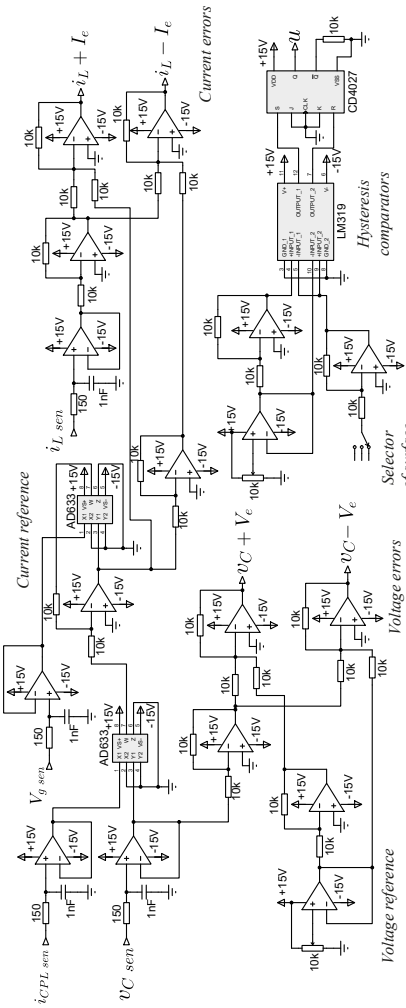

Fig. 2.19: Controller schematic.

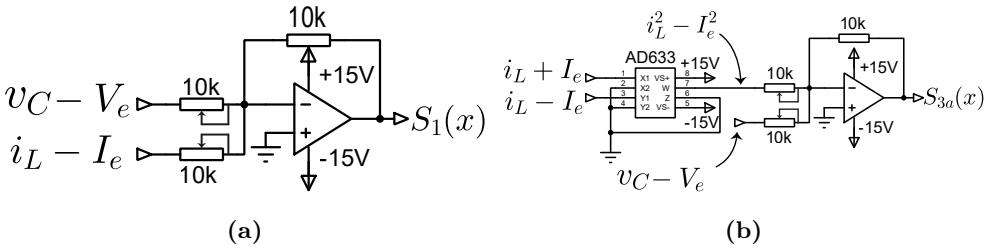

Fig. 2.20: Circuit scheme for the switching functions: (a) $S_1(x)$ and (b) $S_{3a}(x)$.

The control stage has been implemented analogically using the operational amplifier LF324 for simple arithmetic operations, while the CPL power, reference current and both the voltage and current quadratic errors are obtained by means of the IC ADD663. The control law has been implemented with a hysteresis comparator made up of a comparator LM319 and J-K flip-flop 4027, the hysteresis width having been adjusted for a switching frequency of 100 kHz approximately. A dual DC power supply 0-30 V 72-10505 has been used to supply the control stage and the signal data and images have been obtained with a multimeter U3401A and a MDO3024 oscilloscope. A picture of the complete experimental setup is shown in Fig. 2.21.

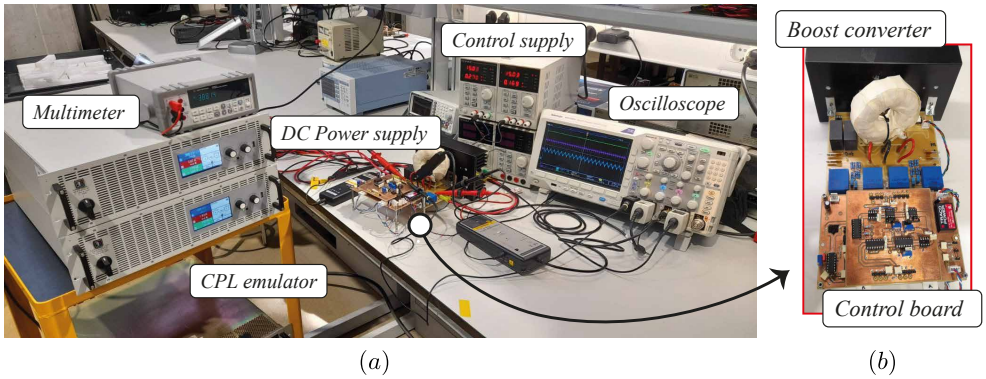

Fig. 2.21: Picture of the experimental setup. (a) overall view, (b) detail showing boost converter and its control board.

2.4.1 Prototype efficiency

Fig. 22 shows the ratio κ of the output power to the power losses κ of the prototype in two operating points, namely around 80 kHz and 100 kHz. The switching function $S_1(x)$ has been used for the test because its incremental resistance does not depend on the EP. Measurements have been carried out over an operating range of 500 W – 1 kW with steps of 50 W. Note that the index κ can be expressed in terms of the efficiency η as follows

$$\kappa = \frac{\eta}{1-\eta} \tag{2.55}$$

It is worth mentioning that using the κ index as a performance metric instead of the efficiency η provides more insight on the losses effect for high values of the efficiency [46]. It can be derived from Fig. 2.22 that the converter efficiency ranges from 96.15% to 97.36% with an average value of 96.87% for 80 kHz and 96.54% for 100 kHz.

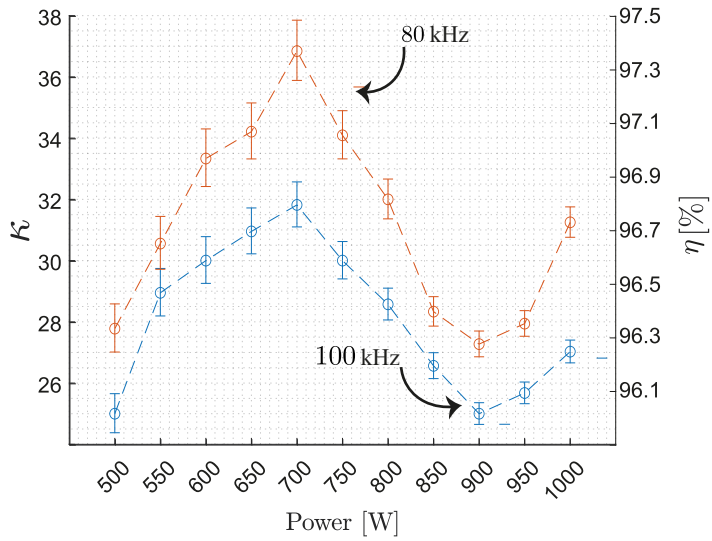

Fig. 2.22: Performance of the boost converter with SMC using the ratio κ.

2.4.2 Measurements of steady-state performance

Fig. 2.23 illustrates the steady-state voltage error caused by conduction losses in the converter. A load of 750 W has been taken as a nominal reference to determine the percentage deviation of the output voltage with respect to V_e, i.e., $V_c\big|_{750\ w} = 380\ V$. Fig. 2.23a illustrates the influence of the incremental resistance over the steady-state voltage error in the case of $S_1(x)$ switching function and three values of the incremental resistance R. The increase in resistance results in a proportional increase of E_v, which confirms the theoretical analysis. The maximum value of error corresponds to $R = -120\ \Omega$ and is around 3% implying a variation of ± 11.4 V.

On the other hand, Fig. 2.23b shows a comparison between the affine and the current parabola switching functions with the same incremental resistance $R = -15\ \Omega$ and equal nominal power of 750 W. In contrast to the switching function of degree one, the incremental resistance of all quadratic switching functions depends on the EP. According to the theoretical estimations, the incremental resistance changes from $-10\ \Omega$ to $-20\ \Omega$ within the range of operation.

2.4.3 Measurements of dynamic performance

The steady-state measurements show that switching function $S_1(x)$ with $R = -15\ \Omega$ exhibits the best performance. For that reason, that switching function with the same incremental resistance has been selected to measure the response of the regulated system to disturbances in input voltage V_g and output power P. A PSIM© simulation with the parameter values shown in Figs. 2.18-2.20 and the inclusion of the measured series parasitic resistance of the inductor (0.6 Ω) is used to compare the theoretical predictions with the experimental results. Fig. 2.24 illustrates the good agreement between both simulated and experimental results of the converter loaded with a 750 W CPL in the response to repetitive input voltage variations taking place every 50 ms.

The input voltage variation between 180 V and 220 V is symmetrical with a slope of $4V/ms$. The current reference, consequently, changes between 4.16 A and 3.41 A. When the disturbance varies gradually, the inductor current follows the reference, and the output voltage does not exhibit any overshoot. Nonetheless, the steady-state output voltage changes from 380.66 V to 384.39 V for input voltage values of 180 V and 220 V respectively, which represents

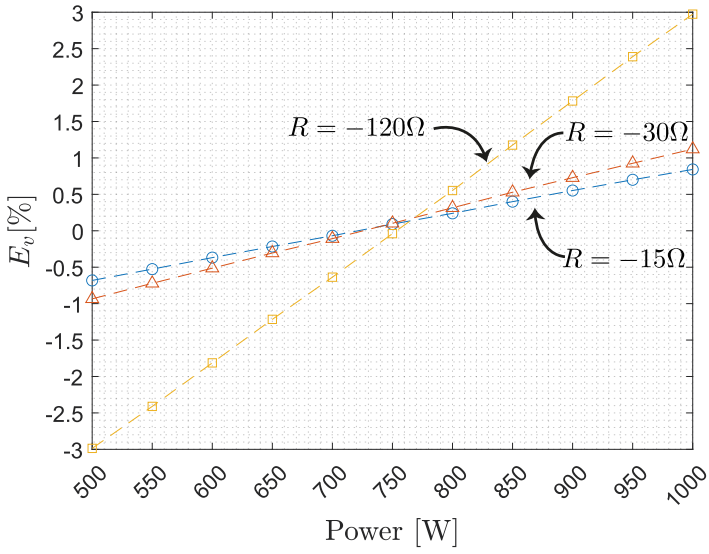

(a)

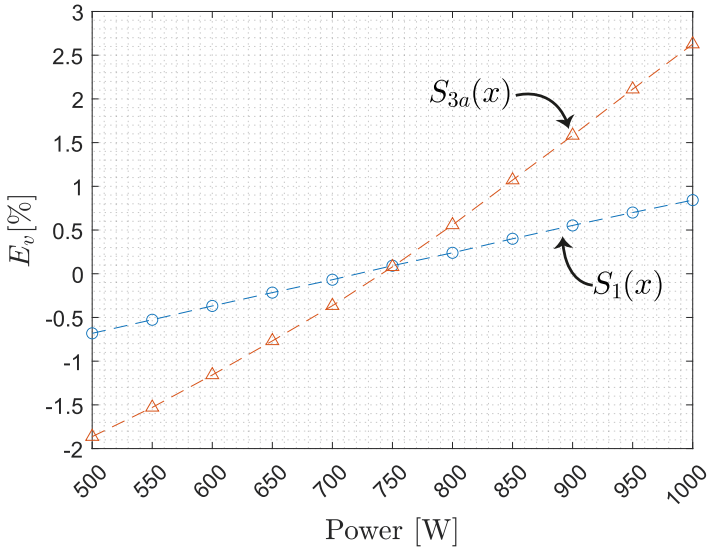

(b)

Fig. 2.23: Static voltage error: (a) control with $S_1\,(x)$ and three values of incremental resistance and (b) Effect of the equal value of the incremental resistance $R = -15\ \Omega$ in switching function $S_1\,(x)$ and $S_{3a}\,(x)$.

a steady-state error of 1% with respect to the output voltage. Fig. 2.25 and Fig. 2.25 show the corresponding steady-state waveforms for the two operating points.

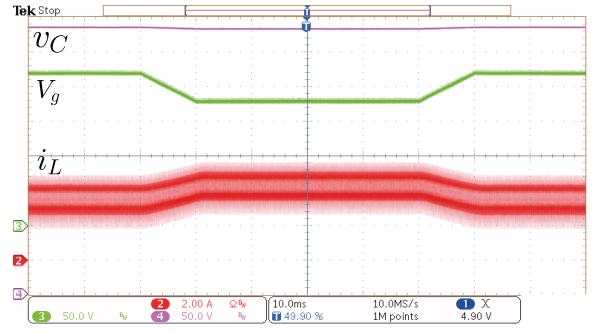

(a)

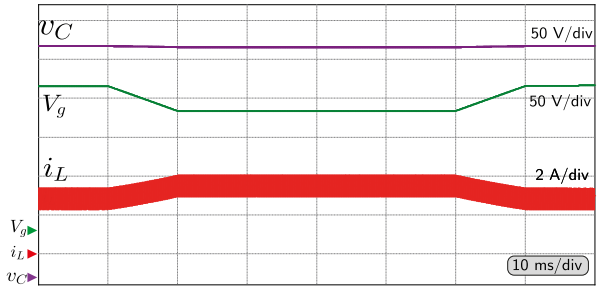

(b)

Fig. 2.24: Transient response for input voltage variations from $V_g = 180\ V$ up to $V_g = 220\ V$: (a) Experimental, and b) PSIM© simulation.

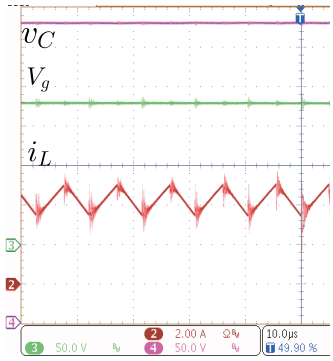

(a)

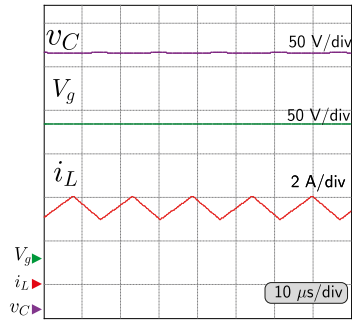

(b)

Fig. 2.25: Steady-state waveforms of the converter with SMC for $V_g = 180\ V$ and $P = 750\ W$. (a) Experimental and (b) PSIM© simulation.

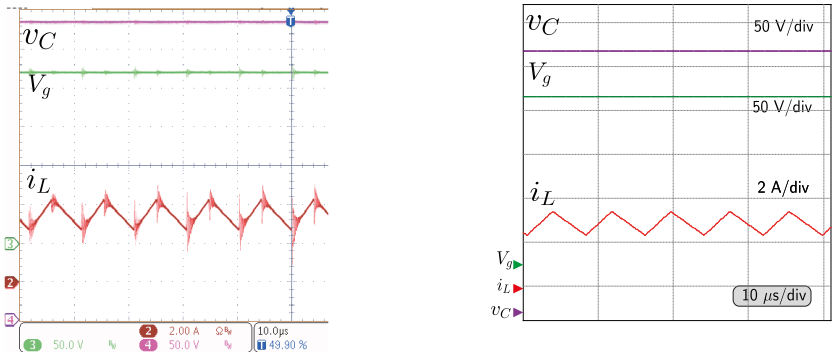

Fig. 2.26: Steady-state waveforms of the converter with SMC for $V_g = 220\ V$ and $P = 750\ W$. (a) Experimental and (b) PSIM© simulation.

Finally, Fig. 2.27 shows the transient response to repetitive abrupt changes of the power load between 500 W and 1 kW with a period 50 ms. Similar results are observed in both simulation and measurements, the settling time being 3 ms in both cases. The average steady-state error of the output voltage is 3.84 V (1.02%) and the maximum voltage variation is 5.6 V (1.5%).

2.5 Extended notions

2.5.1 Control versatility and performance under other types of loads

The development of the proposed SMC has been focused on a boost converter with CPL because this is the worst-case scenario in comparison to other types of canonical loads such as RL or CCL presented in the introduction.

Fig. 2.28 and Fig. 2.29 show the PSIM© simulated response of the boost converter with SMC and a switching affine surface $S_1(x) = 3(i_L \breve{} P/Vg) + 0.2(v_C - V_e)$ to abrupt changes of RL and CCL, respectively. The values of resistance and current loads have been selected to correspond to power changes between 500 W and 1 kW like in the CPL case in section 2.4.3. Also, the same circuitry for measurement of power and input voltage depicted in Fig. 2.18 has been used in simulation. In both cases, similar steady-state and transient-state responses are obtained, which in turn coincide with the response in the CPL case to the power variation from 500 W to 1 kW in Fig. 2.27.

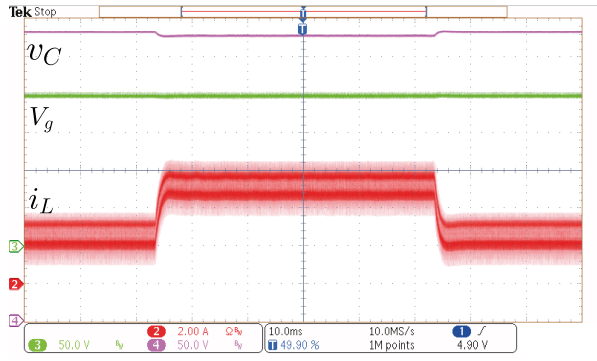

(a)

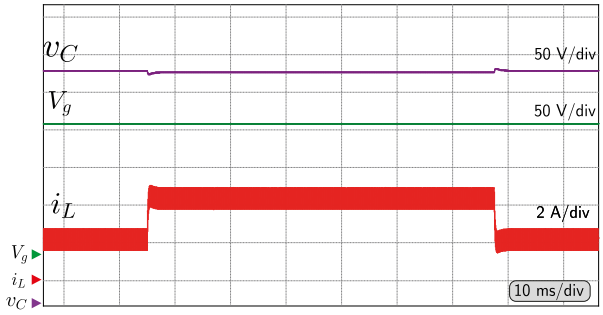

(b)

Fig. 2.27: Transient response for abrupt load power variations between 500 W and 1 kW: (a) Experimental and (b) PSIM© simulation.

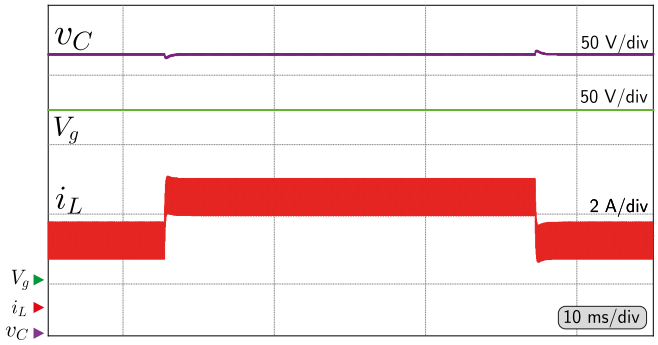

Fig. 2.28: PSIM© simulation of the boost converter with SMC supplying a RL. Response to a step load change between 288.8Ω and 144Ω.

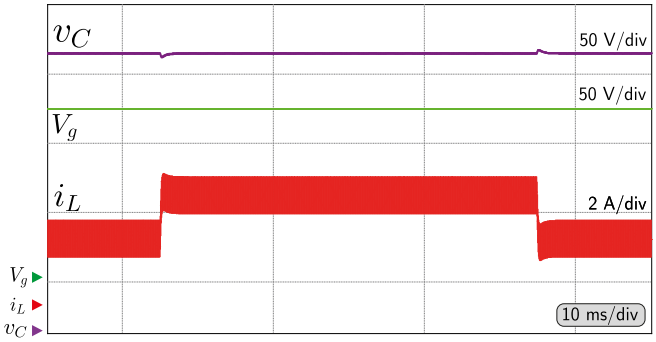

Fig. 2.29: PSIM© simulation of the boost converter with SMC supplying a CCL. Response to a step load change between 288.8Ω and 144Ω.

Similarly, Fig. 2.30 and Fig. 2.31 show equal transient response to input voltage gradual variation between 180 and 220 V in the RL and CCL case respectively. As in the CPL case, in both responses the inductor current absorbs the disturbance effect, while the output voltage is regulated.

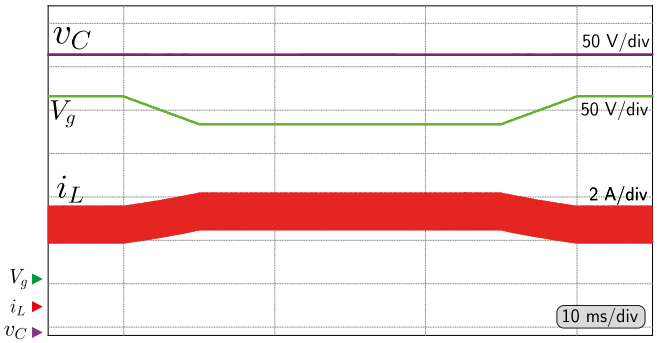

Fig. 2.30: PSIM© simulation of the boost converter with SMC supplying a RL. Response to variations over input voltage from 180 V to 220 V.

The similar performance in the three types of loads is due to the way I_e is calculated within the switching surface (2.8) using instantaneous measurement of P and V_g, this producing an adaptive reference in correspondence with the EPL in each load as evidenced by following expression.

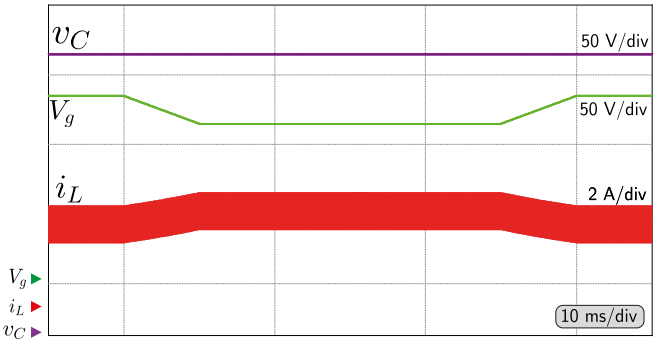

Fig. 2.31: PSIM© simulation of the boost converter with SMC supplying a CCL. Response to variations over input voltage from 180 V to 220 V.

$$I_e = \frac{P}{V_g} = \frac{I_o v_C}{V_g} = \frac{{v_C}^2}{RV_g} \tag{2.56}$$

Fig. 2.32 shows the EPL and the trajectories for a CPL, CCL, and RL from null initial conditions to EP, where the output power in steady-state is equal to 1 kW for the three cases. Complementary, Fig. 2.33 provides the power time-response associated to the different state trajectories until reaching the corresponding equilibrium value. For CCL and RL , the adaptive current reference produces a translation between null load (zero W) and nominal power, allowing the surface to be reached earlier. Eventually, regardless of the type of load, the converter reaches EP, where all EPLs intersect. Finally, Fig. 2.34 illustrates the difference in terms of current and voltage for each type of loads corresponding to Fig. 2.32. As expected, the inrush current in active loads like CPL and CCL is larger than in passive ones. The CPL is the worst case because imposes a stricter demand of power respect the others. However, the dynamic behavior after reaching the affine surface is very similar in all cases.

In conclusion, the proposed technique of the polynomial surfaces with adaptive current reference allows controlling any type of static load, for either constant or variable power demand provided that the maximum power condition for stability is fulfilled.

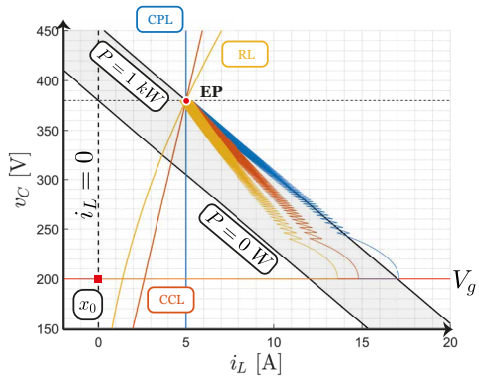

Fig. 2.32: Trajectories of the three canonical loads from null initial conditions to EP.

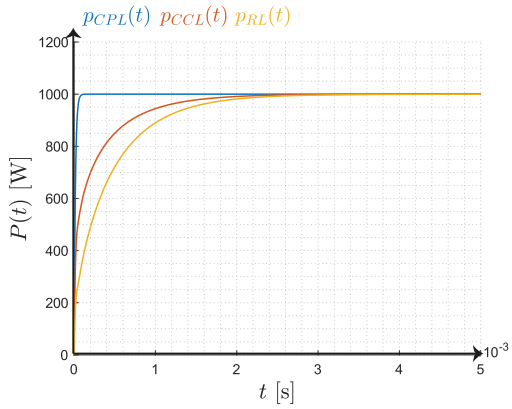

Fig. 2.33: Measured power response for each type of canonical load corresponding to the state trajectories to EP.

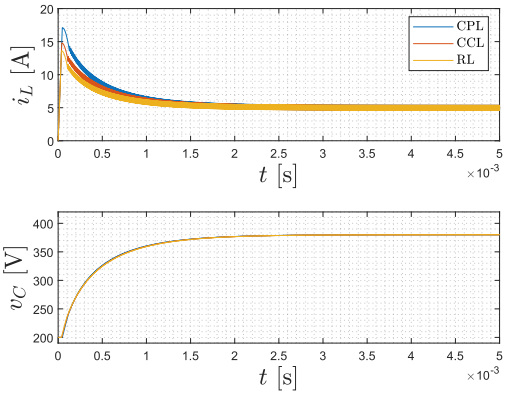

Fig. 2.34: Current and voltage of three canonical loads presented in Fig. 2.32.

2.5.2 Implicit functions

This chapter has been focused on polynomial surfaces in order to propose a systematic procedure with fixed coefficients. The goal has also been achieving consistent and generalized results, both from the analytical point of view and in terms of their real implementation. In addition, it has to be pointed out that some results can be extrapolated to other types of functions expressing curves in the phase plane. In particular, we refer to the conditions of the surface exhibiting a negative slope around the desired EP.

In general, the polynomial surfaces studied are included in implicit functions. Thus, it can be assumed that any implicit function formed with the state variables and the appropriate coefficients will result in a surface that guarantees stable control for a boost converter with CPL.

As a matter of example to support this hypothesis, let's consider the following parabolic surface

$$\Sigma_4 = \{x|\ S_4\ (x) = 0\} \tag{2.57a}$$

$$S_4\,(x) = (v_C - MV_g) - \frac{(V_e - MV_g)\,{V_g}^2}{P^2} i_L^2 \tag{2.57b}$$

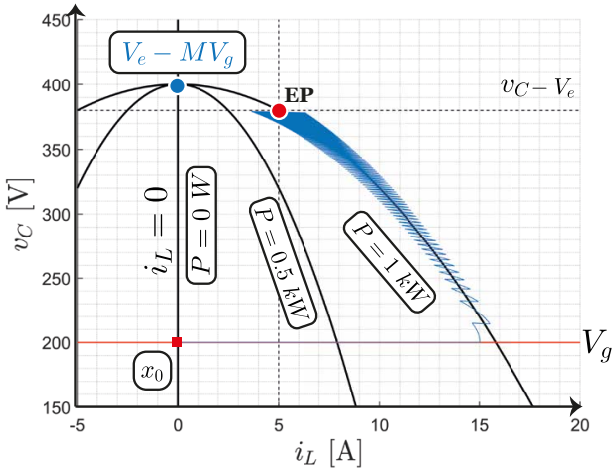

Fig. 2.35: Implicit function in a parabolic surface.

In contrast to polynomial surfaces, $S_4(x)$ has a time-varying coefficient due to the measured current reference V_g^2/P^2. Fig. 2.35 presents the surface $S_4(x)$ on the phase plane. It can be deduced from a geometrical inspection and taking into account the condition of the incremental resistance at negative EP that $(V_e - MV_g) < 0$.

Table 2.7 summarized the parameters and sliding conditions for the existence of sliding motions using the surface $S_4(x)$.

Table 2.7: Parameters and sliding conditions for $S_4(x)$.

Parameter or condition	**Equation**	
Parameter M	$M > \dfrac{V_e}{V_g}$	(2.58)
Sliding surface coefficient	$\Upsilon = \dfrac{(V_e - MV_g)\,{V_g}^2}{P^2} < 0$	(2.59)
EMS region	$i_L < \dfrac{\frac{LP^3}{v_C}}{LP^2 - 2cV_g^2(MV_g - V_e)(V_g - V_e)}$	(2.60)
Equivalent control u_{eq4}	$1 - \dfrac{\frac{P}{v_C} + \frac{2\Upsilon C V_g}{L} i_L}{i_L\left(1 + \frac{2\Upsilon C}{L} v_C\right)}$	(2.61)
Ideal sliding dynamic	$i_L = \sqrt{\dfrac{v_C - MV_g}{\Upsilon}}$	(2.62)
	$\dfrac{dv_C}{dt} = \dfrac{\frac{2\Upsilon}{L} V_g \left(i_L - \frac{P}{V_g}\right)}{1 + \frac{2\Upsilon C}{L} v_C}$	(2.63)
Linearized around at EP	$\dfrac{d\widetilde{v_C}}{dt} = \dfrac{\frac{1}{L}\frac{V_g^2}{P}}{1 + \frac{2\Upsilon C V_e}{L}} \widetilde{v_C}$	(2.64)
Incremental resistance	$r_4(x) = 2\Upsilon i_L < 0$	(2.65)
	$R_4 \triangleq r_4(x)\Big\vert_{X_e} = \dfrac{2(MV_g - V_e)V_g}{P}$	(2.66)

The system will be stable if the denominator in (2.64) is positive, this setting a maximum power limit. If we rewrite the limit by introducing the incremental resistance at EP defined in (2.66), the same expressions for polynomial surfaces will be obtained, and a general stability condition for any implicit function used as a sliding surface can be proposed as follows

$$P < R_4 \frac{CV_eV_g}{L} \triangleq P_{max} \tag{2.67}$$

2.6 Conclusions

Sliding surfaces of polynomial type constitute a simple and reliable alternative for SMC of a boost converter loaded with a CPL. Combining the natural unstable trajectories of the converter in the plane $i_L - v_C$ for ON and OFF states with an appropriate switching law in a polynomial–type sliding surface results in a stable trajectory leading the average dynamics to a desired EP.

From a generic formulation of the surface with the previous features, the analysis of the existing conditions for sliding motions and the study of the subsequent stability in polynomial curves of degree zero, degree one and degree two have demonstrated that all feasible surfaces must exhibit a negative incremental resistance $r(x)|_{EP}$ at the EP smaller than an equivalent resistance imposed by the values of the CPL power, the input voltage and the desired output voltage.

The incremental resistance at the EP is also the main distinctive feature when measuring both static and dynamic performance of the regulated converter as reveals a comparative analysis among five switching functions, namely, an affine function, a current parabola, a voltage parabola, a cross-power hyperbola, and an ellipse. In particular, a conduction loss analysis for a plausible rank of values of the inductor parasitic series resistance has shown that the resulting output voltage steady-state error does not depend of the type of the sliding curve used in the control but it is rather proportional to the inductor current steady-state error, the proportionality constant being the incremental resistance at the EP. Regarding the dynamic behavior, the ideal sliding dynamics is a first order system with a time constant proportional to the incremental resistance at the EP.

The mentioned comparative analysis has demonstrated that quadratic sur-

faces result in both small inrush current and settling time except the cross-power hyperbola that has presented a low general performance.

The general expression of the conic curve given in (2.51) has allowed the reduction of the required number of operations to implement the switching surfaces. Thus, only two summers have been used for $S_1(x)$, three summers and one multiplier for $S_{3a}(x)$ and $S_{3b}(x)$, and five summers and two multipliers for $S_{3d}(x)$. The ideal switching decision required by SMC, which theoretically leads to an infinite switching frequency, has been substituted by a hysteresis comparison, resulting in a finite switching frequency. It is worth mentioning that the chattering produced by the comparators is inherent to the nature of the switching conversion. The energy is absorbed from the input source in a fast repetitive action to be stored in the inductor magnetic field and then transferred to the dc output load. This mechanism is the foundation of power conversion and it is also the way that chattering (or ripple) is produced. Dc-dc switching converters are variable structure systems where classical (first-order) SMC is the natural way to regulate them.

PSIM© simulations and experimental results have verified the theoretical predictions. The static performance has been measured in terms of steady-state output voltage regulation error and prototype efficiency. The dynamic performance, in turn, has been evaluated for large-signal variations of input voltage and output power.

A final global assessment that takes into account static and dynamic performance as well as implementation allows concluding that the best polynomial alternative for the sliding surface is the affine function.

UNIVERSITAT ROVIRA I VIRGILI
A SLIDING MODE APPROACH TO CONTROL POWER SINKS AND POWER SOURCES IN DC-DC SWITCHING CONVERTERS
David Alejandro Zambrano Prada

Chapter 3

Sliding mode control with power estimation for a boost converter with CPL

Introduction

Chapter 2 has analyzed in detail the sliding mode control of a boost converter with CPL using polynomial surfaces. This approach has provided a systematic and generalized methodology, resulting in a robust control, a simple implementation, and a fast recovery of the regulated voltage in response to external disturbances.

Nevertheless, there are two drawbacks in the proposed control:

(i) There is a non-zero voltage error at steady state due to losses in the converter. The computation of the sliding surface is established considering the ideal power balance of the converter, which does not take into account the losses. Since there is no integrating action that reduces to zero the difference of the output voltage with respect to its reference, a steady-state error results reflecting the actual power balance.

(ii) The current reference requires the instantaneous value of the CPL power, which in our implementation is achieved by measuring it directly.

Regarding point (i), small values of the steady-state voltage error below 2%. can be obtained with the appropriate choice of the sliding surface coefficients.

In the case of the point (ii), the need to measure the instantaneous power requires at least one additional sensor. In the case of the boost converter, this implies a current sensor at the output and a filtering stage due to the discontinuity of the signal. To avoid the measurement, two approaches are found in the literature.

Most of the existing controllers are designed using the nominal value of the CPL power in the converter model, so the measure of the robustness for a large variation of that parameter indicates the controller performance quality. Their design requires a complex off-line mathematical analysis to establish the optimal value of the controller parameters, which are not modified once the converter operation starts [47].

In a clear-cut contrast, adaptive controllers estimate the value of the CPL power online to modify the controller parameters accordingly. Therefore, they deal initially with an uncertain parameter that should be included in the control strategy. An example of that is the output voltage regulation of a buck-boost converter with an unknown power load analyzed in [48] and modified in [49] by means of a change of coordinates and partial linearization. The latter procedure is extended to a buck converter [50], which has been the subject of several studies, the estimation of the CPL power being one of their main features [51]–[53] together with the use of high-order sliding mode observers [54], [55].

Similarly, some papers have been devoted to the boost converter with uncertain power in the CPL. Namely, the energy shaping control approach used in [48], [49] is extended in [56] to a boost converter while the use of a nonlinear disturbance observer confers adaptive behavior on a passivity-based control in [57] and provides feedforward compensation to regulate the output voltage in [58]. The mentioned adaptive controllers are characterized by a rigorous continuous-time theoretical analysis and by a complex digital implementation in which the lack of a previous discretization phase makes the experiments interpretation difficult.

Regarding the implementation using analog electronics, the main antecedent is the pulse width modulation–based nonlinear control presented in [59], in which the power of the CPL is estimated by means of the integral of a nonlinear function of the output voltage error. In that work the analysis is based on a continuous–time model.

3.1 Integral SMC with polynomial surface for zero voltage error

Fig. 3.1 shows the boost converter where a resistor R_L in series with inductor L is introduced to model the effect of the parasitic resistances. This model concentrates all the conduction power losses of the converter or P_L.

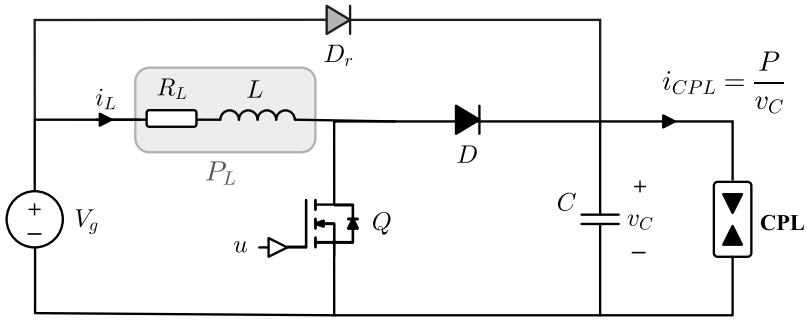

Fig. 3.1: Boost converter with complementary diode supplying a CPL.

In order to reduce to zero with the influence of parasitic resistances in the voltage regulation, the sliding switching surface $\Sigma_1 = \{x|\ S_1(x) = 0\}$ is modified the by adding the integral of the voltage error $e_v = v_C - V_e$ multiplied by a constant.

Considering the properties for polynomial surfaces analyzed in Chapter 2, the affine surface is taken for simplification.

$$\Sigma_{i1} = \{x|\ S_{i1}(x) = 0\} \tag{3.1a}$$

$$S_{i1}(x) = a\left(i_L - \frac{P}{V_g}\right) + b\left(v_C - V_e\right) + \beta \int_{-\infty}^{t} \left(v_C - V_e\right) dt \tag{3.1b}$$

Thus, we can rearrange the system of equations in (2.1) in order to introduce the dynamics of the integral of the voltage error as a new state variable.

$$L\frac{di_L}{dt} = V_g - (1-u)\,v_C \tag{3.2a}$$

$$C\frac{dv_C}{dt} = i_L\,(1-u) - \frac{P}{v_C} \tag{3.2b}$$

$$\frac{dx_3}{dt} = \beta\,(v_C - V_e) \tag{3.2c}$$

From surface (3.1), the expression of its derivative $\dot{S_{i1}}(x)$ is derived

$$\dot{S_{i1}}\,(x) = \left(\frac{aV_g}{L} - \frac{aR_L i_L}{L} - \frac{bP}{Cv_C}\right) - \left(\frac{av_C}{L} - \frac{bi_L}{C}\right)(1-u) + \beta\,(v_C - V_e) \tag{3.3}$$

The sliding dynamics will exist if the reachability condition $S_{i1}\,(x)\,\dot{S}_{i1}(x) < 0$ is satisfied. Particularizing expression (3.3) for $u = 0$ and $u = 1$ leads to the following two expressions

$$\lim_{S(x)\to 0^+} \dot{S}_1\ \ (x)\Big|_{u=0} = \left(\frac{aV_g}{L} - \frac{bP}{Cv_C}\right) + \left(\frac{bi_L}{C} - \frac{av_C}{L}\right) + \beta\,(v_C - V_e) < 0 \tag{3.4a}$$

$$\lim_{S(x)\to 0^-} \dot{S}_1(x)\Big|_{u=1} = \left(\frac{aV_g}{L} - \frac{bP}{Cv_C}\right) + \beta\,(v_C - V_e) > 0 \tag{3.4b}$$

By combining them into a compact expression, we obtain the inequality (3.5), which describes the ESM region.

$$i_L < \frac{P}{v_C} + \frac{RC}{L}\,(v_C - V_g) - \beta(v_C - V_e) \tag{3.5}$$

Within the ESM and after reaching the switching surface, the trajectory of the ideal dynamics satisfies the invariance conditions $S_1\,(x) = 0$ and $\dot{S}_1\,(x) = 0$ when it slides along the surface. Under these operating conditions, the dynamics of the system corresponds to the ideal sliding dynamics by replacing the

equivalent control (3.6) in (3.2). At this point, it is worth to note the reduction of dynamical order of the system to a second order.

$$u_{1_{eq}} = 1 - \frac{\frac{aV_g}{L} - \frac{aR_L i_L}{L} - \frac{bP}{Cv_C} + \beta\left(v_C - V_e\right)}{\frac{av_C}{L} - \frac{bi_L}{C}} \tag{3.6}$$

$$i_L = \frac{P}{V_g} - \frac{\left(v_C - V_e\right)}{R} - \frac{x_3}{a} \tag{3.7a}$$

$$\frac{dv_C}{dt} = \frac{\frac{aV_g}{CL}\left(i_L - \frac{P}{V_g} - \frac{R_L {i_L}^2}{V_g}\right) + \beta i_L\left(v_C - V_e\right)}{\frac{av_C}{L} - \frac{b}{C}\left(\frac{P}{V_g} - \frac{\left(v_C - V_e\right)}{R} - \frac{x_3}{a}\right)} = \frac{N\left(i_L, v_C, x_3\right)}{D\left(i_L, v_C, x_3\right)} \triangleq y_1(t) \tag{3.7b}$$

$$\frac{dx_3}{dt} = \beta\left(v_C - V_e\right) \triangleq y_2(t) \tag{3.7c}$$

At EP, the final value of the voltage error integral function (in $t = T_e$ and $v_C - V_e = 0$) will depend on the starting point and the value of the constant β. Without a set-point value, it is fixed to a constant as expressed in (3.8).

$$X_3 = \langle x3 \rangle\Big|_{X_e} = \beta \int_{-\infty}^{T_e} \left(v_C - V_e\right) dt = -F \tag{3.8}$$

Thus, the state variables in steady-state will take the following values.

$$I_L = \frac{P}{V_g} + \frac{F}{a} \tag{3.9a}$$

$$v_C = V_e \tag{3.9b}$$

Linearizing the ideal sliding dynamics at EP requires the calculation of partial derivatives respect to v_C and x_3 of i_L, y_1 and y_2. In sliding motion, i_L is a function of these two variables and its partial derivatives are constants as shown

in (3.10).

$$\frac{\partial i_L}{\partial v_C} = -\frac{1}{R} \tag{3.10a}$$

$$\frac{\partial i_L}{\partial x_3} = -\frac{1}{a} \tag{3.10b}$$

For y_1 and y_2, the general expression (3.11) with $j = 1, 2$ presents the reduced equation for the partial derivatives because $N(i_L, v_C, x_3) = 0$ at EP.

$$\left.\frac{\partial y_j}{\partial v_C}\right|_{X_e} = \left.\frac{\left(\frac{\partial N(i_L, v_C, x_3)}{\partial v_C} + \frac{\partial N(i_L, v_C, x_3)}{\partial iL}\frac{\partial i_L}{\partial v_C}\right)}{D(i_L, v_C, x_3)}\right|_{X_e} \tag{3.11a}$$

$$\left.\frac{\partial y_j}{\partial x_3}\right|_{X_e} = \left.\frac{\left(\frac{\partial N(i_L, v_C, x_3)}{\partial x_3} + \frac{\partial N(i_L, v_C, x_3)}{\partial iL}\frac{\partial i_L}{\partial x_3}\right)}{D(i_L, v_C, x_3)}\right|_{X_e} \tag{3.11b}$$

Finally, the small signal dynamics around EP will be expressed as follows

$$\frac{d\tilde{v_C}}{dt} = -\frac{\frac{V_g}{CR}\left(1 - \frac{2I_L R_L}{V_g} - \frac{\beta RL}{aV_g}I_L\right)}{V_e - \frac{L}{RC}\left(\frac{P}{V_g} + \frac{F}{a}\right)}\tilde{v_C} - \frac{\frac{V_g}{Ca}\left(1 - \frac{2I_L R_L}{V_g}\right)}{V_e - \frac{L}{RC}\left(\frac{P}{V_g} + \frac{F}{a}\right)}\tilde{x_3} = -\frac{B}{\Lambda}\tilde{v_C} - \frac{\Gamma}{\Lambda}\tilde{x_3} \tag{3.12a}$$

$$\frac{d\tilde{x_3}}{dt} = \beta\tilde{v_C} \tag{3.12b}$$

Therefore, the Jacobian matrix corresponding to (3.12) will be given by

$$A_{I1} = \begin{bmatrix} \left.\frac{\partial y_1}{\partial v_C}\right|_{X_e} & \left.\frac{\partial y_1}{\partial x_3}\right|_{X_e} \\ \left.\frac{\partial y_2}{\partial v_C}\right|_{X_e} & \left.\frac{\partial y_2}{\partial x_3}\right|_{X_e} \end{bmatrix} = \begin{bmatrix} -\frac{B}{\Lambda} & -\frac{\Gamma}{\Lambda} \\ \beta & 0 \end{bmatrix} \tag{3.13}$$

The characteristic equation corresponding to the previous Jacobian matrix is

$$|s\mathbb{I} - A_{I1}| = \begin{bmatrix} s + \frac{B}{\Lambda} & \frac{\Gamma}{\Lambda} \\ -\beta & s \end{bmatrix} = s^2 + \frac{B}{\Lambda}s + \frac{\Gamma\beta}{\Lambda} \tag{3.14}$$

According to (3.14), the system will be stable if all coefficients of the characteristic equation are positive. For $\Lambda > 0$, we obtain

$$P < \frac{RCV_eV_g}{L} - \frac{V_gF}{a} = P_{max} - P_L \tag{3.15}$$

Note that (3.15), extends the expression obtained in (2.19) relative to the maximum allowed power without parasitic resistances. By considering the power losses, the new power limit is reduced by the magnitude of the power losses. It is worth to note that the value of P_L is proportional to X_3 as it can see in (3.16).

$$P_L = \frac{V_gF}{a} = -\frac{\beta V_g}{a}\int_{-\infty}^{T_e}(v_C - V_e)\,dt \tag{3.16}$$

For $B > 0$, we find the maximum limit for I_L.

$$I_L < \frac{V_g}{2R_L} \triangleq I_{Lmax} \tag{3.17}$$

And for $B > 0$, the maximum value of the parameter β is given by

$$\beta < \frac{bV_g}{LI_L}\left(1 - \frac{2I_LR_L}{V_g}\right) \triangleq \beta_{max} \tag{3.18}$$

We can deduce from (3.16) that the state variable $x_3(t)$ is an estimation of the power losses in the converter. Therefore $S_1(x)$ can be rewritten as follows

$$S_1(x) = a\left(i_L - \frac{P + \hat{P}_L}{V_g}\right) + b\left(v_C - V_e\right) \tag{3.19}$$

with

$$\hat{P}_L = -\frac{\beta V_g}{a}\int_{-\infty}^{t}\left(v_C - V_e\right)dt \tag{3.20}$$

In the equations above, the superscript $(\wedge)$ stands for the estimation of a power value. Fig. 3.2 shows the PSIM© simulation of the power loss estimation in the converter with the parameters´ values of Table 3.1 . The figure illustrates the transition from an EP with a load of 1 kW to another load of 750 W for three values of β, where a parasite resistance $R_L = 0.5\ \Omega$ generates a power loss of 12.85 W and 7.20 W, respectively. In the three cases, the estimated power reaches the actual value, the best performance is obtained for $a = 100$. Higher values of this parameter produce an underdamping behavior and higher peaks in the oscillation.

Table 3.1: Parameters‘ values used in Chapter 2, section 2.2.

Parameter	**Values**
L	500 μH
C	20 μF
P_{CPL}	1 kW
V_g	200 V
V_e	380 V

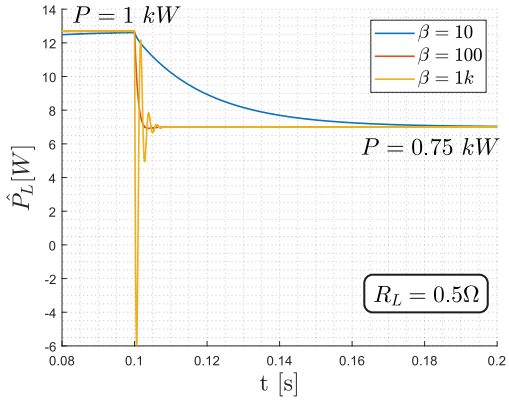

Fig. 3.2: Estimation of power losses for $R_L = 0.5\ \Omega$ from a load change between 1 kW and 750 W with three values of β.

The previous simulation and analysis has tested the transition performance from one equilibrium point to another. Regarding the start-up of the converter from null initial conditions to a load of 1 kW, the power estimation loop has a large deviation during the transient even when an appropriate value of β has been chosen, as can be observed in Fig. 3.3. This dynamics may be appropriate for estimation of larger values of power rather than power losses. In contrast, the inductor current and the capacitor voltage keep close to the surface after reaching it, not being strongly affected by the estimation loop. Fig. 3.4 shows two perspectives of the trajectory of the system, where it is possible to see the translation range of the sliding surface plane $S_{i1}(x)$.

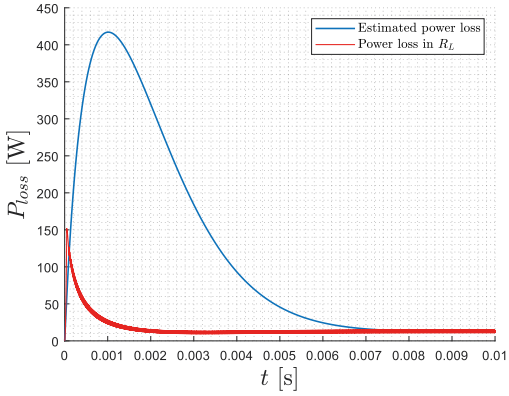

Fig. 3.3: Dynamic of measured power loss in R_L and the estimated power loss $\hat{P}$ from null initial conditions.

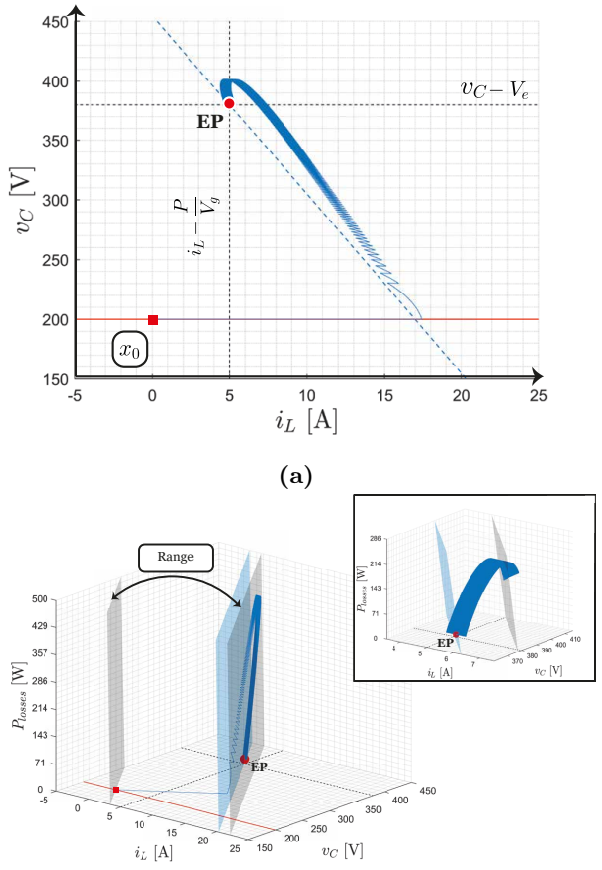

Fig. 3.4: Trajectory from null initial conditions for integral SMC. (a) 2D phase plane, and (b) 3D phase plane view.

3.2 Adaptive sliding controllers with power estimation

3.2.1 Power estimation description

The previous section has demonstrated how a simple integrator loop used in conjunction with a polynomial sliding surface could estimate a fraction of the power flowing through the converter, specifically the power losses. By observing expression (3.19), and the adaptive property of the current reference, we can

assume that the same methodology would estimate the total power handled by the converter by replacing $P + P_L$ by a single estimated parameter.

Taking all this into consideration, a linear power estimator is now presented, adding it to the system description in (2.1), where the extended state variables will be $x = \left[i_L,\ v_C,\ \hat{P}\right]^\intercal$. For convenience of the subsequent analysis, power losses are neglected, i.e., $P_L = 0$.

$$L\frac{di_L}{dt} = V_g - (1-u)\, v_C \tag{3.21a}$$

$$C\frac{dv_C}{dt} = i_L\,(1-u) - \frac{P}{v_C} \tag{3.21b}$$

$$\frac{d\hat{P}}{dt} = -\beta\,(v_C - V_e) \tag{3.21c}$$

3.2.2 Polynomial surface of second degree

Chapter 2 has demonstrated the versatility of the general analysis of polynomial surfaces, which has allowed the extrapolation of the results of a surface of higher degree to surfaces of lower degree. In order to synthesize the current analysis, the polynomial surface of degree two is chosen now to cover all the surfaces studied and analyzed in that chapter.

Then, the general sliding surface of second degree in (2.29) is modified with the power estimation loop as follows

$$\Sigma_{p2} = \{x|\ S_{p2}\,(x) = 0\} \tag{3.22a}$$

$$\begin{aligned} S_{p2}\,(x) =& a_2\left(i_L^2 - \frac{\hat{P}^2}{V_g^2}\right) + b_2\left(v_C^2 - V_e^2\right) + 2\left(h i_L v_C - \frac{\hat{P}V_e}{V_g}\right) \\ &+ 2a_1\left(i_L - \frac{\hat{P}}{V_g}\right) + 2b_1\,(v_C - V_e) \end{aligned} \tag{3.22b}$$

where $\hat{P}$ corresponds to the estimated output power, whose dynamic behavior

is given by (3.21).

3.2.2.1 Conditions of existence and stability of sliding motions

Sliding motions on switching surfaces Σ_{p2} will exist if the condition $S_{2p}(x)\ \dot{S}_{2p}(x) < 0$ is satisfied. From (3.22) the expression for $\dot{S}_{2p}$ is given by

$$\begin{aligned}\dot{S}_{p2}(x) =& \frac{V_g}{L}\left(a_2 i_L + h v_C + a_1\right) - \frac{P}{C v_C}\left(b_2 v_C + h i_L + b_1\right) \\ &+ \frac{\beta\left(v_C - V_e\right)}{V_g}\left(\frac{a_2 \hat{P}}{V_g} + h V_e + a_1\right) - \frac{v_C(1-u)\left(a_2 i_L + h v_C + a_1\right)}{L} \\ &+ \frac{i_L\left(1-u\right)\left(b_2 v_C + h i_L + b_1\right)}{C}\end{aligned} \tag{3.23}$$

The above expression can be written in such a way that it includes the definition of incremental resistance in (2.48) as

$$\dot{S}_{p2}(x) = -\frac{V_g}{L} r(x) - \frac{P}{C v_C} - \frac{\beta\left(v_C - V_e\right)}{V_g}\widehat{r(x)} + (1-u)\left(\frac{v_C}{L} r(x) + \frac{i_L}{C}\right) \tag{3.24}$$

with

$$r(x) = -\frac{a_2 i_L + h v_C + a_1}{b_2 v_C + h i_L + b_1} \tag{3.25}$$

and

$$\widehat{r(x)} = \frac{\frac{a_2 \hat{P}}{V_g} + h V_e + a_1}{b_2 v_C + h i_L + b_1} \tag{3.26}$$

Equation (3.25) corresponds to the incremental resistance of the converter in the phase plane $i_L - v_C$, and equation (3.26) represents its estimation. Thus, there is a region of EMS given by

$$\lim_{S(x)\to 0^+} \dot{S}_1\ (x)\Big|_{u=0} = \frac{V_g}{L} r\,(x) - \frac{P}{Cv_C} - \frac{\beta\,(v_C - V_e)}{V_g}\widehat{r\,(x)} + \frac{v_C}{L} r\,(x) + \frac{i_L}{C} < 0 \tag{3.27a}$$

$$\lim_{S(x)\to 0^-} \dot{S}_1(x)\Big|_{u=1} = -\frac{V_g}{L} r\,(x) - \frac{P}{Cv_C} - \frac{\beta\,(v_C - V_e)}{V_g}\widehat{r\,(x)} > 0 \tag{3.27b}$$

Then, combining the expressions in (3.27) in a compact form, the result in the EMS region is obtained.

$$i_L < l\,(v_C) = \frac{P}{v_C} - \frac{Cr\,(x)\,(v_C - V_g)}{L} + \frac{C\beta\widehat{r\,(x)}\,(v_C - V_e)}{V_g} \tag{3.28}$$

Within the ESM region and after reaching the switching surface, the dynamics along Σ_{2p} guarantees the fulfillment of the invariance condition $S_{2p} = 0$ and $\dot{S}_{2p} = 0$. As a result, the ideal sliding dynamics of the system can be described in terms of an average model, which is based on the equivalent control $u_{p2_{eq}}$ the latter being bounded between 0 and 1, i.e. $0 \leq u_{eq} \leq 1$.

$$u_{p2_{eq}} = \frac{\frac{V_g r(x)}{L} + \frac{P}{Cv_C} + \frac{\beta(v_C - V_e)\widehat{r(x)}}{V_g}}{\frac{v_C r(x)}{L} + \frac{i_L}{C}} \tag{3.29}$$

Introducing the equivalent control (3.29) in (3.21), the ideal sliding dynamics is obtained.

$$i_L = \sqrt{\left(\frac{hv_C + a_1}{a_2}\right)^2 + \frac{\hat{P}^2}{V_g^2} + \frac{2\hat{P}}{V_g}\left(\frac{hv_C + a_1}{a_2}\right) - \frac{b_2}{a_2}\left(v_C^2 - V_e^2\right) - \frac{2b_1}{a_2}\left(v_C - V_e\right)} - \frac{hv_C + a_1}{a_2} \tag{3.30a}$$

$$\frac{dv_C}{dt} = \frac{\frac{V_g i_L r(x)}{L} + \frac{\beta i_L (v_C - V_e)\widehat{r(x)}}{V_g} - \frac{\mathrm{Pr}\,(x)}{L}}{\frac{Cv_C r(x)}{L} - i_L} \triangleq y_3(t) \tag{3.30b}$$

$$\frac{d\hat{P}}{dt} = -\beta\,(v_C - V_e) \triangleq y_4(t) \tag{3.30c}$$

It is worth to note that the system dynamics given in (3.30) is nonlinear. It has to be pointed out that the core of the ideal sliding dynamics is the state variables v_C and P with equations $y_3(t)$ and $y_4(t)$, which corresponds to a second order system. Instead, i_L is a function of v_C and $\hat{P}$ and its partial derivatives correspond to the expressions (3.31) and (3.32).

$$\left.\frac{\partial i_L}{\partial v_C}\right|_{X_e} = r(x)|_{X_e} = \frac{\frac{a_2 P}{V_g} + hV_e + a_1}{b_2 V_e + \frac{hP}{V_g} + b_1} = -\frac{1}{R} \tag{3.31}$$

$$\left.\frac{\partial i_L}{\partial \hat{P}}\right|_{X_e} = \frac{1}{V_g} \tag{3.32}$$

The linearization of the dynamics around $X_e = [I_L^*,\ V_C^*,\ P^*] = [P/V_g,\ V_e,\ P]^\intercal$ leads to the small-signal dynamic model that will be used to determine the stability conditions. Also at this point, the incremental resistance, and its estimation are equal, i.e., $r(x)\big|_{X_e} = \hat{r}(x)\big|_{X_e} = -1/R$. For y_3 and y_4, the general expression (34) with $j = 3, 4$ presents the reduced equation for the partial derivatives because $N\left(i_L, v_C, \hat{P}\right) = 0$ at EP.

$$\left.\frac{\partial y_j}{\partial v_C}\right|_{X_e} = \left.\frac{\left(\frac{\partial N(i_L,v_C,\hat{P})}{\partial v_C} + \frac{\partial N(i_L,v_C,\hat{P})}{\partial i_L}\left.\frac{\partial i_L}{\partial v_C}\right|_{X_e} + \frac{\partial N(i_L,v_C,\hat{P})}{\partial r}\left.\frac{\partial r}{\partial v_C}\right|_{X_e} + \frac{\partial N(i_L,v_C,\hat{P})}{\partial \hat{r}}\left.\frac{\partial \hat{r}}{\partial v_C}\right|_{X_e}\right)}{D\left(i_L, v_C, \hat{P}\right)}\right|_{X_e} \tag{3.33a}$$

$$\left.\frac{\partial y_j}{\partial \hat{P}}\right|_{X_e} = \left.\frac{\left(\frac{\partial N(i_L,v_C,\hat{P})}{\partial \hat{P}} + \frac{\partial N(i_L,v_C,\hat{P})}{\partial i_L}\left.\frac{\partial i_L}{\partial \hat{P}}\right|_{X_e} + \frac{\partial N(i_L,v_C,\hat{P})}{\partial r}\left.\frac{\partial r}{\partial \hat{P}}\right|_{X_e} + \frac{\partial N(i_L,v_C,\hat{P})}{\partial \hat{r}}\left.\frac{\partial \hat{r}}{\partial \hat{P}}\right|_{X_e}\right)}{D\left(i_L, v_C, \hat{P}\right)}\right|_{X_e} \tag{3.33b}$$

Note that when developing (3.11), the terms concerning the partial derivatives of $r(x)$ and $\hat{r}\,(x)$ are cancelled at EP because the value $I_L^* = P/V_g$ and $V_C^* - V_e = 0$. Hence, the small-signal dynamic is equal to is given by

$$\frac{d\tilde{v_C}}{dt} = -\frac{\frac{V_g}{L} - \frac{\beta PR}{V_g^2}}{\frac{RCV_e}{L} - \frac{P}{V_g}}\tilde{v_C} + \frac{\frac{R}{L}}{\frac{RCV_e}{L} - \frac{P}{V_g}}\tilde{p} = -\frac{B}{\Lambda}\tilde{v_C} + \frac{\Gamma}{\Lambda}\tilde{\hat{P}} \tag{3.34a}$$

$$\frac{d\tilde{p}}{dt} = -\beta\tilde{v_C} \tag{3.34b}$$

Therefore, the Jacobian matrix corresponding to (3.34) will be expressed as follows

$$A_{p2} = \begin{bmatrix} \left.\frac{\partial y_3}{\partial v_C}\right|_{X_e} & \left.\frac{\partial y_3}{\partial \hat{P}}\right|_{X_e} \\ \left.\frac{\partial y_4}{\partial v_C}\right|_{X_e} & \left.\frac{\partial y_4}{\partial \hat{P}}\right|_{X_e} \end{bmatrix} = \begin{bmatrix} -\frac{B}{\Lambda} & -\frac{\Gamma}{\Lambda} \\ \beta & 0 \end{bmatrix} \tag{3.35}$$

The characteristic equation corresponding to the previous Jacobian matrix is given by

$$|s\mathbb{I} - A_{p2}| = \begin{bmatrix} s + \frac{B}{\Lambda} & \frac{\Gamma}{\Lambda} \\ -\beta & s \end{bmatrix} = s^2 + \frac{B}{\Lambda}s + \frac{\Gamma\beta}{\Lambda} \tag{3.36}$$

From (3.36), the system will be stable if all coefficients of the characteristic equation are positive. By simple inspection, the following necessary conditions for stability are derived. For $\Lambda = 0$ the maximum output power load is defined

$$P < \frac{RCV_eV_g}{L} \triangleq P_{max} \tag{3.37}$$

And for $B > 0$, the maximum value of the parameter β is given by

$$\beta < \frac{V_g^3}{LPR} \triangleq \beta_{max} \tag{3.38}$$

It has to be pointed out that the maximum output power limit does not depend on the value of the linear estimator gain and its value is the same than that found in expressions (2.18) and (2.42). Furthermore, the maximum limit that the estimation loop gain can take is independent of the type of surface; this limit is only associated with the converter input and output voltages, the value of the input inductor and the incremental resistance at EP. Therefore, surfaces with the previous conditions equal, will result in the same limit value.

Finally, Table 3.2 presents a particularization of expression (3.22) with the linear estimator represented in (3.21) for all the basic polynomial surfaces studied so far.

Table 3.2: Particular cases of polynomial surfaces with power estimation loop.

Polynomial curves	**Coefficients in** (3.22)	**Surface**
Affine	$a_2 = b_2 = h = 0$	$S_{p1}(x) = a_1\left(i_L - \frac{\hat{P}}{V_g}\right) + b_1(v_C - V_e)$
Current parabola	$a_1 = b_2 = h = 0$	$S_{p3a}(x) = a_2\left(i_L^2 - \frac{\hat{P}^2}{V_g^2}\right) + 2b_1(v_C - V_e)$
Voltage parabola	$a_2 = b_1 = h = 0$	$S_{p3b}(x) = b_2\left(v_C^2 - V_e^2\right) + 2a_1\left(i_L - \frac{\hat{P}}{V_g}\right)$
Cross-power hyperbola	$a_2 = a_1 = 0$ $b_2 = b_1 = 0$	$S_{3c}(x) = i_L v_C - \frac{\hat{P}V_e}{V_g}$
Ellipse	$a_2 = b_2 = h = 0$	$S_{p3d}(x) = a_2\left(i_L^2 - \frac{\hat{P}^2}{V_g^2}\right) + b_2\left(v_C^2 - V_e^2\right)$

3.2.3 Implicit function

Section 2.5.2 has presented the extrapolation of results for polynomial surfaces to general implicit functions describing curves in the phase plane and their use as sliding surfaces. As an example, a curve with variable coefficients representing a parabola in the phase plane has been considered.

Using the similar procedure presented above, it is intended now to extend the use of the power estimator to implicit functions representing curves in the phase plane, and, for this purpose, the same parabola curve will be taken as example.

The results obtained are presented below.

Sliding surface:

$$\Sigma_{p4} = \{x|\ S_{p4}(x) = 0\} \tag{3.39a}$$

$$S_{p4}(x) = (v_C - MV_g) + \frac{(MV_g - V_e)\,{V_g}^2}{\hat{P}^2} i_L^2 \tag{3.39b}$$

Compact constant:

$$\mu = (MV_g - V_e)\,{V_g}^2 > 0 \tag{3.40}$$

Surface time-derivative:

$$\dot{S_{p4}}(x) = \frac{2\mu V_g i_L}{L\hat{P}^2} + \frac{2\mu\beta i_L^2\,(v_C - V_e)}{\hat{P}^3} - \frac{P}{Cv_C} - i_L(1-u)\left(\frac{2\mu v_c}{L\hat{P}^2} - \frac{1}{C}\right) \tag{3.41}$$

Reachability condition $S_{p4}(x)\,\dot{S}_{p4}(x) < 0$:

$$i_L < \frac{P}{v_C} + 1 - \frac{2\left(MV_g - V_e\right)V_g^2}{L\hat{P}^2} - \frac{2\beta\left(v_C - V_e\right)}{\hat{P}^3} \tag{3.42}$$

Equivalent control:

$$u_{4_{eq}} = 1 - \frac{\frac{2\mu V_g i_L}{L\hat{P}^2} + \frac{2\mu\beta i_L^2(v_C - V_e)}{\hat{P}^3} - \frac{P}{Cv_C}}{i_L\left(\frac{2\mu v_c}{L\hat{P}^2} - \frac{1}{C}\right)} \tag{3.43}$$

Ideal sliding dynamic:

$$i_L = \hat{P}\sqrt{\frac{v_C - MV_g}{\mu}} \tag{3.44a}$$

$$\frac{dv_C}{dt} = -\frac{\frac{2\mu}{L\hat{P}^2}V_g\left(i_L - \frac{P}{V_g}\right) + \frac{2\mu\beta i_L^2(v_C - V_e)}{\hat{P}^3}}{\frac{2\mu C v_c}{L\hat{P}^2} - 1} \tag{3.44b}$$

Partial derivatives and incremental resistance:

$$\left.\frac{\partial i_L}{\partial v_C}\right|_{X_e} = r\left(x\right)\Big|_{X_e} = -\left.\frac{\hat{P}^2}{2i_L\left(MV_g - V_e\right){V_g}^2}\right|_{X_e} = \frac{P}{2\left(MV_g - V_e\right)V_g} = -\frac{1}{R} \tag{3.45a}$$

$$\left.\frac{\partial i_L}{\partial \hat{P}}\right|_{X_e} = \frac{1}{V_g} \tag{3.45b}$$

Linearizing around its EP:

$$\frac{d\tilde{v_C}}{dt} = -\frac{\left(\frac{2\left(MV_g - V_e\right)V_g^3}{LRP^2} - \frac{2\left(MV_g - V_e\right)\beta}{P}\right)}{\frac{2\left(MV_g - V_e\right)V_g^2 CV_e}{LP} - 1}\tilde{v_C} + \frac{\frac{RV_g}{LP}}{\frac{2\left(MV_g - V_e\right)V_g^2 CV_e}{LP} - 1}\tilde{p} = -\frac{B}{\Lambda}\tilde{v_C} + \frac{\Gamma}{\Lambda}\tilde{\hat{P}} \tag{3.46a}$$

$$\left.\frac{\partial i_L}{\partial \hat{P}}\right|_{X_e} = \frac{1}{V_g} \tag{3.46b}$$

Characteristic equation of the system:

$$|s\mathbb{I} - A_{p4}| = \begin{bmatrix} s + \frac{B}{\Lambda} & \frac{\Gamma}{\Lambda} \\ -\beta & s \end{bmatrix} = s^2 + \frac{B}{\Lambda}s + \frac{\Gamma\beta}{\Lambda} \tag{3.47}$$

The system will be stable if all coefficients of the characteristic equation in (3.47) are positive.

For $\Lambda = 0$, the same expression for the maximum output power load for polynomial surfaces in (3.37) can be found here, where the incremental resistance at EP is equal to

$$R = \frac{2\left(MV_g - V_e\right)V_g}{P} \tag{3.48}$$

Finally, for $B > 0$, the maximum value for the estimation loop will be given by

$$\beta < \frac{V_g^3}{LRP} \triangleq \beta_{max} \tag{3.49}$$

Where the maximum limit above is similar to the one attained in (3.38). Based on the uniformity of the resulting stability conditions for all curves studied so far and presented in expressions (3.37) and (3.38), it can be expected that any curve in the phase plane $i_L - v_C$ that fulfills these conditions can be a candidate for sliding surface.

3.3 Characteristics of adaptive sliding controller with power estimation

3.3.1 Small-signal dynamics

All the surfaces discussed in this chapter, both polynomial surfaces and the implicit function based on a current parabola, can represent their behavior in sliding motion around EP according to the following linear second-order equation.

$$\frac{d^2\tilde{v_C}}{dt^2} + \frac{B}{\Lambda}\frac{d\tilde{v_C}}{dt} + \frac{\beta\Gamma}{\Lambda}\tilde{v_C} \tag{3.50}$$

The coefficients B and Γ have been defined in expressions (3.34) and (3.46) for polynomials and implicit function, respectively. Instead, the coefficient Λ is common to both.

It is worth noting that equation (3.50) just takes into account the ideal sliding dynamics. Regarding a external variation on power and control references, Fig. 3.5 shows the block diagram of the linearized system in sliding motion when disturbances on the output power ΔP and change of voltage reference ΔV_e are considered. Due to the adaptive reference current, the input voltage disturbances are instantaneously rejected.

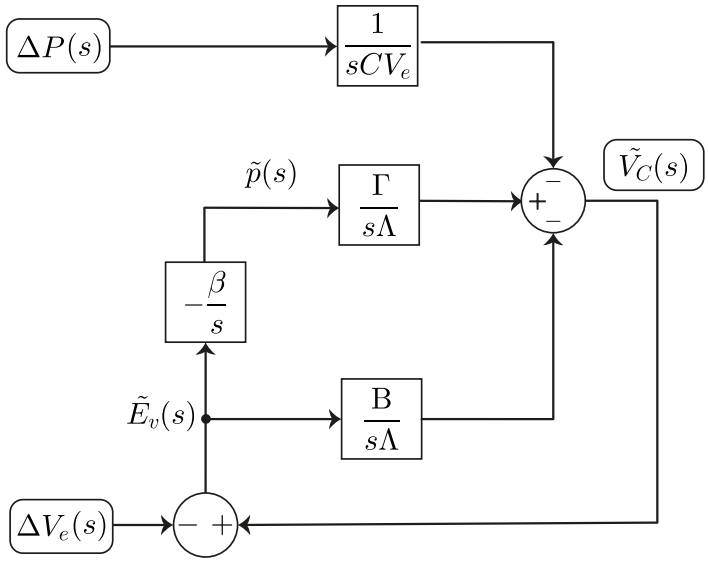

Fig. 3.5: Block diagram of a boost converter in sliding motion including output power and voltage reference perturbations.

By examining the coefficients of the characteristic equation for both polynomial and implicit functions, it can be concluded that the incremental resistance $r(x)\Big|_{X_e} = R$ mainly determines the sliding dynamics, which is a result consistent with the conclusions attained in chapter 2.

In the polynomial cases, where the coefficients in the sliding surface are constant, the same values of R and power estimator will yield the same dynamic behavior. Fig. 3.6 and Fig. 3.7 present the response of the system under variations of the power load from 1 kW to 900 W and the voltage reference from 380 V to 390 V using the parameter values of Table 3.1. They also compare comparising the response of the model depicted in Fig. 3.5 with a PSIM© simulation for polynomial surfaces with $R = -15\Omega$ and a estimator gain $\beta = 10$ kA/s. In both responses, the analytical description is in perfect agreement with the numerical.

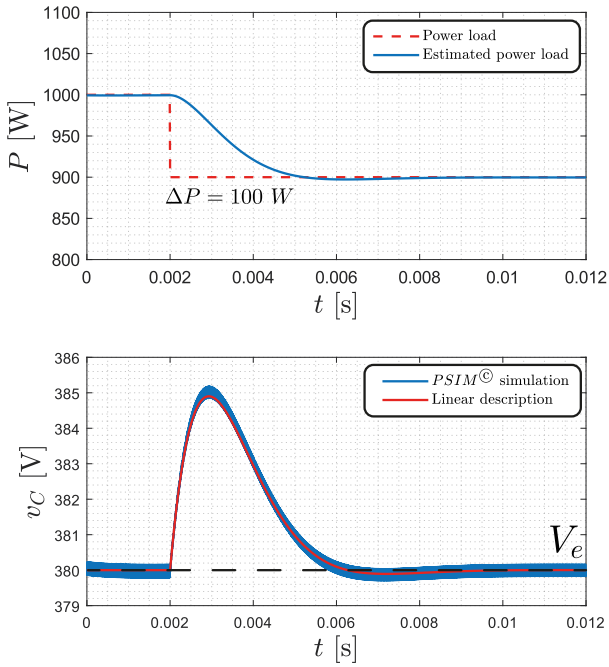

Fig. 3.6: Comparison of analytical and simulated responses of power estimation and output voltage regulation after an abrupt change of the output power load for $S_{p2}(x)$ with $R = -15\Omega$ and $\beta = 10$ kA/s.

After validation of the analytical model near the EP, different values of power estimation gain β with a fixed value of R are tested under abrupt changes of power load as illustrated in Fig. 3.8. A high gain value generates a better rejection of disturbances due to an underdamped behavior in power estimation. Nevertheless, there is no a large difference in settling time within the range of β values because a combined effect between the sliding surface and the estimator.

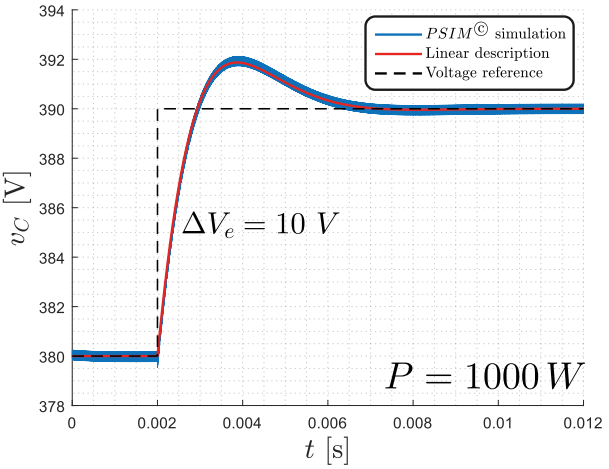

Fig. 3.7: Comparison of analytical and simulated responses of output voltage to a change of voltage reference for $S_{p2}(x)$ with $R = -15\Omega$ and $\beta = 10$ kA/s.

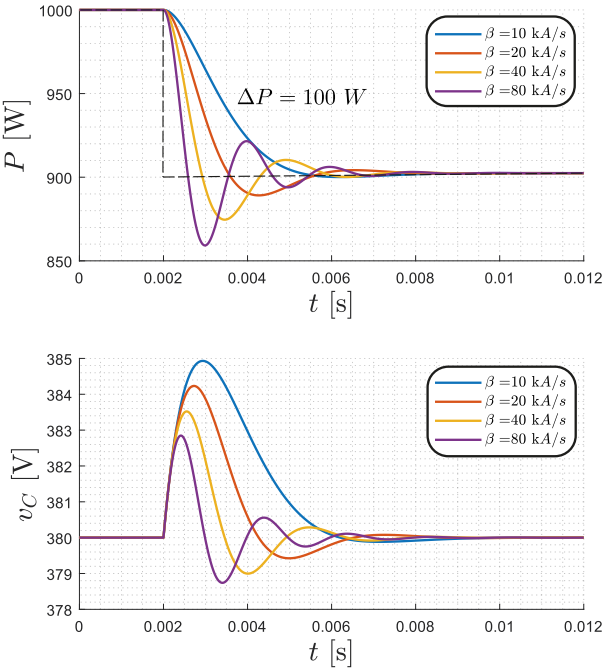

Fig. 3.8: Comparison of a general polynomial surface of second degree under change of 100 W power load for several values of gain of the power estimator and a $R = -15\Omega$.

Fig. 3.9 and Fig. 3.10 show the result of variations of output power load and voltage reference for the implicit function $S_{p4}(x)$ under the identical pattern of changes made to the polynomial ones. In contrast to the previous performance,

the analytical description differs from PSIM© simulations, especially in the change of voltage reference.

This is a consequence of how the coefficients on the surface $S_{p4}(x)$ have been calculated based on adaptive current reference. The value of $r(x)$ depends strongly on the power estimation variable $\hat{P}$ and V_e as it can determined in (3.45a). In addition, a variation of EP just does not change the value of $r(x)$, but it changes the shape of the curve. This is explained in more detail in the next section.

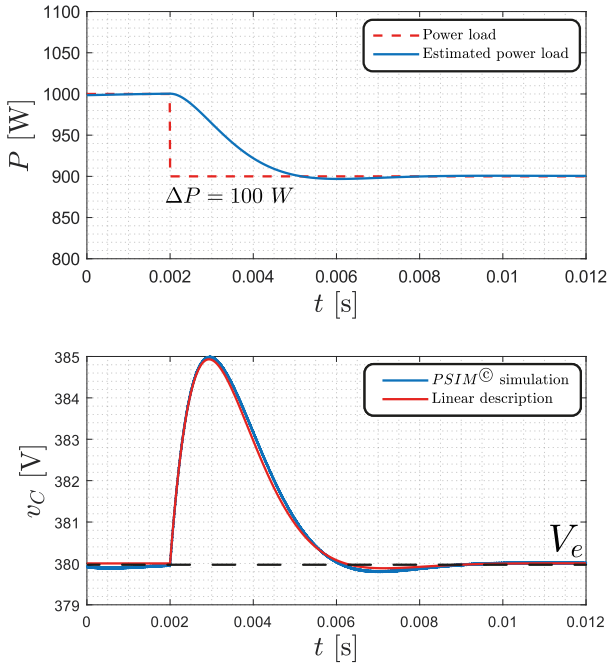

Fig. 3.9: Comparison of analytical and simulated responses of power estimation and output voltage regulation after an abrupt change of the output power load for $S_{p4}(x)$ with $R = -15\Omega$ and $\beta = 10$ kA/s.

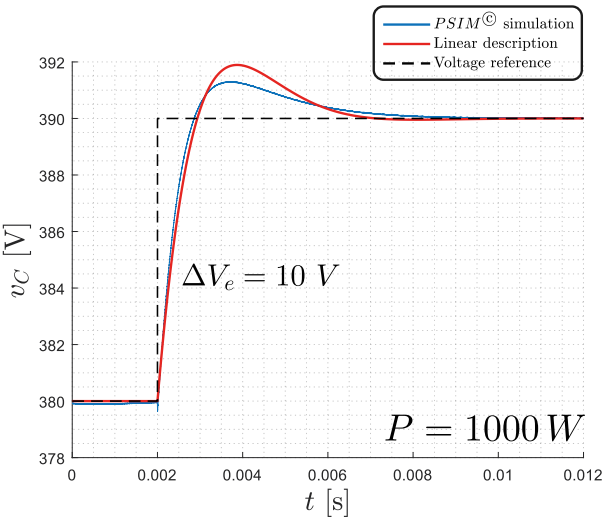

Fig. 3.10: Comparison of analytical and simulated responses of output voltage to a change of voltage reference for $S_{p4}(x)$ with $R = -15\Omega$ and $\beta = 10$ kA/s.

3.3.2 Large-signal analysis

The analysis and results of the linearized model of the system show certain key aspects of sliding mode control with power estimation that can provide a qualitative description in a large-signal analysis. The main one is that the sliding dynamics can be described in terms of its incremental resistance $\partial v_C/\partial i_L$.

However, other aspects are not clear. For instance, the stability conditions imposed on the maximum value of the output power load and the estimation loop gain are very relaxed and have higher values than the ones used in Table 3.1 , so they do not provide a solid benchmark to understand the system behavior. For example, with $R = -15\Omega$, P=1 kW and $\beta = 10$ kA/s, the value of these limits are $P_{max} = 41.5$ kW and $\beta_{max} = 969.7$ kA/s. To put the problem in context, Fig. 11 shows the scale of the chosen parameter values in a red circle and the calculated limit for a range of each parameter, the blue shaded region corresponding to the allowed values for stability.

In order to examine the large-signal dynamics, a complementary approach is to study the evolution of the system during a start-up with zero initial conditions up to the equilibrium point, using numerical simulations in PSIM©and MATLAB.

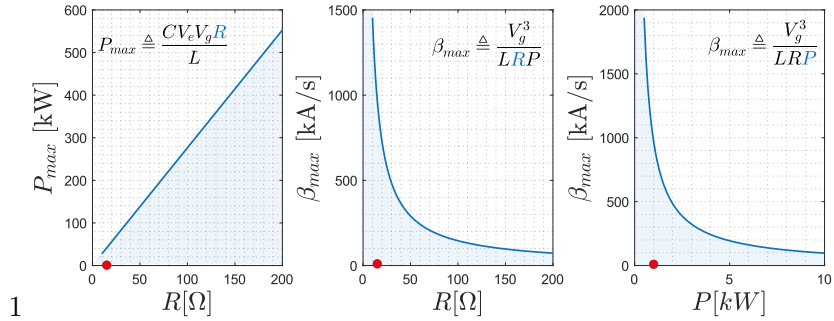

Fig. 3.11: Region of stability conditions for feasible values for incremental resistance R, output power load P, and gain estimation β.

Fig. 3.12 illustrates the start-up from initial conditions $x_o = [0,\ V_g,\ 0]^\intercal$ for polynomials surfaces $S_{p1}(x)$, $S_{p3a}(x)$, $S_{p3b}(x)$ y $S_{p3d}(x)$ with $R = -15\Omega$ and $\beta = 10$ kA/s. S_{p3c} has a value of R that is only determined for by the converter parameters , so it cannot be used for control purposes. The converter parameters and the coefficients of surfaces are shown in Table 3.1 and Table 3.3, respectively.

Table 3.3: Surface coefficients used in Fig. 3.12.

Surface	$\mathbf{a_2}$	$\mathbf{b_2}$	**h**	$\mathbf{a_1}$	$\mathbf{b_1}$
$S_1(x)$	0	0	0	4	0.1
$S_{3a}(x)$	1	0	0	0	0.1812
$S_{3b}(x)$	0	0.001	0	11.5	0
$S_{3e}(x)$	3.2	0.002	0	0	0

For the type of polynomial curves considered, the surface maintains its geometrical shape in the phase plane $i_L - v_C$. The effect of power estimation loop on the computing of the current reference can be visualized as a translation of the curve through the phase plane on the $v_C = V_e$ axis in the intersection of the sliding surface with this axis. This aspect has already been presented in section 3.3.1 for integral SMC and illustrated in Fig. 3.4.

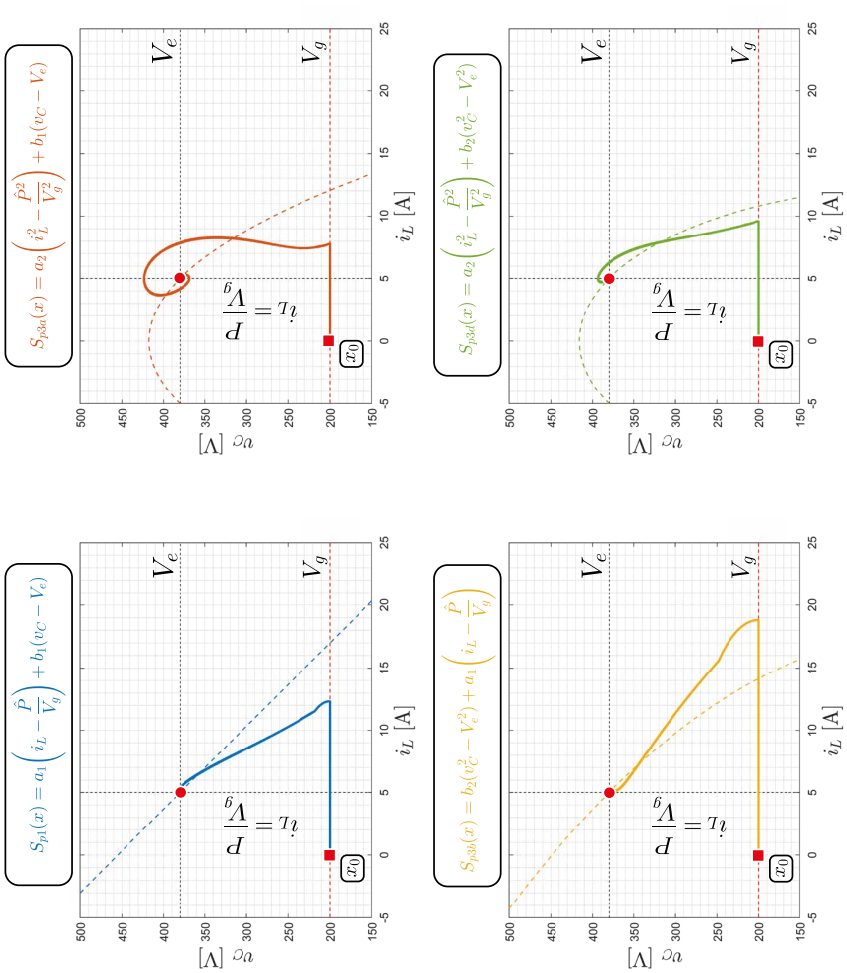

Fig. 3.12: Start-up from zero initial conditions to EP of four polynomial surfaces.

In Fig 3.12, the surface is shown in dotted line after the trajectory reaches the desired EP. However, the translation of the curve during the transient may allow the system to reach the surface at another point in the plane different from the expected one without power estimation as seen in the figure. Except in the case of $S_{p3b}(x)$, the system reaches the surface earlier decreasing the inrush current.

As the power estimation loop is associated to the current reference, in the surfaces where algebraic powers and the corresponding coefficients are more predominant (as S_{p3a} and S_{p3d}), the behavior of the system in closed-loop is more oscillatory given the interaction between the control and the estimation loop, but the surface is reached in less time. On the other hand, a higher dominance of voltage terms in the surface results in damped behavior, but at the expense of a higher inrush current. This can be seen clearly in Fig. 13, where the power estimation is also presented and its transient behavior corresponds to the output voltage transient as it could be expected.

It is remarkable that the performance of both $S_{p1}(x)$ and $S_{3d}(x)$ is the most well-balanced: a short settling time with adequate voltage overshoot and inrush current. This seems to imply a sort of proportionality between voltage and current terms of the same order in polynomial sliding surfaces to achieve optimal performance. The current reference is controlled by the voltage error through the power estimation loop, which in turn reduces the voltage difference until the EP is reached.

Complementarily, Fig. 3.14 illustrates the incremental resistance along trajectory for each polynomial surface, which is calculated by means of (3.25) and (3.26) because in sliding motion, $\widehat{r\,(x)} = r(x)$.

Another way to understand the nonlinear sliding dynamics in (3.36) through its linear approximation is to interpret the trajectory from x_0 to EP as a transition between a set of neighboring linear systems or a time-varying linear function, where the absolute value of the incremental resistance R and the estimated power load $\hat{P}$ are key elements. The latter can be particularly relevant since the stability conditions were defined in steady state, where $\hat{P} = P$. However, during the transient state, the limit is established by the estimated power value. Thus, underdamped dynamics in start-up or change of EP can generate unstable behavior in the vicinity of the boundary illustrated in Fig. 3.11.

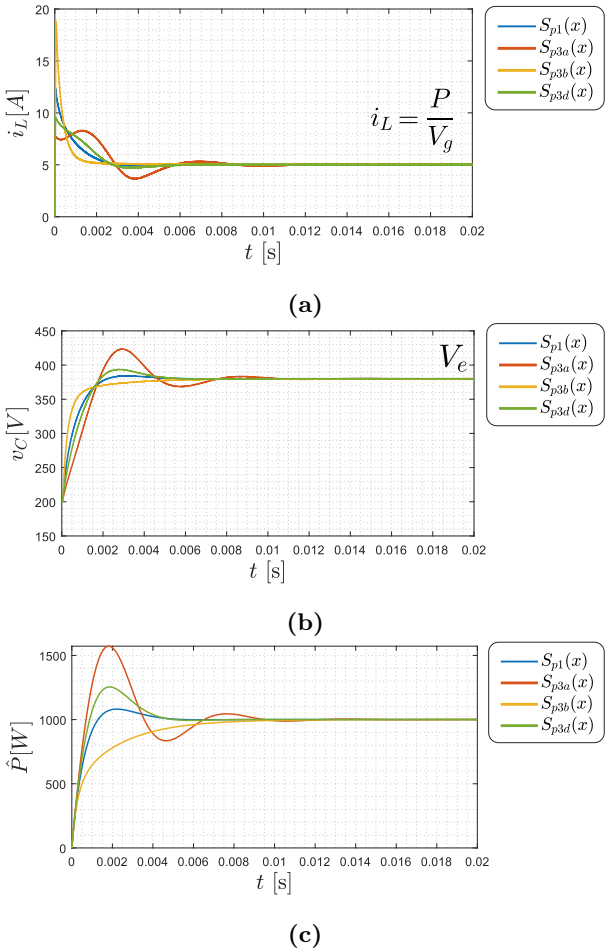

Fig. 3.13: PSIM© simulation of state variables during start-up for polynomial surfaces. (a) i_L, (b) v_C and (c) $\hat{P}$

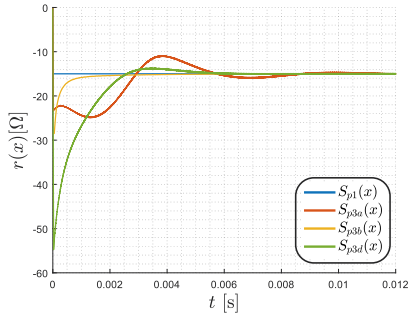

Fig. 3.14: Incremental resistance along the trajectory for polynomial surfaces.

This approach results in the set of pole diagrams of the characteristic equation for the boost converter with CPL operating with SMC shown in Fig. 3.15.

The three pole diagrams consider the variation of the linearized dynamics in sliding mode within a range for the incremental resistance, the gain of the estimation loop and its estimated power, respectively. In each diagram, a single variable is changed according to a given step value, while the other two are fixed. Moreover, the area where a damping constant is equal or less than 0.4 is highlighted.

In the above scenarios, the increase in power generates a damped response with a shorter settling time. For β, the increase in the gain loop value is proportional to the system speed as would be expected. In contrast, a larger value of the loop gain does not substantially affect the speed of the response beyond a value of 5 kA/s but affects the damping making the response more underdamped; By looking at Fig. 3.15a, it can be observed that the loop gain should have a value of less than 30 kA/s.

There are three differentiated zones for the incremental resistance From the minimum allowed value up to about 12 Ω, the behavior is damped. Between 12 and 25 Ω, the system shows the best performance. Beyond that value, the system is oscillatory and the settling time increases. Taking this analysis into account, the affine surface with power estimation $S_{p1}(x)$ would be the best choice for polynomial surface considering its expected value of R.

The parabolic curve $S_{p4}(x)$ taken as an example of a general implicit function also fulfills the characteristics described in the previous analysis for polynomial curves. Fig. 3.16 shows three trajectories of $S_{p4}(x)$ for three values of M illustrated in Table 3.4. Unlike the polynomial cases, the variable coefficient on the surface changes the shape of the curve during the trajectory, widening or contracting the parabola about the $i_L = 0$ axis from the estimated value of the power. As a product of this time-varying modification, the system goes into sliding motion practically from the initial instant t_o.

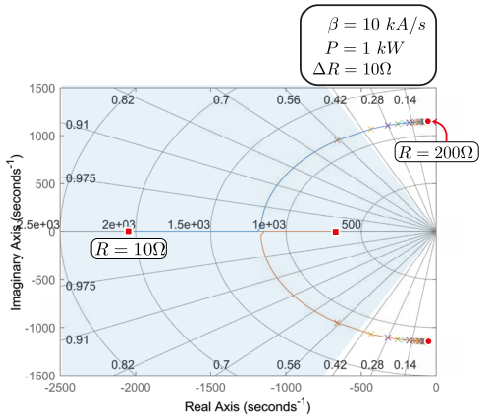

(a)

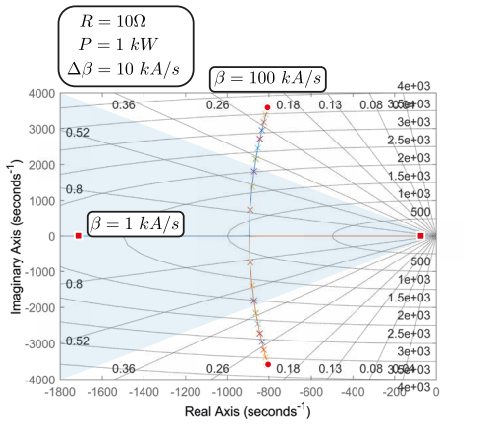

(b)

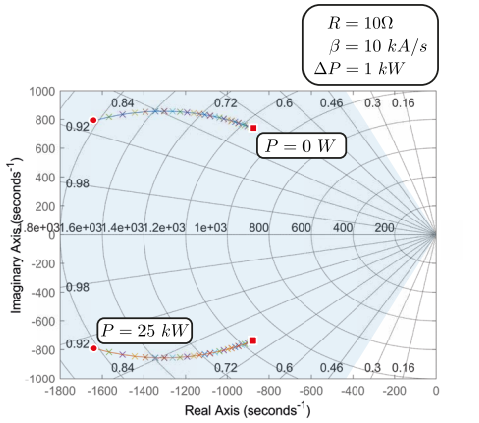

(c)

Fig. 3.15: Pole diagrams for boost converter with CPL and polynomial surface. (a) Incremental resistance, R, (b) Estimation loop gain β and (c) Estimated power load $\hat{P}$.

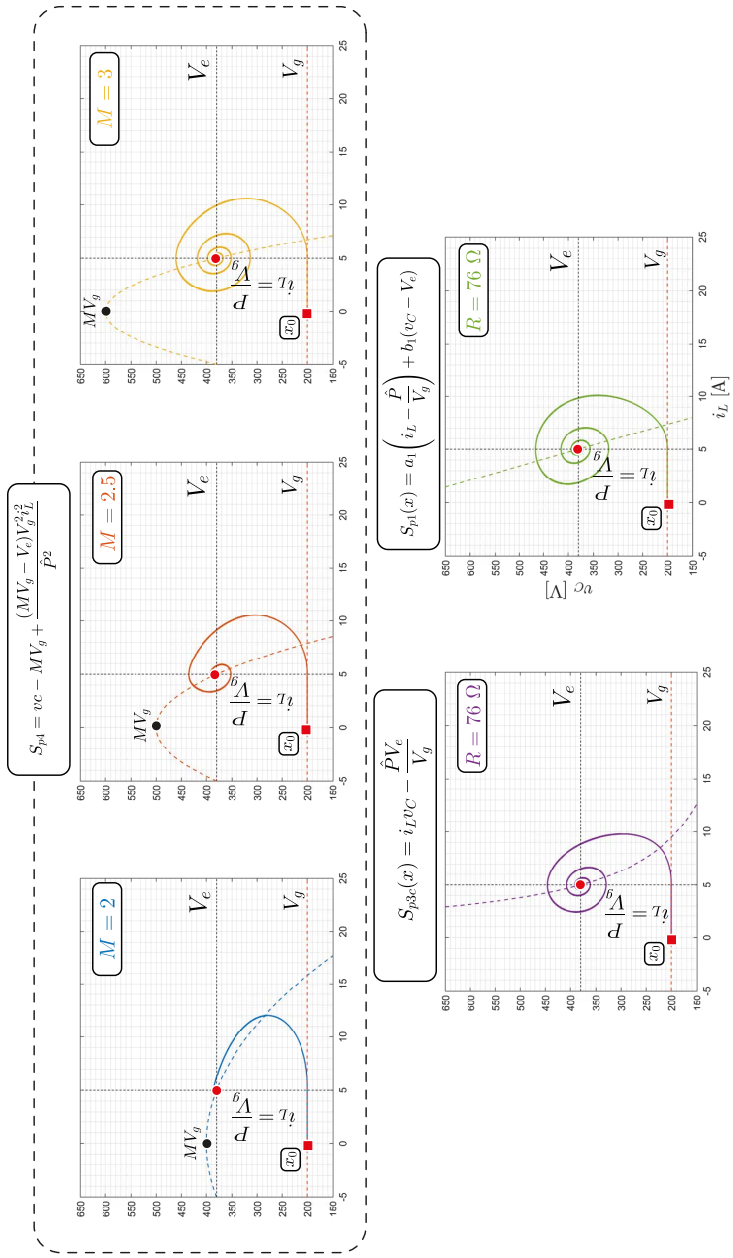

Fig. 3.16: Start-up from zero initial condition to EP of three parabolic surfaces and two polynomial surfaces with higher value of R.

Table 3.4: Surface parameters and their respective absolute incremental resistance value at EP.

M	R
2	8 ΩH
2.5	48 ΩH
3	88 ΩH

The same figure shows two polynomial curves for comparison, $S_{p3c}(x)$ and $S_{p1}(x)$. Both show a resistance in EP equal to 76 Ω, the inherent one for $S_{p3c}(x)$ according to parameters' values of Table 3.1. By simple inspection, the best performance is achieved for the surface with the minimum value of $R = 8\ \Omega$ for $S_{p4}(x)$. Higher values of R produces an underdamped behavior, regardless of the type of curve. This assessment validates the previous conclusions: the appropriate value for incremental resistance produces a good performance when it is lower than 30 Ω as illustrated in Fig. 3.17.

Another feature of the parabolic curve $S_{p4}(x)$ is the inrush current, which is smoother and longer lasting in contrast to those achieved in the polynomial curves with the same value of $r(x)\Big|_{X_e} = R$.

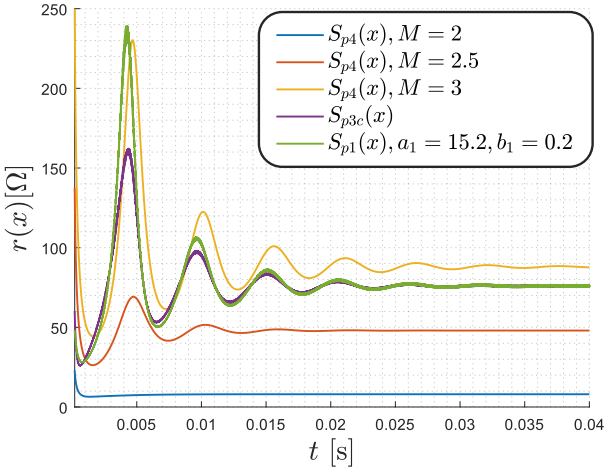

Fig. 3.17: Incremental resistance along the trajectory for surfaces in Fig. 3.16.

3.3.3 Effect of power estimation on the region for sliding motion

In the previous section, observing the trajectories from zero initial conditions to the EP, it appeared how the system reached the sliding surface earlier in almost all cases with respect to the instantaneous power measurement studied in chapter 2. By comparing the ESM without power estimation expressed in (2.54) with (3.28), the estimation loop aggregates a term that extends the sliding dynamics region because of the estimation. Fig. (3.18) gives an example of how the ESM region is expanded in proportion to the value of the gain estimation loop taking the surface $S_{p1}(x)$, although this spread of the region is not significant with respect to the original value. It is the combination of the translation with the extension, i.e. both of them being products of the estimated power, that allows the system to intersect the surface in a shorter time.

This result is common for both polynomial surfaces. For implicit function in (3.42), the expansion of ESM region is negligible due to the time-varying form of the surface during the transient.

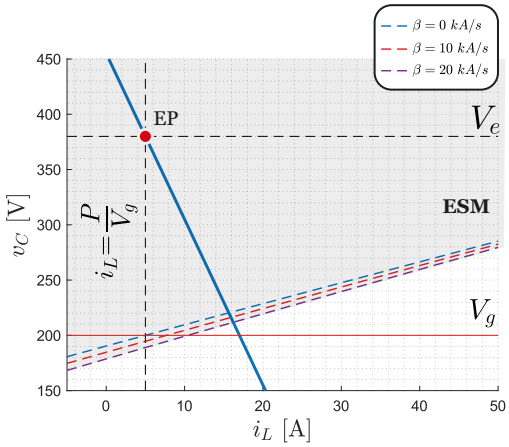

Fig. 3.18: ESM region of sliding surface $S_{p1}(x)$ for three values of β.

3.3.4 Effect of conduction losses at EP

In section 3.2.2.1, it has been explained how the action of the power estimation loop calculates the total power supplied by the input source to the converter, i.e., the power of the load plus the power losses generated in the converter itself.

The estimation error at EP is defined as $E_p = \hat{P} - P$ that, in the presence of losses, it will not be zero and will be equal to

$$E_P = \frac{V_g}{2R_L}\left(V_g - \sqrt{V_g^2 - 4PR_L}\right) - P \tag{3.51}$$

Where R_L represent the total parasitic resistance in the converter and is the main source of losses. The expression (3.51) is the result of power balance in the converter and is therefore independent of the control method. Thus, the error of power estimation is a function of parasitic resistance and output power load. Fig. 3.19 plots the percentage error for an increasingly wide range of resistance and load power. In practice with a highly efficient converter, it is common to find R_L values of less than 1 Ω, resulting in an error of less than 2%. In the case of a 1 kW load, this would represent a maximum offset of 40 W (96% of efficiency).

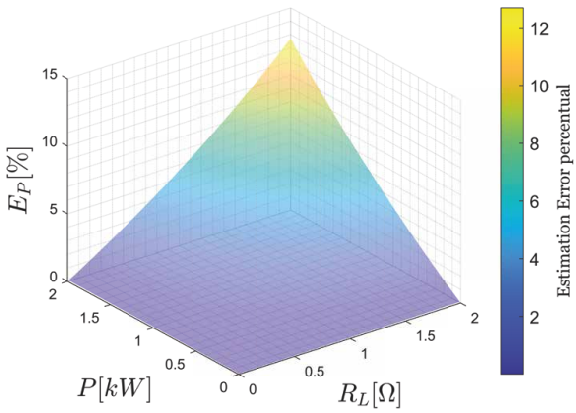

Fig. 3.19: Power estimation error E_P for a range of output power load P and parasitic resistance R_L.

In order to reduce E_P to zero, the input voltage V_g can change in the surfaces to an apparent input voltage $\widehat{V_g}$ that includes the power losses as follows

$$\widehat{V_g} = \frac{V_g + \sqrt{V_g^2 - 4\hat{P}R_L}}{2} \tag{3.52}$$

Where $\widehat{V_g} < V_g$.

3.4 Candidate functions for power estimation

The linear power estimator proposed in the previous sections gives a guidance procedure for defining a general set of power estimators $\hat{P}$ within sliding surfaces computed from the voltage error $e_v = v_C - V_e$ as follows

$$\frac{d\hat{P}}{dt} = f(e_v) \tag{3.53}$$

Where $f(e_v)$ is a function of the voltage error. By examination of linear estimator, any candidate function f must satisfy the following three conditions:

(i) It must be a function with odd symmetry, i.e., $f(-e_v) = -f(e_v)$,

(ii) $f(0) = 0$ will be the only zero crossing point, at least within the operating range (stable point), and

(iii) the tangent line to f at the origin must have negative slope (linearized around at EP), i.e.,

$$\left.\frac{\partial f(e_v)}{\partial e_v}\right|_{e_v=0} = -F < 0 \tag{3.54}$$

Where $F > 0$ is a real number.

These conditions are similar to those applied in classical control loops based on the integral of the error function. The linear estimator is the simplest one of these types. Other alternatives have appeared using this methodology. In [59] a nonlinear voltage error function has been used for power estimation but applied

to a PWM nonlinear control. However, that work is a singular contribution and there is no selection of the estimator based on a systematic approach.

In the next pages, three main types of candidate functions that satisfy the requirements based on voltage error will be presented.

3.4.1 Rational functions

Expression (3.55) illustrates a general rational function for power estimation loop. To achieve the specified requirements, the degree of the numerator must be odd and that of the denominator even.

$$f_1(e_v) = -\frac{\beta e_v^{2m-1}}{1+\alpha e_v^{2n}} \tag{3.55}$$

The coefficient m and n are integer. Thus, the linear estimator is an especial case of (3.55) when $m = 1$ and $\alpha = 0$, and the nonlinear estimator presented in [59] corresponds to $m = 1$ and $n = 1$. The partial derivative of f respect to e_v are given by

$$\frac{\partial f_1(e_v)}{\partial e_v} = -\frac{\beta}{1+\alpha e_v^{2n}}\left((2m-1)\, e_v^{2(m-1)} - 2n\alpha e_v^{2(n+m-1)}\right) \tag{3.56}$$

By inspection at $e_v = 0$, it can be concluded that the only appropriate value for m is 1 to guarantee that $\frac{\partial f_1(e_v)}{\partial e_v}$ is $-\beta$. For any other value the function exhibits odd symmetry and at $e_v = 0$ its partial derivative is zero. On the other hand, there is no constraint on the parameter n, so $n \in \mathbb{Z}$ with a correct selection of parameter α.

An advantage of the rational function when $n \neq 0$ and the degree of the numerator is lower than that of the denominator is the possibility to constraint the maximum estimated power value; otherwise, the estimator will be unbounded. Then there exists a $\|f_1\|_\infty = P_{max}$, which takes place at points $e_v = \pm e_{vo}$ with a value equal to

$$e_{vo} = \sqrt[2n]{\frac{2m-1}{2n\alpha}} \tag{3.57}$$

By introducing (3.57) in (3.55), we obtain

$$\left| f\left(e_{vo}\right) \right| = \left| \frac{\beta \left(\frac{2m-1}{2n\alpha}\right)^{\frac{2m-1}{2n}}}{1+\frac{2m-1}{2n}} \right| \tag{3.58}$$

Fig. 3.20 compares five of the first rational functions in terms of exponents and estimator parameters listed in Table 3.5 for the surface $S_{p1}(x)$ and the parameters in Table 3.1.

Table 3.5: Rational functions and their parameters.

Rational function	β	α
$f_{1a} = -\beta e_v$	-10 kA/s	0
$f_{1b} = \frac{\beta e_V}{1+\alpha e_v^2}$	-10 kA/s	100 n
$f_{1c} = -\frac{\beta e_V^3}{1+\alpha e_v^2}$	-25 A/s	2.5 m
$f_{1d} = -\frac{\beta e_V}{1+\alpha e_v^2}$	-10 kA/s	20 n
$f_{1e} = -\frac{\beta e_v^3}{1+\alpha e_v^4}$	-20 kA/s	20 m

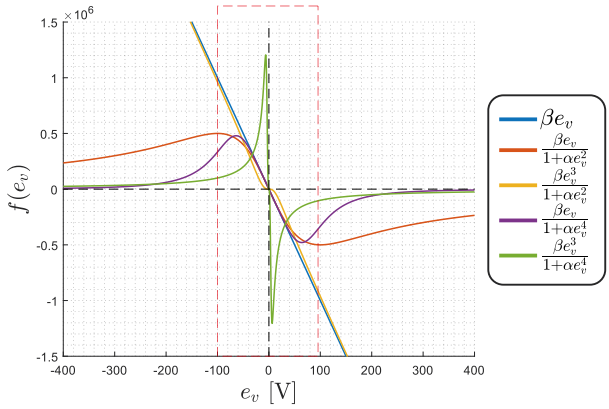

(a)

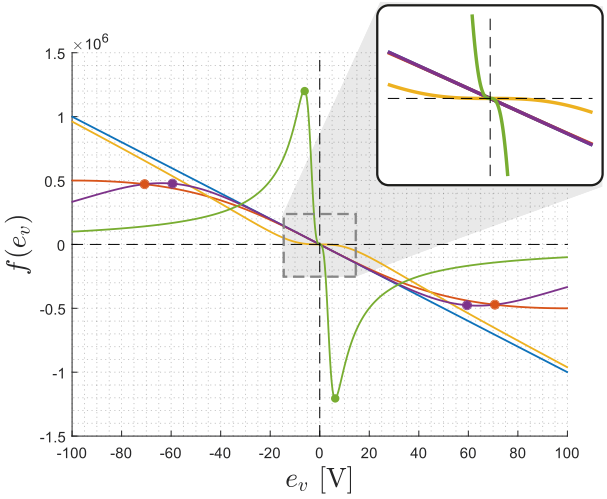

(b)

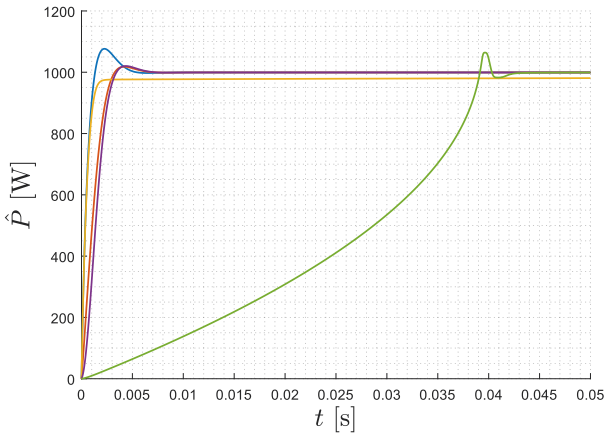

(c)

Fig. 3.20: Rational functions: (a) panoramic view, (b) zoom at origin of the plane, (c) Output power estimation.

Fig. 3.20a shows a panoramic representation of the functions, differentiating two unbounded, f_{1a} and f_{1c}, and three bounded functions. f_{1b}, f_{1d} and f_{1d}. The latter ones tend asymptotically to zero when the voltage error is very large, avoiding a saturation of the integrator and overshoot, at expense of a longer settling time. Furthermore, Fig. 3.20b is a zoom in the zero-voltage error vicinity, visualizing the maximum points of the bounded functions. It is clear that at the origin, functions with an exponent m greater than one have a flat plateau. As mentioned before, the function tends to EP, but this plateau produces an error in the power estimation in steady state, the value being larger the value of m is smaller as can be seen in Fig 3.20c for f_{1c} and f_{1e}. Functions with a higher degree of denominator tend to concentrate around $e_v = 0$ axis and $f = 0$ in the rest of the response, thus resulting in an excessively large settling time.

3.4.2 Trigonometric functions

There are two functions that use trigonometric expressions and satisfy the conditions: sine and tangent with the following equations.

$$f_{2a}\left(e_v\right) = -\beta \sin\left(\alpha e_v\right) \tag{3.59a}$$

$$f_{2b}\left(e_v\right) = -\beta \tan\left(\alpha e_v\right) \tag{3.59b}$$

Both functions are limited to the range $-\pi/2 < e_v < \pi/2$. So, if the operating range of the converter is $|e_v| = 200\ V$, the parameter's values are fixed to $\alpha = 0.008\ rad/V$ and $\beta = 1$ MA/s with $\left.\frac{\partial f_1(e_v)}{\partial e_v}\right|_{e_v=0} = -\beta$. Out of this operating range, the estimator reaches another equilibrium point and will have a non-zero estimation error.

Fig. 3.21 illustrates the trigonometric function for power estimation loop for an operating range of $\pm 200V$. The tangent estimator has overshoot during the transient state from null initial conditions; close to the limit of the range, the tangent tends to infinite; see Fig. 3.21b.

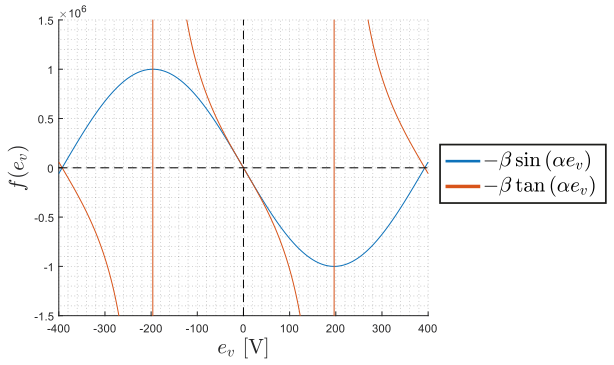

(a)

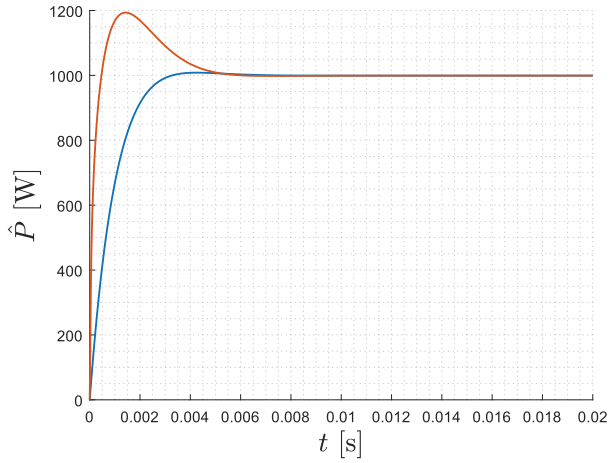

(b)

Fig. 3.21: Trigonometric functions: (a) panoramic view and (b) Output power estimation.

3.4.3 Sigmoid functions

Sigmoids are curves that present a monotonic S-shape characteristic. Conditions (iii) restrict sigmoid functions to be monotonic decreasing.

There are several equations that represent sigmoid curves. Table 3.6 lists four of the most commonly used sigmoid functions, their partial derivatives and slope at $e_v = 0$.

In Fig. 3.22a one of the most characteristic features of sigmoid functions can be seen: moving away from the origin the function is bounded and constant, and is parallel to the horizontal axis up to $\pm\infty$. The parameters in Table 3.6 have been chosen so that all the functions had their linear range close to the

Table 3.6: Sigmoid function equation and their parameters.

Sigmoid function	**Partial derivative**	**Slope at EP**	β	α
Logistic function $f_{3a} = -\beta\left(1 - \frac{2}{1+e^{-\alpha e_v}}\right)$	$-\beta\left(\frac{2\alpha e^{-\alpha e_v}}{1+e^{-\alpha e_v}}\right)$	$-2\beta\alpha$	1 MA/s	0.04
$f_{3b} = -\frac{2\beta}{3}\arctan(\alpha e_v)$	$-\frac{2\beta}{3}\frac{\alpha}{1+\alpha^2 e_v^2}$	$-\frac{2\beta\alpha}{3}$	1 MA/s	0.05
$f_{3c} = -\beta\tanh(\alpha e_v)$	$-\beta\alpha\,\mathrm{sech}(\alpha e_v)$	$-\beta\alpha$	1 MA/s	0.025
$f_{3d} = -\frac{\beta e_v}{\sqrt{1+\alpha e_v^2}}$	$-\frac{\beta}{\left(1+\alpha e_v^2\right)^{3/2}}$	$-\beta$	15 kA/s	0.002

origin of the same width and the lower and upper bounds equal. Although the functions do not present significant differences, their corresponding behavior in the estimator loop provides different performances at start-up due to the specific morphology in each case and their slope around the origin as can be seen in Figure 3.22b. The best performance is obtained for rational function f_{3d}, which also allows an easy tuning of both slope and width because of the independence of its parameters.

3.4.4 First-order sliding estimator

A special case results when considering the sign function according to (3.60) as a candidate function for a power estimator. Strictly speaking, the sing function would only fulfill two of the three conditions, because its derivative at the origin does not exist. However, similar to the unbounded rational functions with $m > 1$, the estimator with f_4 will tend to EP, but without remaining there (because any disturbance would move it away) confined in a permanent sliding around it.

$$f_{4a}(e_v) = -\beta\ sign(e_v) = \begin{cases} e_v < 0 & \beta \\ e_v = 0 & 0 \\ e_v > 0 & -\beta \end{cases} \tag{3.60}$$

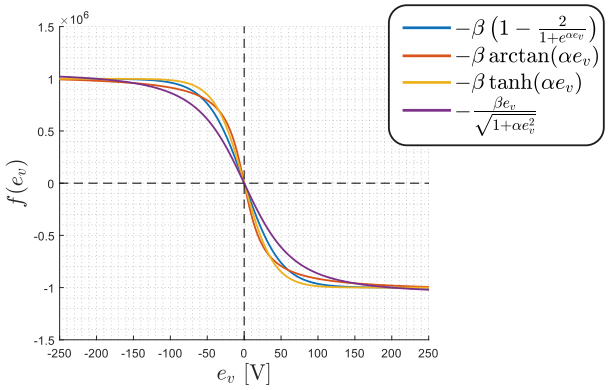

(a)

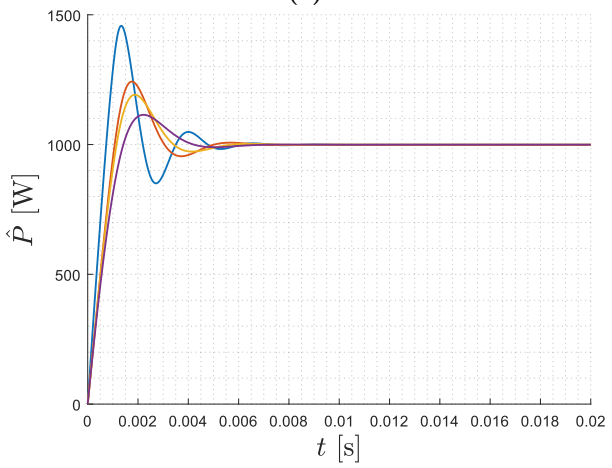

(b)

Fig. 3.22: Sigmoid functions: (a) panoramic view and (b) Output power estimation.

This fact can be understood as part of an ideal sliding estimator, where its average value would correspond to the value of the load power. The ideal sliding estimator means infinite frequency, this being impractical for implementation as seen in Chapter 2. A bounded approximation referred in [20] and described in (3.61), produces a finite frequency and also fulfills (iii) condition.

$$f_{4b}(e_v) = f(x) = \begin{cases} \beta\ sign(e_v) & |e_v| \geq \varepsilon \\ -\beta\ e_v & |e_v| < \varepsilon \end{cases} \tag{3.61}$$

The parameter ε is the bandwidth of the approximation and determines the chattering frequency of power estimation. On the other hand, parameter β must be greater than P to reach the sliding surface $e_v = 0$.

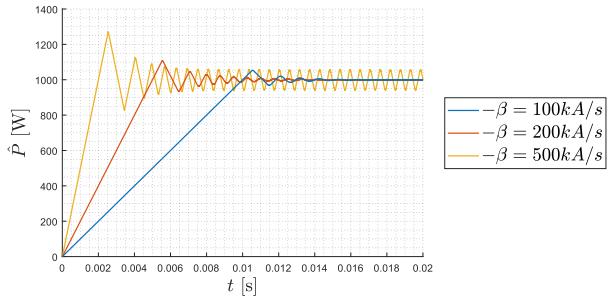

Fig. 3.23: Output power estimation for first-order sliding estimator.

Fig. 3.23 illustrates the sliding estimator behavior for three values of β. In all cases, the average value of estimated power reaches the real power: the larger the value of β, the faster the estimated value is reached. However, a high value of gain estimation loop leads to a high value of chattering. In contrast to the approach proposed for the power converter in this work where the chattering is a natural phenomenon on switching converters, chattering in the continuous power estimation loop is undesirable. For these scenarios, an appropriate gain β will be chosen in order to reduce or reject the chattering.

In general, this section provides evidence of the feasibility of a sliding power estimator within an SMC. Other higher order sliding estimators can be proposed to reduce or reject the chattering and obtain better performance. In these cases, they would no longer represent simple voltage error functions, but more complex estimation loops and are beyond the scope of this chapter.

3.5 Conclusions

The use of an integral loop of the voltage error added to the polynomial sliding surfaces has demonstrated the feasible and efficient estimation of the power losses of the boost converter with CPL guaranteeing at the same time zero steady-state voltage error. An analysis of this result has led to a procedure for establishing a loop estimation of the total power flowing through the input port of the converter that, in the absence of losses, is equal to the power load due to

the POPI nature of power converter.

For both the general polynomial surface formulation and the time-varying current parabola studied, the inclusion of the power estimation loop based on an integral of voltage error, i.e. a linear power estimator, satisfies the existing condition for sliding motion and stability criteria under the appropriate selection of surface coefficients, following the principles described in Chapter 2.

The dynamics of the system in sliding motion has been well-defined in small signal from the features of the incremental resistance $r(x)\Big|_{X_e} = -R$ and the gain of the power estimator β, obtaining the best performances for R with absolute values lower than 30 Ω and β between 5 kA/s and 30 kA/s. These conclusions could also be extrapolated for the large-signal qualitative description after analyzing the closed-loop control for start-up from zero initial conditions. In general, the power estimation loop allows reaching the surface in a shorter time compared to the same test without estimation in most cases with lower peak inrush current. For polynomial surfaces, better performance has been observed when the powers of i_L and v_C terms are equal, i.e., $S_{p1}(x)$, $S_{p3d}(x)$.

Regarding the addition of power losses, the power estimation error is unique for all surfaces and remains below 2% when normal operating values are considered. However, if the value of the parasitic resistance in the converter is known, an apparent input voltage $\widehat{V_g}$ can be calculated to achieve zero estimation error.

Numerical analysis, PSIM© simulations have verified the theoretical predictions. A final global assessment that considers dynamic performance as well as implementation allows concluding that the best surface among polynomial and implicit function as alternative for the sliding surface is the linear surface $S_{p1}(x)$. This is the same choice than in chapter 2.

Finally, a general procedure has been derived to find other candidate voltage error functions from the analysis and results obtained for the linear estimator. Four types of candidate functions have been proposed: rational functions of the type found in [59], trigonometric functions, sigmoid functions and first-order sliding estimators. Operating conditions have been established for each type of function with well-defined estimation limits.

A preliminary analysis of a first-order power sliding estimator has shown its feasibility, so further research would contemplate the developing of higher-order sliding estimators.

Part II

Power source elements

UNIVERSITAT ROVIRA I VIRGILI
A SLIDING MODE APPROACH TO CONTROL POWER SINKS AND POWER SOURCES IN DC-DC SWITCHING CONVERTERS
David Alejandro Zambrano Prada

Chapter 4

Power source based on loss-free resistor terminated at a generic nonlinear static load

Introduction

The first part of this thesis has discussed the CPL as a challenge for dc-dc switching converters because the constant power demand at the output of converters operating in CCM and open loop generates instability, making the CPL the worst-case load in terms of control.

The sliding mode control strategies proposed for the boost converter with CPL, either through instantaneous measurement or estimation of the output power, have been proved to be effective and robust by extending their application to other types of static loads. The surfaces used in the SMC are based on implicit functions $S(x) = 0$ in the phase plane $i_L - v_C$, where the proposed generalized approach (polynomial surfaces) searches a zero error of the inductor current and capacitor voltage with respect to their references at EP.

Another approach to the constant power demand in a dc-dc switching converter has been already mentioned in chapter 1. It is intuitive to think that the most direct way to supply constant power to a load is through a power source. By considering the converter as a two-port circuit, there are three canonical elements for power processing: the dc transformer, the power gyrator, and the loss-free resistor.

Of the above three, LFRs present a virtual resistor in the input port and a power source supplying the load in the output port. In addition, LFR behavior results from the use of SMC, which imposes proportionality between input voltage and current in steady-state and CCM in switching power converters with a series inductor in the input port [13].

Power factor correction (PFC) and impedance matching in PV systems are currently the main applications of the LFRs synthetized by an appropriate control. In the first case, PFC is the result of SMC either in a semi-bridgeless rectifier [60] or in a boost converter [61], while it stems from a current control with adaptive features in reference [62]. LFR behavior in a power converter for impedance matching is the result of the inner loop control in a two-loop strategy for maximum power point tracking in a PV system as described in [63]. In addition, SMC-based LFRs have been used to adapt a sea wave energy harvesting transducer to a battery supplying a standalone payload [64].

In all the previous examples, the main objective is obtaining a virtual resistance characteristic at the input port of the converter by means of an appropriate control. On the other hand, it has to be pointed out that all implemented LFRs reported in the literature terminate at a resistor, and it has not been proved that they can exhibit the same performance if other type of loads substitutes the resistor. This would be the case of CCL or CPL presented in microgrids or new ones due the emergence of electric vehicles with lithium batteries that can be effectively modelled as a voltage source in series with a resistor.

Note that an LFR-based converter transferring power to any type of load would regulate the power indirectly in a relatively simple way by means of the emulated resistor at the input port. In a clear-cut contrast, a direct regulation in any converter would require processing the product of current and voltage of the output port and result in a more complex system for both analysis and implementation.

For all the previous reasons, it makes sense to explore the SMC-based LFR design in an appropriate converter loaded by the parallel connection of a CPL, a CCL, and a battery with internal resistance. The resulting combination will present a current versus voltage nonlinear static characteristic, i.e., it will constitute a generic nonlinear static load (GNSL). It can be expected that the particularization of GNSL in the case of CPL, CCL, a single resistor, or a battery as well as in the combination of pairs of loads or groups of three loads

can give sufficient insight for the design of power systems feeding loads from a constant power source.

4.1 SMC-based LFR in a boost converter with GNSL

Fig. 4.1 shows a boost converter loaded by a GNSL, which is the parallel connection of a CPL, a CCL, and a battery with internal resistance. The small letters in the figure represent instantaneous values of the converter variables.

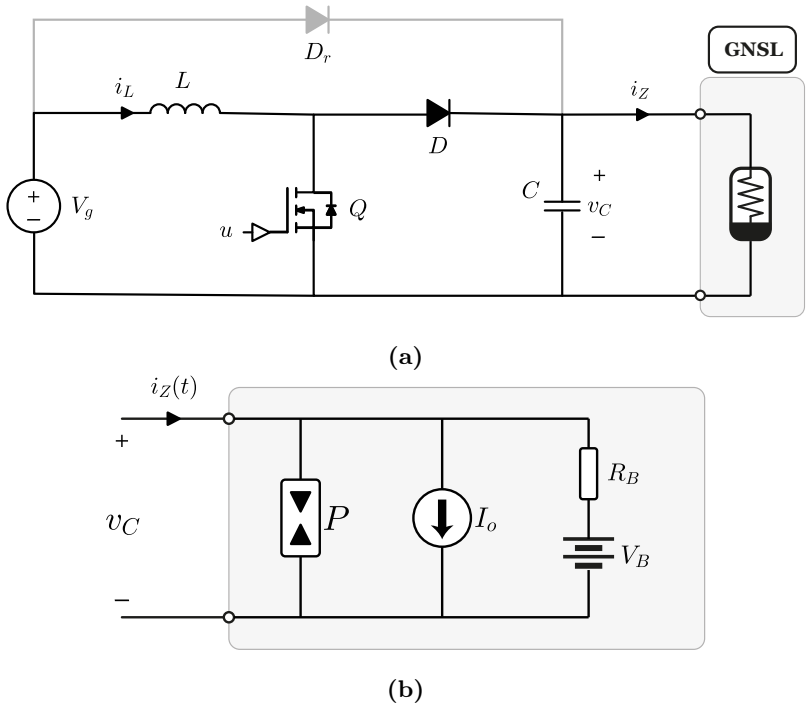

Fig. 4.1: (a) Boost converter loaded with a GNSL and (b) Model of a GNSL.

The objective of SMC is obtaining a two-port circuit whose steady-state equations are the following:

$$V_1 = rI_1 \tag{4.1a}$$

$$V_1 I_1 = V_2 I_2 \tag{4.1b}$$

Equations (4.1) and (4.1b) characterize an LFR, so, in steady-state, Fig. 4.1 can be described as illustrated in Fig. 4.2 (Input port: $V_1 = V_g$ and $I_1 = I_L$, output port: $V_2 = V_C$ and $I_2 = I_Z$). Letter r represents the virtual resistance of the LFR ideally transferring the 100% of the absorbed power P from the input port to the output port. Capital letters stand for steady-state values of the converter variables.

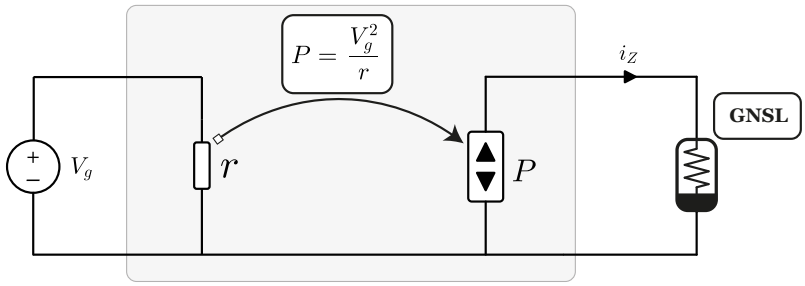

Fig. 4.2: Equivalent circuit of an LFR loaded with a GNSL.

In CCM, the converter in Fig. 4.1 can be described as follows

$$L\frac{di_L}{dt} = V_g - v_C\,(1-u) \tag{4.2a}$$

$$C\frac{dv_C}{dt} = i_L\,(1-u) - i_z \tag{4.2b}$$

The current i_z is given by

$$i_z = \frac{P}{v_C} + I_o + \frac{v_C}{R_B} - \frac{V_B}{R_B} \tag{4.3}$$

To fulfil (4.1a), $S_5\,(x)$ is selected as follows

$$S_5\,(x) = ri_L - V_g \tag{4.4}$$

which implies

$$S_5(x)\,\dot{S}_5(x) = r\,(ri_L - V_g)\,\frac{V_g - v_C\,(1-u)}{L} \tag{4.5}$$

where

$$\dot{S}_5(x) \triangleq \frac{dS_5(x)}{dt} \tag{4.6}$$

Given that $V_g - v_C < 0$, it can be deduced that $S_5(x) > 0$ and $u = 0$ will result in $S_5(x)\,\dot{S}_5(x) < 0$. Similar result is obtained for $S_5(x) < 0$ and $u = 1$. Therefore, sliding motions will exist in the boost converter of Fig. 4.1 with the selected sliding surface and the associated switching law described above [13].

4.2 Equilibrium point analysis

4.2.1 Steady-state

The invariance condition $\dot{S}_5(x) = 0$ results in the equivalent control $u_{eq} = 1 - V_g/v_C$. Introducing the constraint $S_5(x) = 0$ in (5), and substituting u by u_{eq} in the same equations lead to the following ideal sliding dynamics

$$\frac{dv_C}{dt} = \frac{V_g^2}{Crv_C} - \frac{i_Z}{C} \tag{4.7a}$$

$$i_L = \frac{V_g}{r} \tag{4.7b}$$

In equilibrium, $v_C = V_C^*$, $i_Z = I_Z^*$, and $\frac{dv_C}{dt} = 0$, which implies $V_g^2/r = V_C^* I_Z^*$, or equivalently dc input power equal to dc output power in steady-state. However, I_Z^* is a nonlinear function of V_C^*, and therefore the equation describing the possible values of V_C^* is given by

$$\frac{V_g^2}{r} = P + V_C^* I_o + \frac{V_C^{*2}}{R_B} - \frac{V_C^* V_B}{R_B} \tag{4.8}$$

Assuming $V_g^2/r > P$, only one equilibrium point X_e will exist and the value of V_C^* will be given by

$$V_C^*\Big|_{X_e} = \frac{V_B - I_0 R_B + \sqrt{(I_0 R_B - V_B)^2 + 4R_B\left(\frac{V_g^2}{r} - P\right)}}{2} \tag{4.9}$$

which corresponds to the horizontal coordinate of the intersection point of the i-v curve of the power source in Fig. 4.3 given by $I_Z^* = V_g^2/V_C^* r$ and the curve $I_Z^* = P/V_C^* + I_o + V_C^*/R_B - V_B/R_B$ corresponding to the GNSL in a MATLAB simulation for the set of parameter values $V_g = 240\ V$, $r = 48\ \Omega$, $P = 400\ W$, $I_o = 1\ A$, $R_B = 100\ \Omega$ and $V_B = 300\ V$.

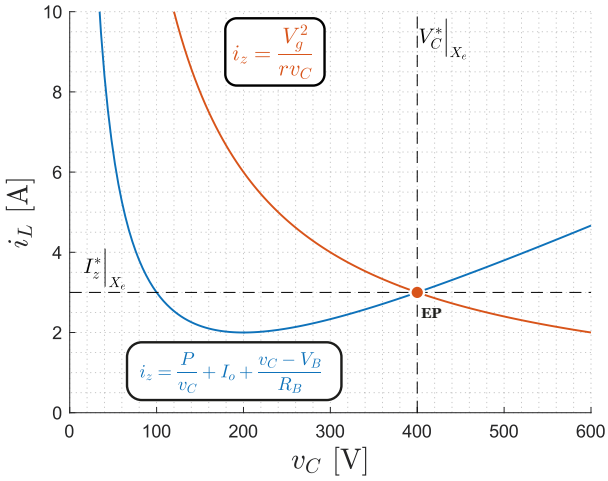

Fig. 4.3: Equilibrium point of the output port of the LFR loaded with a GNSL.

Figs. 4.4a-4.4c show respectively the values of the equilibrium point when the GNSL becomes a resistive load ($P = 0$, $I_o = 0$ and $V_B = 0$), a CCL ($P = 0$ and $R = \infty$) or a voltage source ($P = 0$, $R = 0$ and $I_o = 0$). The CPL case, i.e. $R = \infty$ and $I_o = 0$ results in an infinite number of equilibrium points because the load and the power source are characterized by the same curve as illustrated in Fig. 4.5a.

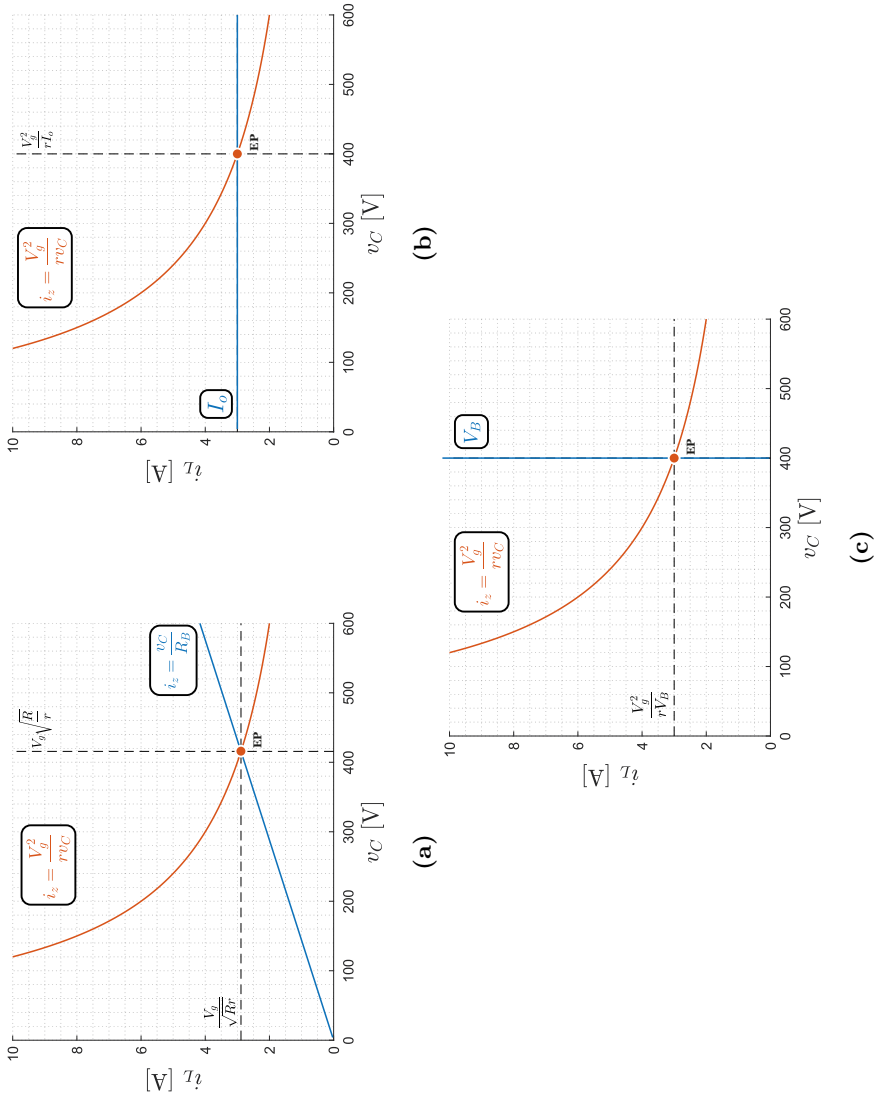

Fig. 4.4: Equilibrium point for: (a) resistive load; (b) CCL; and (c) voltage source load.

This case corresponds to the connection of a power source in parallel with a power sink (CPL), which is only consistent when both devices handle the same amount of power P (Fig.4.5b).

All the six possible combinations of pairs of canonical loads yield attainable equilibrium points as listed in Table 4.1, where the value of V_C^* in the equilibrium point is given in each case.

Similarly, the four possible combinations of three loads lead to a single equilibrium point as illustrated in Table 4.2. Recall that expressions in Table 4.1 and Table 4.2 are obtained by particularizing expression (4.9) for each type of load combinations.

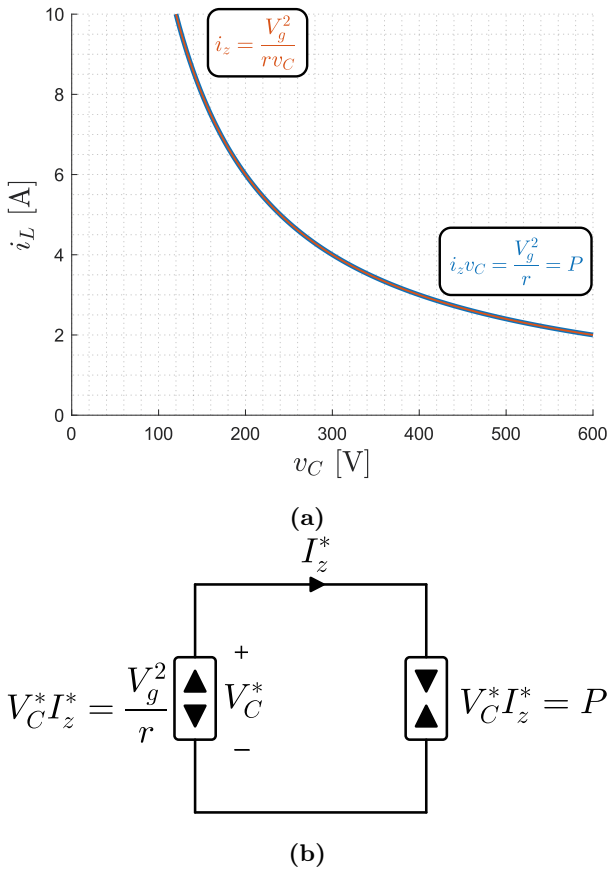

Fig. 4.5: Infinite number of equilibrium points for: (a) CPL; and (b) circuit interpretation.

Table 4.1: Output voltage at equilibrium point for pairs of loads.

GNSL	$\mathbf{V_C^*}$
CPL-R $(I_o = 0,\ V_B = 0)$	$\sqrt{R\left(\frac{V_g^2}{r} - P\right)}$
CPL-CCL $(R_B \to \infty)$	$\frac{1}{I_O}\left(\frac{V_g^2}{r} - P\right)$
CPL-Voltage source $(I_o = 0,\ R_B = 0)$	V_B
CCL-R $(P = 0,\ V_B = 0)$	$\frac{1}{2}\left(-I_O R + \sqrt{I_O^2 R^2 + 4R\frac{V_g}{r}}\right)$
Voltage source with R $(I_o = 0,\ P = 0)$	$\frac{1}{2}\left(V_B + \sqrt{V_B^2 + 4R\frac{V_g^2}{r}}\right)$
CCL-Voltage source $(P = 0,\ R_B = 0)$	V_B

Table 4.2: Output voltage at equilibrium point for combinations of three loads.

GNSL	$\mathbf{V_C^*}$
CPL-Voltage source with R ($I_O = 0$)	$\frac{1}{2}\left(V_B + \sqrt{V_g^2 + 4R\left(\frac{V_g^2}{r} - P\right)}\right)$
CPL-R-CCL ($V_B = 0$)	$\frac{1}{2}\left(-I_O R + \sqrt{I_O^2 R^2 + 4R\left(\frac{V_g^2}{r} - P\right)}\right)$
CPL-CCL-Voltage source ($R = 0$)	V_B
CCL-Voltage source with R ($P = 0$)	$\frac{1}{2}\left(V_B - I_O R + \sqrt{(I_O R - V_B)^2 + 4R\frac{V_g^2}{r}}\right)$

4.2.2 Stability conditions

The ideal sliding dynamic behavior is described by the nonlinear differential equation (8), which can be rewritten as follows

$$C\frac{dv_C}{dt} = \frac{V_g^2}{rv_C} - i_Z \triangleq\ g\left(x\right) \tag{4.10}$$

The linearized system around the equilibrium point X_e will be given by

$$C\frac{d\tilde{v_C}}{dt} = \alpha\tilde{v_C} \tag{4.11}$$

where

$$\alpha = \left.\frac{\partial g(x)}{\partial v_C}\right|_{X_e} = -\frac{V_g^2}{rV_C^{*2}} - \left.\frac{\partial i_Z}{\partial v_C}\right|_{X_e} \tag{4.12}$$

On the other hand, by taking (4.3) and applying (4.12), we get

$$\alpha = -\frac{V_g^2}{rV_C^{*2}} + \frac{P}{V_C^{*2}} - \frac{1}{R} \tag{4.13}$$

Note that the system terminated with a GNSL will be always stable because the input power is always larger than the power absorbed by the CPL, namely,

$$\frac{V_g^2}{rV_C^{*2}} > \frac{P}{V_C^{*2}} \tag{4.14}$$

Which implies $\alpha < 0$.

It immediately follows from (4.13) and (4.14) that all the particular cases of GNSL considered in the previous section will be stable with the exception of the single CPL case. In this case, the system is marginally stable because α in (4.13) is zero since the left term of (4.14) equals the right term in equilibrium. This result coincides with the theoretical prediction given in chapter 2 when a general polynomial sliding surface of first degree takes the particular expression given by (4.4).

Note that the active damping introduced by the virtual resistance r of the LFR ensures the stability. This fact is particularly remarkable in the case of a single CCL of current I_0, in which a classical approach based on the converter dynamic model predicts the presence of imaginary poles in the control to output transfer function $G_C(s)$ due to the absence of resistive elements in the power stage. In that case $G_C(s)$ will be given by

$$G_c(s) = \frac{V_g}{(1-D)^2}\left(1 - \frac{sLI_0}{V_g(1-D)}\right)\frac{1}{1+\frac{s^2LC}{(1-D)^2}} \tag{4.15}$$

where D is the steady-state duty cycle, and the necessary damping should be introduced by appropriate current feedback [28].

4.3 Simulation and experimental results

4.3.1 Experimental setup

To validate the proposed study, several simulations have been carried out in PSIM software and a prototype of the boost converter has been built in our laboratory. The prototype utilizes $C = 20$ μF (MKP1848SE62050JP4C), $L = 550$ μH, one power MOSFET (STW25NM60ND) and one dual fast-recovery diode (STPSC20H12CWL). One leg is the diode of the converter, and the other one is used to give initial voltage $v_C(0) = V_g$ to guarantee the existence of sliding mode conditions at the start-up and therefore mitigate the inrush current [65]. The control circuit makes use of Hall-effect sensors measuring input voltage (LEM – LV25P) and inductor current (LEM – LA25NP) and analogue electronics for mathematical operations (AD633, LM324). Gate signal is applied using an opto-isolated driver (TLP350H) fed by a dedicated isolated source (TRACO TEN 3-2415N). Switching at a finite frequency in the system is induced by means of a hysteresis comparator implemented with analogue electronics (LM319, CD4027). The schematic diagram of the power stage of the converter prototype is illustrated in Fig. 4.6 while the controller circuitry is depicted in Fig. 4.6. From left to right, it is possible to observe the conditioning circuits for voltage and current measurements, mathematical operations to define the sliding surface, the circuit creating the limits of the hysteresis band and the hysteresis comparator based on the SR flip-flop.

The experimental set-up consists of an oscilloscope (Tektronix MDO3024) with one isolated current probe (U3401A) and two differential voltage probes (Yokogawa 700924), one power source feeding the power converter (ELEKTRO-AUTOMATIK EA PSI-9750-40), two power sources feeding the control circuits (TERMA 72-10505) and three programmable electronic loads (EA ELR-9750-44, EA EL-3400-25 and EA EL9750-75 HP). Fig. 4.8 is a picture of the experimental setup where the converter prototype, GNSL, oscilloscope, input voltage source and control supply can be identified.

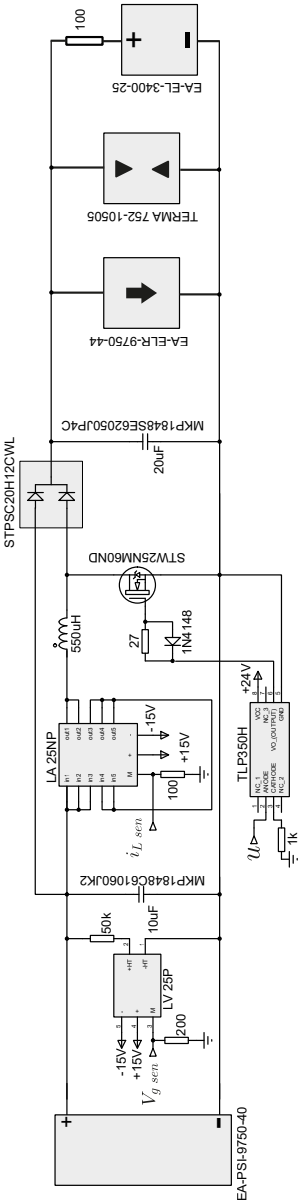

Fig. 4.6: Schematic diagram of the implemented boost converter circuit.

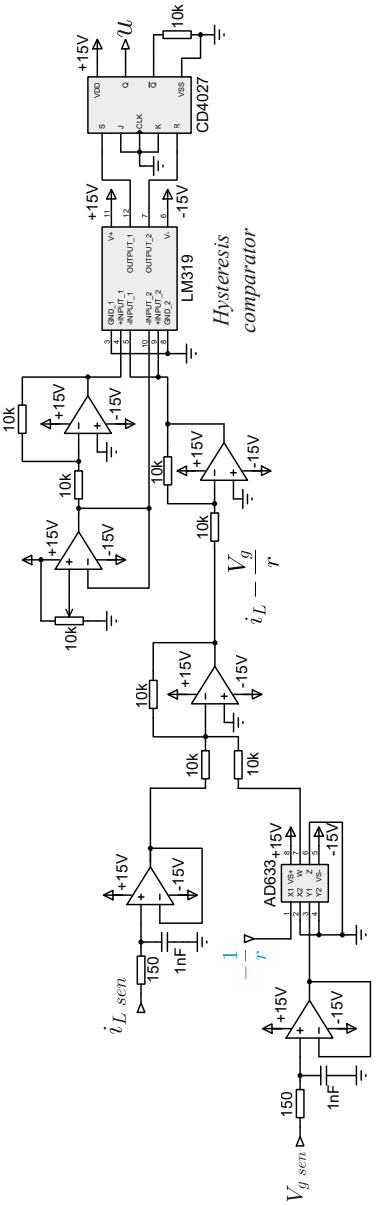

Fig. 4.7: Schematic diagram of the implemented controller circuit.

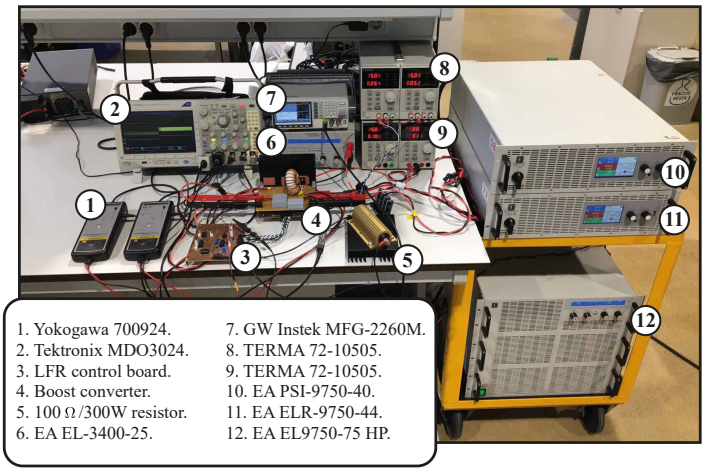

Fig. 4.8: Photography of the experimental setup and converter prototype.

4.3.2 Static and dynamic performance

Fig. 4.9 shows the simulated waveforms and the corresponding experimental results for the set of parameter values $V_g = 240\ V, r = 52\ \Omega, P = 350\ W, I_o = 0.92\ A$, $R = 100\ \Omega\ V_B = 287\ V$. Figs. 9a and 9b depict the simulation and the measured results respectively of the inductor current and capacitor voltage waveforms in steady-state when the GNSL is composed of all studied elements. It can be observed that the average value of the simulated output voltage is the predicted value in expression (4.9).

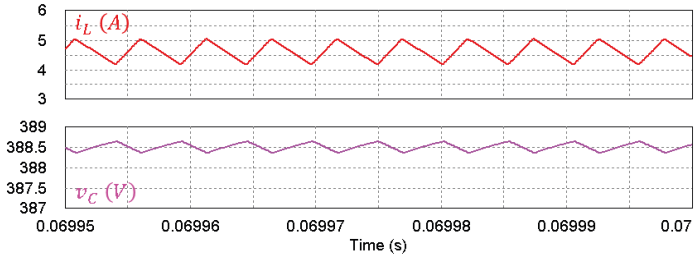

(a)

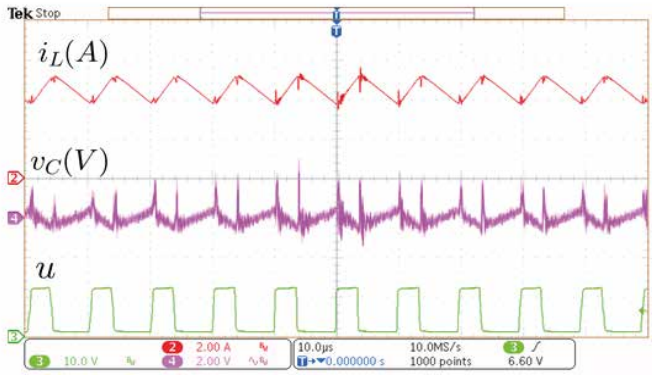

(b)

Fig. 4.9: Waveforms for GNSL with all the elements: (a) PSIM simulation; and (b) measured inductor current (dc+ac) and measured voltage (ac).

Fig. 4.10 illustrates the simulation results for the stable transition from a first equilibrium point to a new one corresponding to a change in the virtual resistance of the LFR for different combination of loads in the GNSL (CCL, battery type, battery type and CPL, CCL and CPL, battery type and CCL, and battery type and CCL and CPL). As it can be observed, all the steady-states evaluated are stable and the transitions show the expected first-order dynamic behavior with a settling time given by $-4/\alpha$ as theoretically predicted by equation (4.11).

Fig. 4.11 shows the experimental results for the same combination of loads in the GNSL used for simulations. A good agreement is observed between the steady-state values in simulations and measured waveforms. The time constant of the transitions is higher in experiments because the input capacitances of the electronic loads emulating the GNSL behavior are connected in parallel with the output capacitance of the boost converter, but they have not been considered in the simulations.

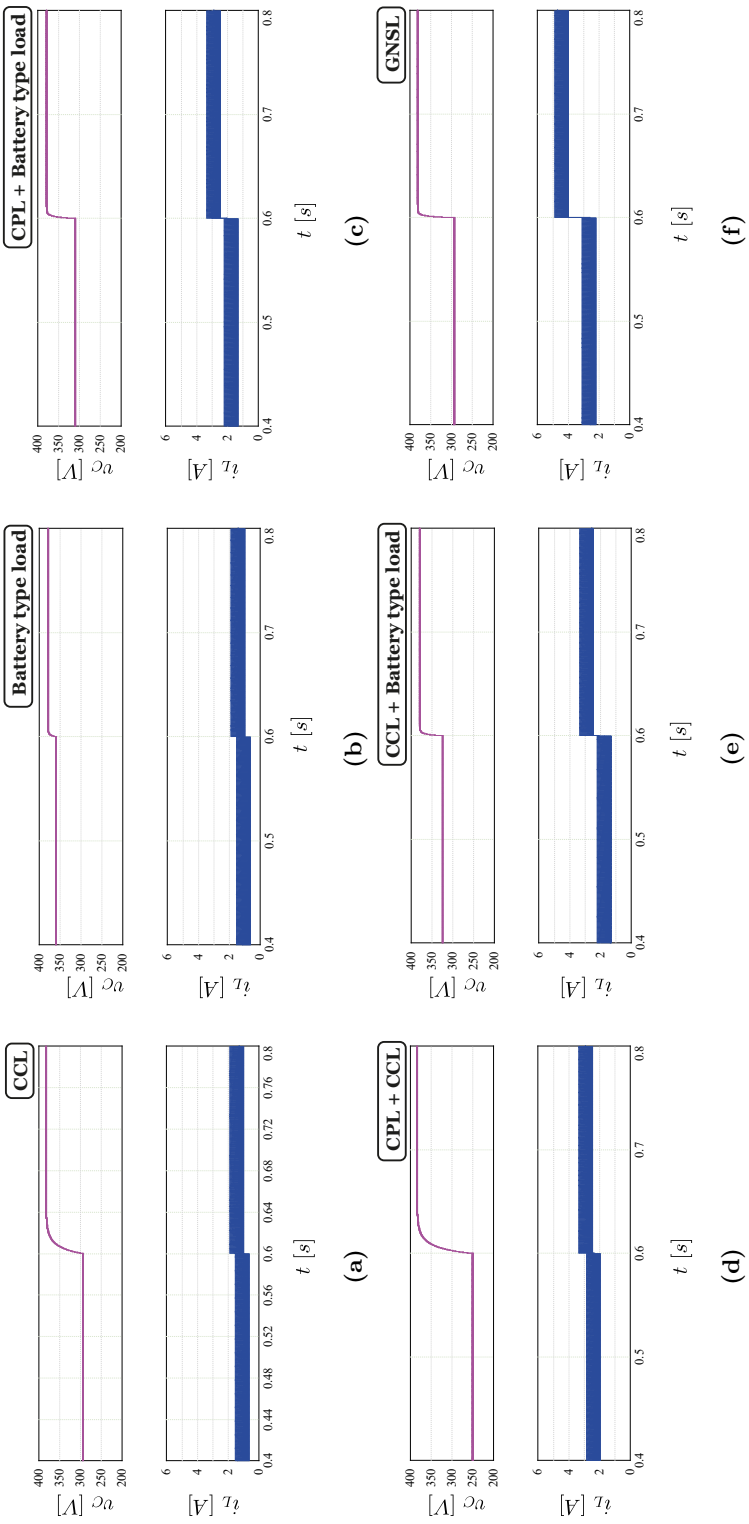

Fig. 4.10: Simulation results showing the system behavior when a step-type change is applied to the virtual resistance r and different combinations of elements in the GNSL are considered: a) CCL (r from 215 Ω to 164 Ω), b) Battery type load (r from 215 Ω to 164 Ω), c) Combination of a CPL with a battery type load (r from 136 Ω to 82 Ω), d) Combination of a CPL with a CCL (r from 100 Ω to 82 Ω), e) Combination of a CCL with a battery type load (r from 136 Ω to 82 Ω), and f) Combination of the three types of loads (r from 90 Ω to 54 Ω).

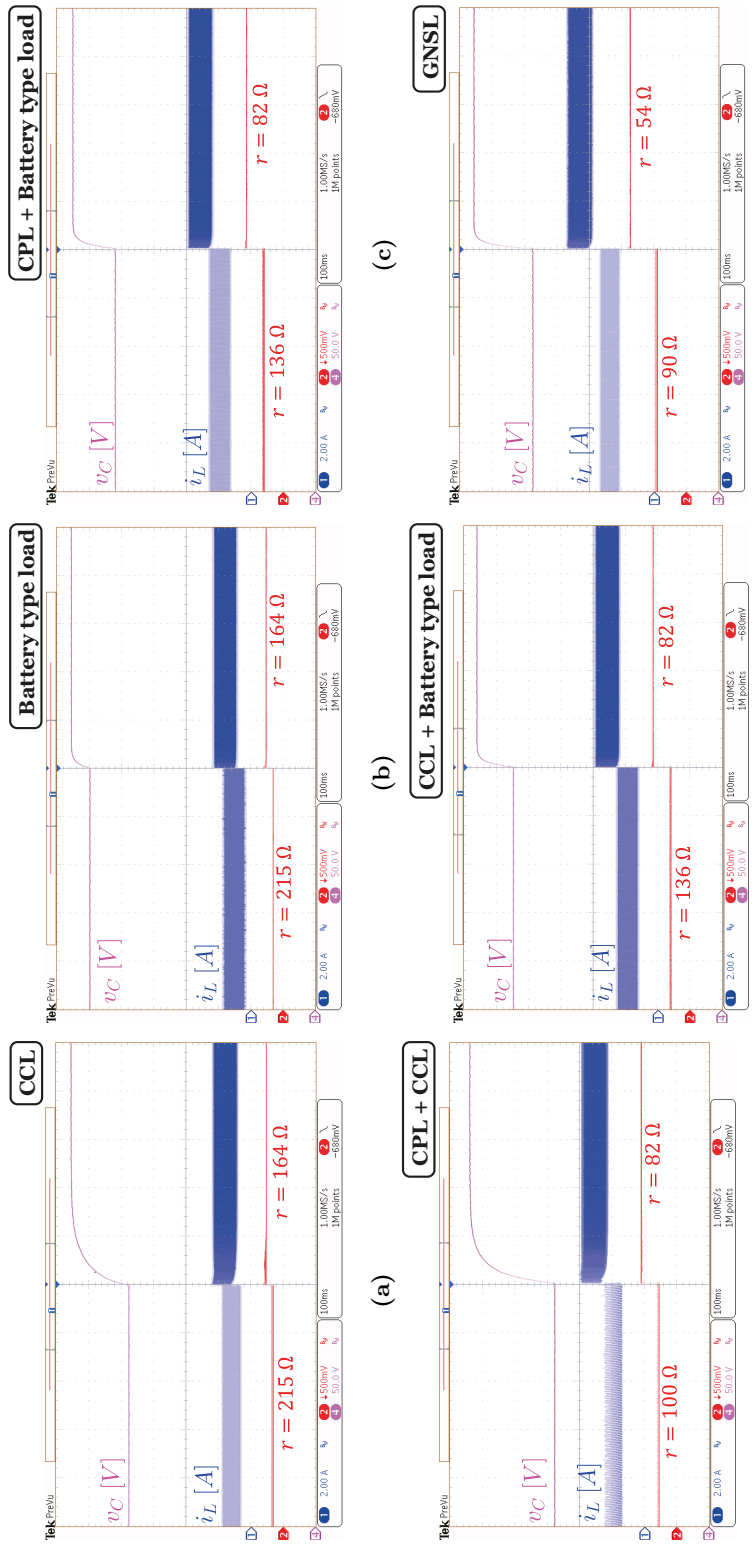

Fig. 4.11: Experimental results showing the system behavior when a step-type change is applied to the virtual resistance r and different combinations of elements in the GNSL are considered: a) CCL (r from 215 Ω to 164 Ω), b) Battery type load (r from 215 Ω to 164 Ω), c) Combination of a CPL with a battery type load (r from 136 Ω to 82 Ω), d) Combination of a CPL with a CCL (r from 100 Ω to 82 Ω), e) Combination of a CCL with a battery type load (r from 136 Ω to 82 Ω), and f) Combination of the three types of loads (r from 90 Ω to 54 Ω). Scales: Time – 100 ms/div, Ch. 1 (i_L) – 2 A/div, Ch. 2 (r) – 500 mV/div and Ch. 4 (v_C) – 50 V/div

Finally, we have simulated the case in which the converter controlled as an LFR feeds a pure CCL and compared its behavior with the one in open loop feeding the same type of load. Two equilibrium points have been selected corresponding to output power values of 350 and 500 W respectively. Considering an input voltage $V_g =$ 240 V, these points correspond to virtual resistances of $r = 164\ \Omega$ and $r = 115\ \Omega$ in the case of the LFR and duty cycles of $D = 0.37$ and $D = 0.56$ in the case of the converter operating in open loop.

As it can be observed in Fig. 4.12a, the system operating as an LFR feeding the CCL shows a stable behavior in the corresponding equilibrium points and in the transition between them. Unlike the LFR case, the steady-state for converter operating in open loop is characterized by a sustained oscillation around the equilibrium average value whose frequency is derived from expression (4.16) and given by

$$f_0 = \frac{1 - D}{2\pi\sqrt{LC}} \tag{4.16}$$

It can be observed in (4.16) that the oscillation frequency depends on the duty cycle and hence on the equilibrium point as illustrated in Fig. 12b. A higher value of the duty cycle results in a smaller value of the oscillation frequency.

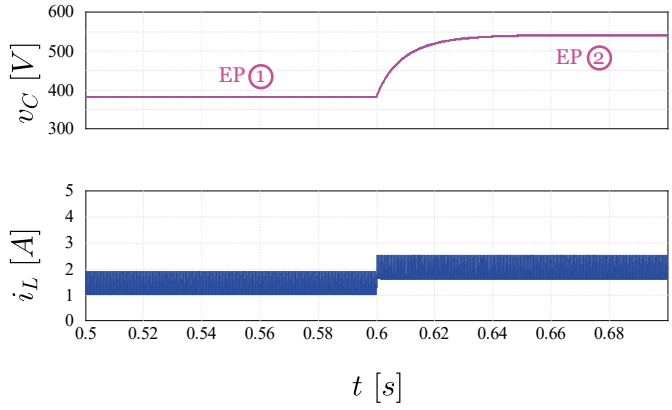

(a)

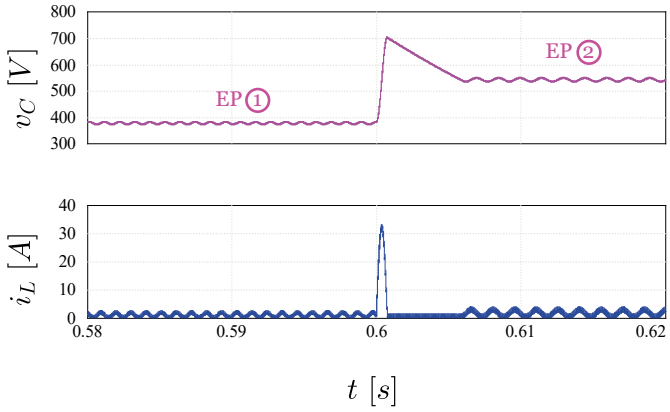

(b)

Fig. 4.12: Simulation results for a transition between two equilibrium points when the load is a CCL: a) change of the virtual resistance of the LFR from 64 to 115 Ω, and b) change of the duty cycle in open loop from 0.5 to 0.6.

4.4 Effect of conduction losses

Parasitic resistances are present in the final implementation of any power converter, and they mainly affect the resulting efficiency [65] but can also slightly change the expected value of the equilibrium output voltage in certain cases [66] or introduce a steady-state error in the estimated value of a load parameter [59]. In all cases, they model the conduction loss and are usually represented by a single resistor R_L in series with the inductor to characterize equally the loss effect in the inductor and transistor during on state or in the inductor and diode during off state.

Assuming a resistor R_L in series with the inductor in Fig. 4.1 results in the following expression of the equivalent control.

$$u_{eq}(x) = 1 - \frac{V_g - R_L i_L}{V_g} \tag{4.17}$$

Hence, the ideal sliding dynamics can be expressed as

$$\frac{dv_C}{dt} = \frac{V_g^2\left(1-\frac{R_L}{r}\right)}{Crv_C} - \frac{i_Z}{C} \tag{4.18a}$$

$$i_L = \frac{V_g}{r} \tag{4.18b}$$

By comparing (4.7) and (4.18) it can be observed that the term V_g^2 in (4.7) is modified by the factor $(1 - R_L/r)$ in (4.18), which represents the effect of the conduction loss. Therefore, the steady-state power balance given by (4.18) will be expressed now as

$$\frac{V_g^2\left(1-\frac{R_L}{r}\right)}{r} = P + V_C^* I_0 + \frac{V_C^{*2}}{R_B} - \frac{V_C^* V_B}{R_B} \tag{4.19}$$

It can be observed that the left term of (4.19) is the difference between the dc input power and conduction loss in steady-state. Hence, the horizontal coordinate V_C^* of the equilibrium point will be given by

$$V_C^*\Big|_{X_e} = \frac{V_B - I_0 R_B + \sqrt{\left(I_0 R_B - V_B\right)^2 + 4R_B\left[\frac{V_g^2\left(1-\frac{R_L}{r}\right)}{r} - P\right]}}{2} \tag{4.20}$$

In the design here reported the emulated resistance r ranges from 54 Ω to 215 Ω and a realistic assumption for R_L is 1 Ω, which implies that in all the examples considered above the following approximation applies

$$V_g^2\left(1-\frac{R_L}{r}\right) \approx V_g^2 \tag{4.21}$$

Hence, expression (4.20) becomes expression (4.9) and therefore it can be concluded that the parasitic resistance R_L has a negligible effect in the coordinates of the equilibrium point provided that its value is considerably smaller than the virtual resistance r.

Similarly, the stability condition (4.14) becomes

$$\frac{V_g^2\left(1-\frac{R_L}{r}\right)}{rV_C^{*2}} > \frac{P}{V_C^{*2}} \tag{4.22}$$

Condition (4.22) is always fulfilled because the input power is higher than the sum of the power absorbed by the CPL and the conduction loss. Nonetheless, the effect of the parasitic resistance R_L on the equilibrium point coordinates can be significant for small values of the emulated resistance r.

Fig. 4.13 shows simulated results regarding the steady-state and transient behavior of a non-ideal boost converter operating as LFR and feeding a GNSL composed by the three studied elements ($V_g = 240\ V, P = 350\ W,\ I_o = 0.92\ A, R = 100\ \Omega$ and $V_B = 287\ V$). The test consists in comparing the steady-state values and the transient response of the system for three different values of the parasitic resistance R_l (0 Ω, 1 Ω and 27 Ω) when a sudden change is applied in the reference of the input virtual resistor value r (from 90 Ω to 54 Ω). As it can be observed, the difference between the cases of 0 Ω and 1 Ω is imperceptible. Also, as predicted, for very large values of R_L the equilibrium point suffers a deviation caused by the loss of efficiency in the system. Complementarily, it is possible to observe that the transient response does not suffer a considerable deviation with the increment of the parasitic resistance. These results allow to confirm the validity of the theoretical study based on the ideal converter.

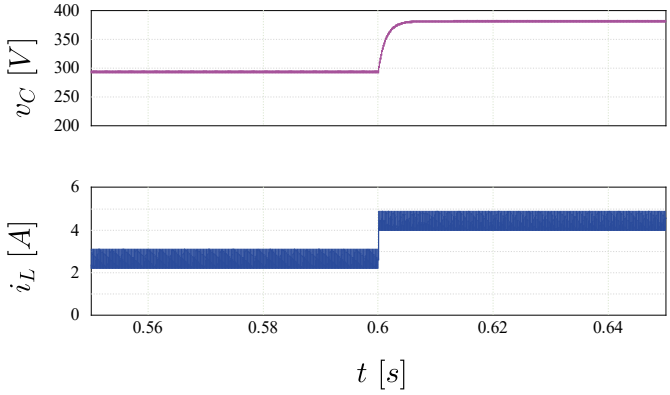

(a)

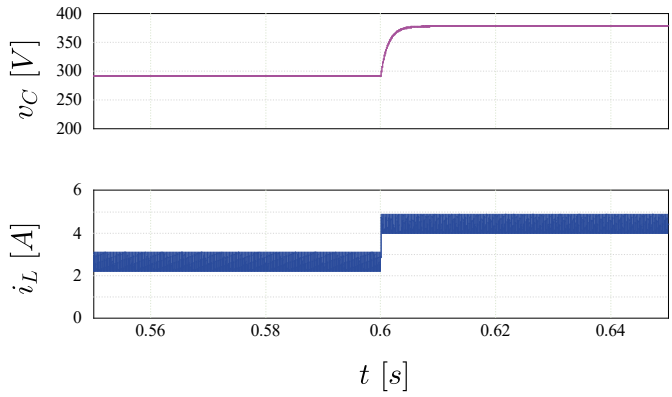

(b)

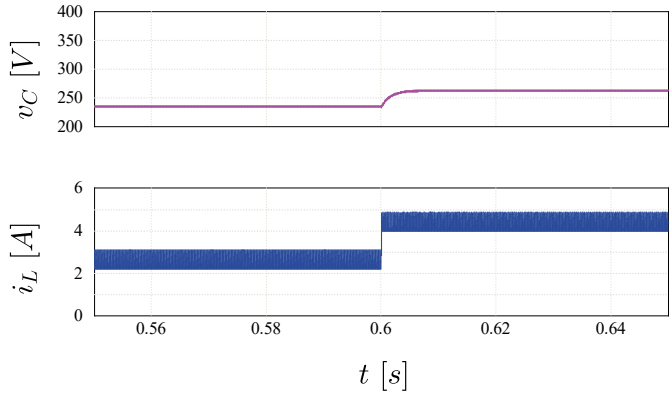

(c)

Fig. 4.13: Simulation results for a transition between two equilibrium points regarding the effect of the parasitic resistance R_L: (a) 0 Ω, (b) 1 Ω and (c) 27 Ω.

4.5 Conclusions

From the observation of the type of load used in a classical power electronics equipment (resistor) and in new applications like electric vehicles and microgrids (CPL, CCL, and battery), a parallel combination of three of them to introduce the notion of GNSL is proposed. A realistic scenario in modern power distri-

bution systems is a dc bus supplying a combination of the mentioned loads characterized by GNSL.

The design of a boost converter with LFR characteristics in the role of a dc bus has allowed the transference of regulated power to the GNSL. The SMC approach has demonstrated that there is a single equilibrium point, which is unconditionally stable. The particularization of the GNSL in two cases of single load, six cases of couple of loads and four cases of three-load combination has also resulted in a stable equilibrium point in each case. The stability is guaranteed by the active damping introduced by the virtual resistance of the LFR.

Nevertheless, if the LFR supplies only a CPL, the power of the source and the power of the sink must be equal to keep the POPI nature of the converter, which yields an infinite number of equilibrium points with marginally stable behavior. Setting a stable point in this case requires an external voltage control loop to ensure a single point of equilibrium.

In the real implementation of the LFR, conduction losses do not affect the dynamic behavior, but they result in a deviation from EP because of the power dissipation caused by parasitic resistances. A significant effect due to losses would only appear if small values of virtual resistance were used.

UNIVERSITAT ROVIRA I VIRGILI
A SLIDING MODE APPROACH TO CONTROL POWER SINKS AND POWER SOURCES IN DC-DC SWITCHING CONVERTERS
David Alejandro Zambrano Prada

Chapter 5

Potential applications of LFR and PET: constant power - constant voltage battery charging based on a loss-free resistor approach

Introduction

There is a clear consensus in admitting that the main obstacles that complicate the market penetration of EVs are the so-called range anxiety (fear of not having enough charge in the vehicle), customer price, charging time and charging availability, all of them related to the battery [67]. To overcome these barriers, fast charging technique has emerged in the last years, which represents a short time of charging for both battery and energy supply system [22].

Fast charging is a multidisciplinary problem that requires a joint perception of the physical phenomena related to the battery technology and the electronic system interfacing a primary energy source and the battery. Charging is often measured in terms of C, i.e., the nominal charging capacity of the battery in Ah [68], so 0.5C or less corresponds to conventional charging while values higher or equal than C are typical of fast charging. The high currents involved in the

latter case often result in energy efficiency reduction, thermal runaway, and fast degradation of characteristics, i.e., a decrease of both capacity and power of the battery.

It is accepted that ten minutes fast charging could be a suitable target because it would require batteries made up of abundant and accessible raw materials at affordable cost. An experiment in that direction is the work reported in [23], in which the authors succeed in charging an energy-dense battery of 265 Wh/kg to 70% state of charge (SOC) in 11 minutes for more than 2,000 cycles. 4C charging is achieved with correct cooling and safe operation due to appropriate air convection in a thermally stable electrolyte.

Charging techniques can be classified into open and closed-loop categories [69]. In the first case, there is no information fed back to the system input while in the second case the charging process is regulated dynamically. Open loop techniques are characterized by a profile-based approach whereas closed-loop procedures are model-based allowing the formulation of an optimization problem, which is eventually solved by means of fuzzy logic or genetic algorithms. Profile-based techniques consist in a first phase of either CC, constant power (CP), multistage constant current (MCC), pulse charging , boost charging or variable current, followed in most cases by an interval of CV [70]. The most common charging protocol is the CC-CV.

In the research of methods and profiles about battery charging, a large part of the literature on the subject focuses on the electrochemical aspects, the reports being mainly technology related papers. Strictly speaking, the first recent overview of charging methods from a power electronics perspective is the work described in [71]. In that paper, the authors analyze battery charging methods in terms of converter topologies, power levels and control strategies. Based on the current cost of the materials, they also develop an estimation model using a genetic algorithm to forecast the optimal capacity size of a battery and the power rating of the associated on and off-board chargers. On the other hand, in what regards the electrical architecture of a fast charging station, selecting the appropriate unidirectional dc-dc converter topology for the output stage has to take into account several factors such as the number of charging points, type of power distribution in the electrical architecture , and existence of galvanic isolation as described in [72].

In this context, it makes sense to explore the electronic implementation

of some of the charging protocols by selecting an appropriate converter and describing the main features of the resulting experiments in electronic terms; namely, efficiency, stress, stability, and number of components.

For the purposes of this research, a CP-CV protocol is the most adequate for a comparative study with respect to the typical CC-CV. Both protocols use the same number of charging stages and have equivalent parameters for comparison. Regarding efficiency, simulations of a CV-CV procedure have shown improvements of up to 4% in loss reduction and better heat treatment at 50 kW ultrafast charging from 20% to 90% of SOC in comparison with the traditional CC-CV technique under the identical conditions [73].

We have shown in Chapter 4 that an SMC-based LFR can supply power to the particular case of a GNSL made up of a voltage source with a series resistance yielding a single stable EP. This approach is based on the two-port circuit model of the dc-dc switching converters, which is not only a formal aspect, but it is rather an insightful tool in practical cases.

Thus, the same power converter could be used to produce the different charging phases, synthetizing by control a convenient canonical element that complies with the required charging specifications.

5.1 Canonical elements for battery charging

The standard protocol for battery charging consists of a constant current charging interval (CC phase), in which the battery voltage increases up to attain a desired value V_{B_F}, followed by a constant voltage interval (CV phase) hold until the current decreases to the vicinity of zero. An alternative protocol of the type of CP-CV is made up of a constant power interval (CP phase) similar to that of the standard protocol. Fig. 5.1a. and Fig. 5.1b show respectively the main features of the CC-CV and CP-CV charging protocols, while Fig. 5.1c illustrates the power curves during charging.

We assume in this work that the primary energy source is a regulated dc voltage V_g supplied by an appropriate internal bus of a battery charging station. Therefore, a non-isolated dc-dc switching converter will be the interface between the dc bus and the battery in order to perform the required charging protocol. Irrespective of the function it performs, a switching converter can be modelled by any of the three canonical elements for power processing: a dc transformer

[73], a power gyrator [74], and a loss-free resistor [75].

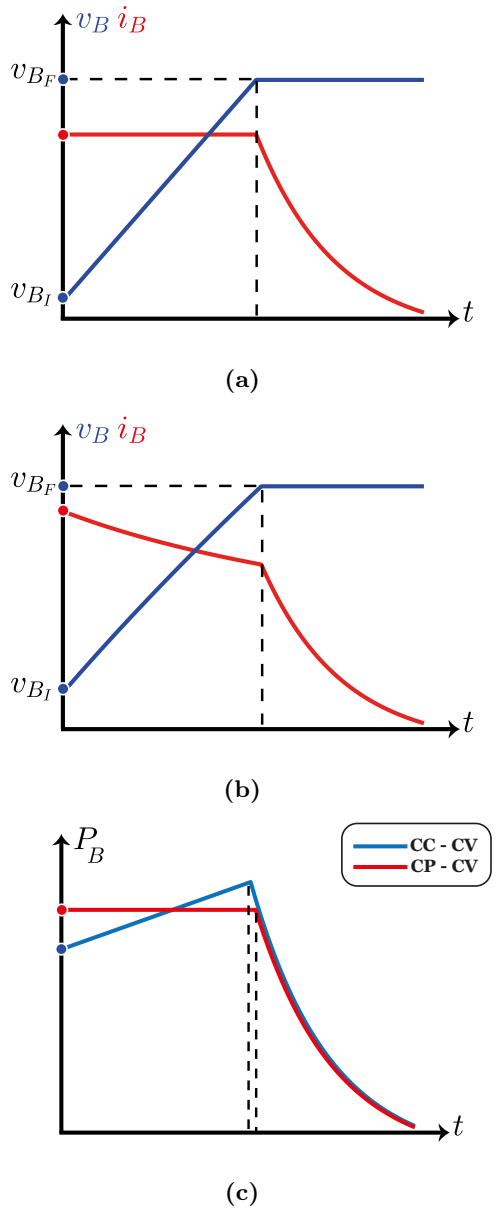

Fig. 5.1: Battery charging protocols (i_B=battery current; v_B=battery voltage): (a) standard CC-CV, (b) CP-CV and (c) power curves.

On the other hand, what distinguishes the standard protocol from the CP-CV alternative is the first phase, which can be either performed at constant current or at constant power. Hence, it makes sense to explore the CC phase under the optics of a dc transformer or a power gyrator, and to study the CP interval with the LFR approach as illustrated in Fig. 5.2. It can be observed in the transformer case that the battery current i_B in steady-state will be constant if the input current is constant and an appropriate constant value for the duty cycle D, and hence the transformer ratio $n(D)$, is used.

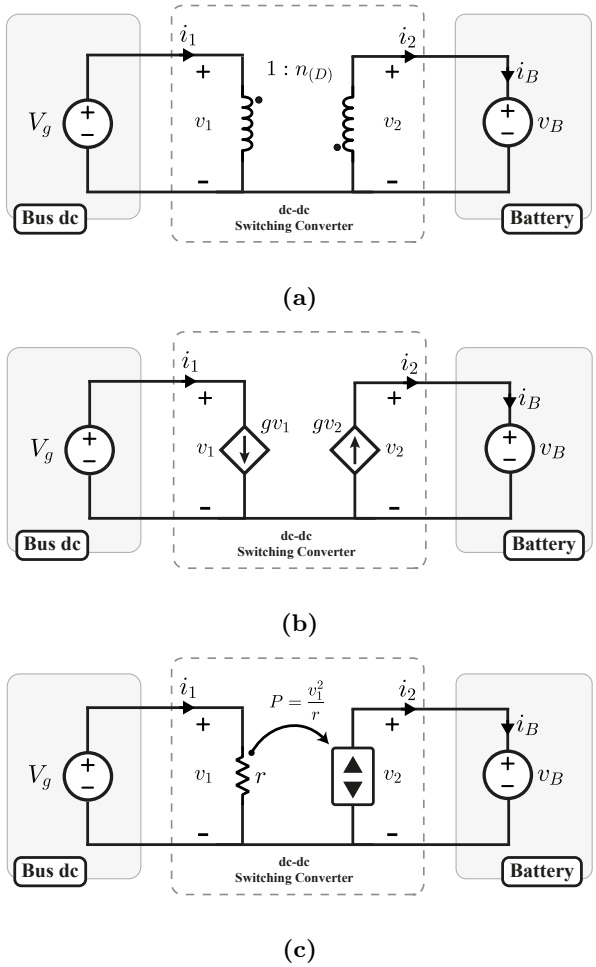

Fig. 5.2: Modelling the first phase of battery charging by means of a canonical. (a) dc transformer, (b) power gyrator and (c) LFR.

$$v_2 = n(D)v_2 \tag{5.1a}$$

$$i_2 = \frac{i_1}{n(D)} \tag{5.1b}$$

$$i_1 = g(D)v_2 \tag{5.2a}$$

$$i_2 = g(D)v_1 \tag{5.2b}$$

$$i_1 = \frac{v_1}{r} \tag{5.3a}$$

$$v_2 i_2 = r i_1^2 \tag{5.3b}$$

Similarly, using a power gyrator will yield a constant value of the battery current by imposing proportionality in steady-state between the output current and the input voltage if an appropriate value of the conductance $g\,(D)$, and therefore of the duty cycle, is employed. In a clear-cut contrast, the LFR feeds the battery with the constant power absorbed by the emulated resistor r at its input port.

A boost converter is apparently a good candidate for the LFR approach since it results with LFR behavior in a single stable EP when loaded with a generic nonlinear static load that can be particularized as a battery as seen in Chapter 4. However, the output current is discontinuous, which introduces an undesired ripple in the battery and precludes its control in sliding-mode. This drawback has led as to include an output filter, and therefore to consider a BOF as the power converter on which both CC-CV and CP-CV protocols can be theoretically studied and verified by experiments.

5.2 SMC-based design of canonical elements

Fig. 5.3 shows the block diagram of a sliding-mode controlled BOF unidirectional battery charger. Transistor Q and diode D are assumed ideal and no parasitics are considered. Losses on the passive components are neglected. For the sake of the subsequent implementation, a general sliding surface model up of a linear combination of both input and output ports variables is represented in the figure.

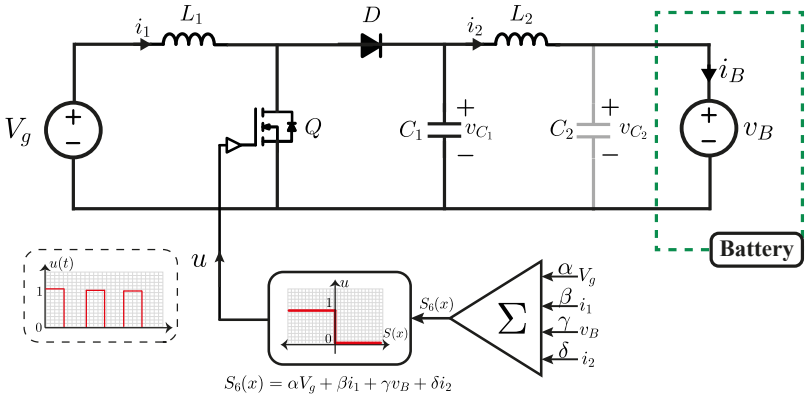

Fig. 5.3: Block diagram of a sliding-mode controlled BOF unidirectional battery charger.

It is worth mentioning that capacitor C_2 is optional since its filtering effects can be accomplished by the internal capacity of the battery. For that reason, C_2 will not be considered in our analysis and hence the battery charging current will be i_2. Therefore, the expression of the sliding surface $S_6(x)$ will be given by

$$S_6(x) = \alpha V_g + \beta i_1 + \gamma v_B + \delta i_2 \tag{5.4}$$

It can be observed that particularizing expression (5.4) for certain parameter values might result in: (i) a dc transformer [77], (ii) a power G-gyrator of type I [78]. (iii) a power G-gyrator of type II [79], and (iv) a loss-free resistor [13]. The four cases and the corresponding parameter constraints are summarized in Table 5.1

Table 5.1: Particularizing $S_6(x)$ for canonical elements implementations.

Parameter constraint	Sliding surface	Canonical element
$\alpha = \gamma = 0$	$S_{6a}(x) = \beta i_1 + \delta i_2$	dc transformer
$\beta = \gamma = 0$	$S_{6b}(x) = \alpha V_g + \delta i_2$	G-gyrator type I
$\alpha = \delta = 0$	$S_{6c}(x) = \beta i_1 + \gamma v_B$	G-gyrator type II
$\gamma = \delta = 0$	$S_{6d}(x) = \alpha V_g + \beta i_1$	LFR

The control law to keep the state trajectory switching above and below surface $S_6(x)$ is derived from the conditions for existence of sliding motions.

$$\frac{dS_6(x)}{dt} < 0 \quad \text{if} \quad S_6(x) > 0 \tag{5.5a}$$

$$\frac{dS_6(x)}{dt} > 0 \quad \text{if} \quad S_6(x) < 0 \tag{5.5b}$$

The above conditions are fulfilled when the switching law is given by

$$u = \begin{cases} 0, & \text{if, } S_6(x) > +\Delta \\ 1, & \text{if, } S_6(x) < -\Delta \end{cases} \tag{5.6}$$

5.2.1 State equations

In CCM, the converter in Fig. 5.2 can be described in compact form by the following set of differential equations.

$$\frac{di_1}{dt} = \frac{V_g}{L_1} - \frac{v_{C_1}}{L_1}(1-u) \tag{5.7a}$$

$$\frac{di_2}{dt} = \frac{v_{C_1}}{L_2} - \frac{v_B}{L_2} \tag{5.7b}$$

$$\frac{dv_{C_1}}{dt} = \frac{i_1}{C_1}(1-u) - \frac{i_2}{C_1} \tag{5.7c}$$

$$\tag{5.7d}$$

5.2.2 Existence of sliding mode

Assuming a constant input voltage V_g, the time-derivative of $S_6(x)$ can be expressed as follows

$$\dot{S}_6(x) \triangleq \frac{dS_{6(x)}}{dt} = \beta\frac{di_1}{dt} + \gamma\frac{dv_B}{dt} + \delta\frac{di_2}{dt} \tag{5.8}$$

Taking into account condition (5.8) and the switching policy given by expression (5.6), we study next the existence of sliding mode in the four cases illustrated in Table 5.1.

5.2.2.1 dc transformer

The constraint $\gamma = 0$ in (5.8) yields

$$\frac{dS_6(x)}{dt} = \beta\frac{di_1}{dt} + \delta\frac{di_2}{dt} \tag{5.9}$$

On the other hand, $S_6(x) < 0$ implies u=1 and therefore expression (5.9) becomes

$$\frac{dS_6(x)}{dt} = \beta\frac{V_g}{L_1} + \delta\frac{(v_{C_1} - v_B)}{L_2} > 0 \tag{5.10}$$

In steady-state $v_{C_1} = v_B$, which implies

$$\frac{dS_6(x)}{dt} = \beta \frac{V_g}{L_1} > 0 \tag{5.11a}$$

$$\forall \beta > 0 \tag{5.11b}$$

Similarly, $S_6(x) > 0$ implies $u = 0$, and hence expression (5.9) results in

$$\frac{dS_6(x)}{dt} = \beta \frac{(V_g - V_{C_1})}{L_1} + \delta \frac{\left(v_{\{C_1\}} - v_B\right)}{L_2} < 0 \tag{5.12}$$

In steady-state, $v_{C_1} = v_B$ and $V_g < v_{C_1}$, which yields

$$\frac{dS_6(x)}{dt} = \beta \frac{(V_g - V_{C_1})}{L_1} < 0 \tag{5.13}$$

Therefore, the control law given by expression (5.6) induces sliding motions in a dc transformer based on BOF.

5.2.2.2 G-gyrator of type I

The constraints in the parameters are $\beta = \gamma = 0$, which results in

$$\frac{dS_6(x)}{dt} = \delta \frac{di_2}{dt} = \delta \frac{\left(v_{\{C_1\}} - v_B\right)}{L_2} \tag{5.14}$$

Since expression (5.14) doesn't depend on the control variable u and, in addition, is zero in steady-state, there will be no sliding-mode in this case.

5.2.2.3 G-gyrator of type II

In this case, the constraint $\delta = 0$ in (5.8) results in

$$\frac{dS_6(x)}{dt} = \beta \frac{di_1}{dt} + \gamma \frac{dv_B}{dt} \tag{5.15}$$

Therefore, $S_6(x) < 0$ and $u = 1$ leads to

$$\frac{dS_6(x)}{dt} = \beta\frac{V_g}{L_1} + \gamma\frac{dv_B}{dt} > 0 \tag{5.16}$$

where the second term is greater than zero because $v_B(t)$ is a growing function of time in charging process.

Assuming $\beta > 0$, expression (5.16) will be positive if the following condition is fulfilled

$$V_g > \left|\frac{\gamma L_1}{\beta}\right| \frac{dv_B}{dt} \tag{5.17}$$

For $S_6(x) > 0$ and $u = 0$, expression (5.15) becomes

$$\frac{dS_6(x)}{dt} = \beta\frac{V_g - v_{C_1}}{L_1} + \gamma\frac{dv_B}{dt} < 0 \tag{5.18}$$

Since $V_g - V_{C_1} < 0$ in steady-state, expression (5.18) will be negative if $\gamma < 0$. Since expression (5.15) can be positive and expression (5.18) negative with an appropriate selection of β and γ, it can be concluded that the control law (5.6) will lead to a sliding behavior in a G-gyrator of type II based on BOF.

5.2.2.4 Loss-free resistor

Introducing $\gamma = \delta = 0$ in (5.8) results in

$$\frac{dS_{6d}(x)}{dt} = \beta\ \frac{di_1}{dt} \tag{5.19}$$

Hence, for $S_6(x) < 0$ and $u = 1$, expression (5.19) becomes

$$\frac{dS_6(x)}{dt} = \beta \frac{\beta V_g}{L_1} > 0 \tag{5.20a}$$

$$\forall \beta > 0 \tag{5.20b}$$

which is again inequality (5.11). Also, for $S_6(x) > 0$ and $u = 0$, we obtain inequality (5.13). Therefore, the control given by expression (5.8) will generate sliding motions in BOF-based loss-free resistor.

5.2.3 Equivalent control and ideal sliding dynamics

In sliding mode, the converter dynamics is subjected to the constraints $S_6(x) = 0$ and $\dot{S}_6(x) = 0$. Therefore, equaling (5.8) to zero leads to the following general expression of the equivalent control:

$$u_{6_{eq}} = 1 - \frac{V_g + \frac{L_1\delta}{L_2\beta}\ (v_{C_1} - v_B)\ + \frac{L_1\gamma}{\beta}\frac{dv_B}{dt}}{v_{C_1}} \tag{5.21}$$

Introducing expression (5.21) in the converter state equations given by (5.7) and imposing the different constraints of Table 1 will yield the ideal sliding dynamics for dc transformer, G-gyrator of type II, and loss-free resistor.

5.2.3.1 dc transformer

In this case $S_{6a}(x) = 0$ implies $i_2 = -(\beta/\delta)i_1$, and $\gamma = 0$ leads to

$$u_{6a_{eq}} = 1 - \frac{V_g + \frac{L_1\delta}{L_2\beta}\ (v_{C_1} - v_B)}{v_{C_1}} \tag{5.22}$$

Hence, the ideal sliding dynamics will be given by

$$\frac{di_1}{dt} = -\frac{\delta\left(v_{C_1} - v_B\right)}{\beta L_2} \tag{5.23a}$$

$$\frac{dv_{C_1}}{dt} = \frac{i_1\left(V_g + \frac{L_1\delta}{L_2\beta}\left(v_{C_1} - v_B\right)\right)}{C_1 v_{C_1}} + \frac{\beta i_1}{C_1\delta} \tag{5.23b}$$

5.2.3.2 G-gyrator of type II

In sliding-mode $S_{6c}(x) = 0$, which implies for this type of gyrator $i_1 = -(\gamma/\beta)v_B$. On the other hand, $\delta = 0$ leads to the following expression of the equivalent control.

$$u_{6c_{eq}} = 1 - \frac{V_g + \frac{L_1\gamma}{\beta}\frac{dv_B}{dt}}{v_{C_1}} \tag{5.24}$$

Consequently, the ideal sliding dynamics can be expressed as follows

$$\frac{di_2}{dt} = -\frac{\left(v_{C_1} - v_B\right)}{L_2} \tag{5.25a}$$

$$\frac{dv_{C_1}}{dt} = -\frac{\gamma v_B}{\beta}\frac{V_g + \frac{L_1\gamma}{\beta}\frac{dv_B}{dt}}{C_1 v_{C_1}} - \frac{i_2}{C_1} \tag{5.25b}$$

5.2.3.3 Loss-free resistor

In the LFR behavior, the sliding-mode will be characterized by $i_1 = -(\alpha/\beta)V_g$. Besides, the constraints $\delta = \gamma = 0$ yield the following expression of the equivalent control.

$$u_{6d_{eq}} = 1 - \frac{V_g}{v_{C_1}} \tag{5.26}$$

Consequently, the ideal sliding dynamics can be expressed as follows

$$\frac{di_1}{dt} = -\frac{(v_{C_1} - v_B)}{L_2} \tag{5.27a}$$

$$\frac{dv_{C_1}}{dt} = -\frac{\alpha V_g^2}{\beta C_1 v_{C_1}} - \frac{i_2}{C_1} \tag{5.27b}$$

5.2.4 Equilibrium point description

By equaling to zero equations (5.23), (5.25) and (5.27), the expression of EP in the dc transformer, G-gyrator of type II, and LFR cases is obtained. The value of the capacitor voltage v_{C_1} in equilibrium is equal to that of the battery voltage in the three cases, i.e., $V_{C_1}^* = V_B^*$, where the asterisk stands for the EP.

In all three cases, the nature of POPI circuit is verified at the EP while the particular features of each case are the following

$$I_2^* = -\frac{\beta}{\delta} I_1^* \quad \text{dc transformer} \tag{5.28a}$$

$$I_1^* = -\frac{\gamma}{\beta} V_B^* \quad \text{G-gyrator of type II} \tag{5.28b}$$

$$I_1^* = -\frac{\alpha}{\beta} V_g \quad \text{LFR} \tag{5.28c}$$

5.2.5 Stability conditions

Linearizing equations (5.23), (5.25) and (5.27) around their corresponding EP results in the characteristic equation $s^2 + bs + c = 0$, whose coefficients are shown in Table 5.2 for each canonical element together with the conditions to ensure both stability and the existence of sliding mode.

Among the three synthesized canonical elements, the dc transformer presents the most restrictive operating and stability condition. If we define $n = -\delta/\beta$, the maximum gain value will be bounded by the static voltage gain $M = V_B^*/V_g > n$, thus limiting the maximum power that can be delivered to the battery. In addition, in open-loop it is not possible to establish an operating point through the gain n because the synthetized dc transformer by $S_{6a}(x)$ is a self-oscillating converter in which the transformer ratio depends on the power stage parameters.

Table 5.2: Particularizing $S_6(x)$ for canonical elements implementations.

Canonical element	b	c	Stability	Sliding motion
dc transformer	$\frac{\frac{\delta I_2^*}{\beta V_B^*}\left(\frac{V_g}{V_B^*}-\frac{\delta L_1}{\beta L_2}\right)}{C_1 V_{C_1}^*}$	$1+\frac{\delta V_g}{\beta V_B^*}$	$\beta>0$ $\delta<0$ $\left\|\frac{\delta}{\beta}\right\|<\left\|\frac{V_B^*}{V_g}\right\|$	$\beta>0$
G-gyrator of type II	$-\frac{\gamma V_g}{\beta C_1 V_{C_1}^*}$	$\frac{1}{L_2 C_1}$	$\beta>0$ $\gamma<0$	$\beta>0$ $\gamma<0$ $\frac{\beta V_g}{L_1}+\gamma\frac{dv_B}{dt}>0$
Loss-free resistor	$-\frac{\alpha V_g^2}{\beta C_1 {V_{C_1}^*}^2}$	$\frac{1}{L_2 C_1}$	$\beta>0$ $\alpha<0$	$\beta>0$

Under these conditions, the best alternative to CC phase would correspond to a G-gyrator of type II. However, the G-gyrator in open-loop with a fixed conductance $g=-\gamma/\beta$ has not a constant output current i_2 during the charging process and would require the insertion of a closed-loop through the variable g in order to regulate the current.

5.3 Battery charging control

5.3.1 Control diagram description

Fig. 5.4 presents the general diagram block of a battery charging control. It is divided into two parts: the first is the charging phase, corresponding to (i) CC stage for the G-gyrator or (ii) CP state for the LFR, and the second phase is a common CV phase as discussed in section 5.1.

The converter is controlled by the variable k(t),whose value depends on the type of canonical element and is given as follows

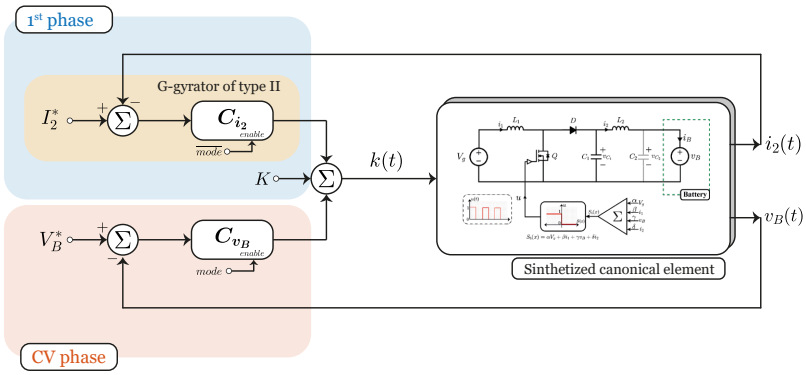

Fig. 5.4: Diagram block of battery charging control.

$$k_1(t) = -\frac{\gamma(t)}{\beta} = g_{gyr} \tag{5.29a}$$

$$k_2(t) = -\frac{\alpha(t)}{\beta} = g_{LFR} = \frac{1}{r} \tag{5.29b}$$

Where k_1 and k_2 are related to the transconductance of G-gyrator and virtual conductance of LFR, respectively. Thus, $k(t)$ is provided by each stage and tends to a constant value. In order to achieve a soft start-up, the constant value can be reached after a first order transient state given by

$$K = K_o\left(1 - e^{-\tau t}\right) \tag{5.30}$$

which K_o is the desired value and τ is the time constant. For the CP stage, an appropriate value of K_o guarantees the constant power in the output port. On the other hand, for CC stage the controller C_{i_2} is enabled when $K_1(5\tau) = K_{1o}$, which ensures a constant current to battery.

In CV phase, both G-gyrator and LFR use the controller C_{v_B} to regulate the battery voltage. C_{i_2} and C_{v_B} are activated by the binary variable mode $\in [0, 1]$, where $\overline{mode} \triangleq mode = 0$ enables the first phase of charging, while $mode = 1$ allows the CV phase.

5.3.2 Small-signal dynamics in sliding motion

In sliding motion, the transfer functions of small-signal to output port of the corresponding canonical elements are governed by equations (5.31) and (5.32) for the G-gyrator, and (5.33) and (5.34) for the LFR.

$$\frac{I_2(s)}{k_1(s)} = \frac{\frac{V_g}{L_2C_1} - \frac{L_1V_B^*g_{gyr}^*}{L_2C_1}s}{s^2 + \frac{V_g g_{gyr}^*}{C_1V_B^*}s + \frac{1}{L_2C_1}} \tag{5.31}$$

$$\frac{V_{c_1}(s)}{k_1(s)} = \frac{\frac{V_g}{L_2C_1}s - \frac{L_1V_B^*g_{gyr}^*}{C_1}s^2}{s^2 + \frac{V_g g_{gyr}^*}{C_1V_B^*}s + \frac{1}{L_2C_1}} \tag{5.32}$$

$$\frac{I_2(s)}{k_2(s)} = \frac{\frac{V_g^2}{V_B^*\ L_2C_1} - \frac{L_1V_g^2g_{gyr}^*}{V_B^*\ L_2C_1}s}{s^2 + \frac{V_{g^2}g_{LFR}^*}{C_1V_B^{*2}}s + \frac{1}{L_2C_1}} \tag{5.33}$$

$$\frac{V_{C_1}(s)}{k_2(s)} = \frac{\frac{V_g^2}{V_B^*\ C_1}s - \frac{L_1V_g^2g_{gyr}^*}{V_B^*\ C_1}s^2}{s^2 + \frac{V_{g^2}g_{LFR}^*}{C_1V_B^{*2}}s + \frac{1}{L_2C_1}} \tag{5.34}$$

Assuming an equal dc voltage gain, e.g., $V_B^* = 2V_g$, and implementing in the same converter and with the same parameters both G-gyrator and LFR, the characteristic equation from (5.31) and (5.32) for the gyrator and LFR is the same are when power balance is guaranteed, i.e., $V_g i_1 = i_2 V_B^*$. This fact is verified in Fig. 5, where the response i_2 and v_{C_1} to a step variation of k_1 or k_2 using the parameters of Table 5.3.

Table 5.3: Parameter values of numerical simulation of BOF with battery load.

Parameter	Values
L_1	100 μH
L_2	100 μH
C	20 μF
V_g	24 V
V_B^*	48 V

5.3.3 Control design considerations

The small-signal behavior in Fig. 5.5 is underdamped in both cases and has a non-minimum phase zero. In terms of control design, this one of the worst-cases scenarios. However, in charging process the battery dynamic behavior is slower than the converter dynamics, this allowing a smooth transition. Therefore, the smoothness of voltage capacitor v_{C_1} and current inductors i_1 and i_2 are ensured all time together with the soft start-up expressed in (5.30),

Under these conditions, the design requirements are more relaxed and classical linear controllers, such as PI or PID, may be used.

By considering power losses in the converter due to parasitic resistances R_{L_1} and R_{L_2} in inductors L_1 and L_2 respectively, the following constraints are imposed for k_1 and k_2.

$$k_1 < \frac{V_g}{R_{L_1} v_B} \triangleq g_{max} \tag{5.35}$$

$$k_2 = \frac{1}{r} < \frac{1}{R_{L_1}} \tag{5.36a}$$

$$r > R_{L_1} \triangleq r_{min} \tag{5.36b}$$

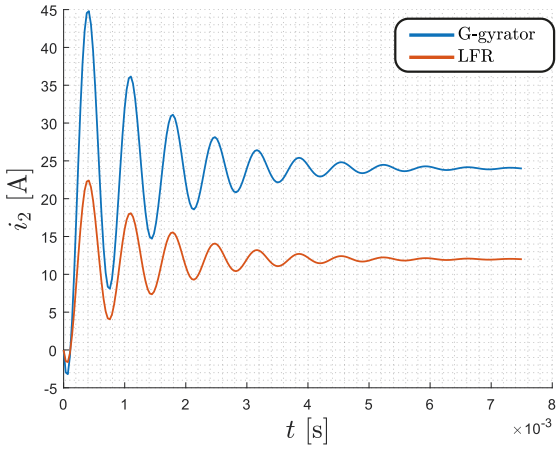

(a)

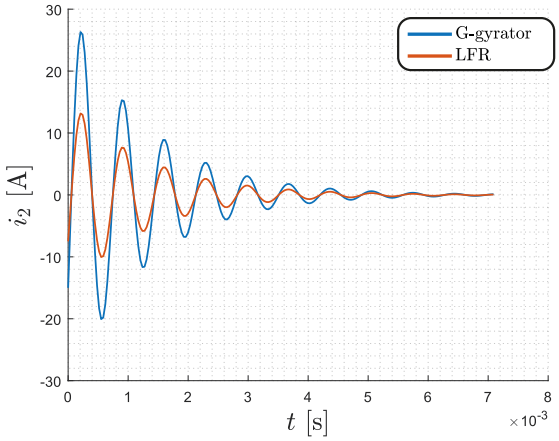

(b)

Fig. 5.5: Small–signal response to step variations of k_1 (gyrator) or k_2 (LFR) in sliding motion. (a) output current i_2 and (b) capacitor voltage v_{C_1}

Ultrafast charging demands high current at the output port of a single converter which leads to g value in a G-gyrator or a r value in an LFR that may exceed these limits expressed above. This is especially relevant in the step-up converter, where the constraints (5.35) and (5.36) are associated with the input current, which is higher than the output current. In addition , it should be taken into account reduced efficiency and the required thermal management.

Finally, it would be possible paralleling the output connections of the converters synthetized as output current sources or output power sources. From a standard BOF converter module, a democratic current (power) distribution

strategy can could be applied, where the total transconductance (virtual resistance) would be divided among the m different modules. Thus, each module would synthesize a G-gyrator with $g = g_{Total}/m$ or a LFR with $r = r_{Total}/m$. This approach would allow increasing the flexibility and the power efficiency of the system. As an example, Fig. 5.6 shows the control scheme for $m = 3$, controlling three BOF converters in parallel.

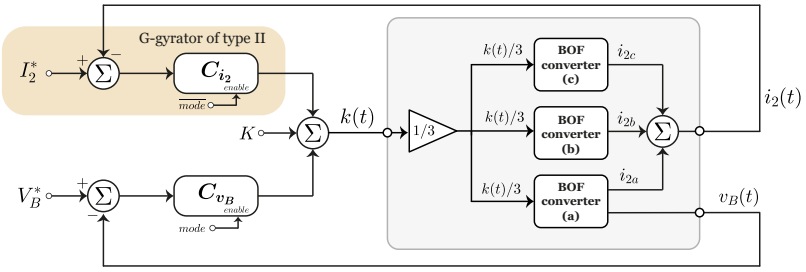

Fig. 5.6: Battery control scheme for three standard BOF converters with a democratic distribution approach.

5.3.4 Simulation results

In order to test the battery charging strategy, simulations in PSIM© for the scheme presented in Fig. 5.6 have been performed. Table 5.4 summarizes the parameter values of each BOF using the nomenclature defined in Fig. (5.3), as well as the nominal value of the main input source, and the battery characteristics.

The battery dynamics in the charging process is emulated by charging a capacitor with a capacitance value of 120 F. The value of the battery capacity has been chosen to ensure the complete charging process in only two seconds, this representing a trade-off between simulating the low-frequency charging protocols dynamics and the high-frequency sliding dynamics in BOF converters. Likewise, Table 5.5 summarizes the control command and controllers for each charging stage. For both CP-CV and CC-CV protocols, the battery voltage controller is the same. Fig. 5.7 shows the input and output current of the LFR charger during start-up, for each module and the total, without a smooth transition control from the initial conditions to the set power, Fig. 5.8 shows the start-up when a soft-start circuit is included. An abrupt start-up generates an overshoot

and a ringing in the output current of the charger during the transient due to the interaction of the output filter and the battery. This produces a power overshoot in the battery, as can be seen in Fig. 5.9. This is particularly important in the case of ultrafast charging, where significant power levels are required, because this peak is twice the desired power delivery. The proposed soft start-up avoids this peak by mitigating the impact of the charging process in the battery and converters.

Table 5.4: Parameters of the standard BOF converter and battery model.

Parameter	**Values**
L_1	100 μH
L_2	100 μH
C	100 μF
Input voltage source V_g	24 V
Battery nominal voltage (CV set point, 80% SOC)	48 V
Battery voltage range (CV set point, 80% SOC)	[28 – 54] V
Nominal battery capacity	60 mAh

Table 5.5: Control command set and controller of the battery charging control in Fig. 5.6

Stage	**Controller**	**Equation**
CC	$k_1(t)$	$1.25\left(1-e^{-0.01t}\right)S$
	C_{i2}	$0.1\frac{s+1000}{s}$
CP	$k_2(t)$	$0.6667\left(1-e^{-0.01t}\right)S$
CV	C_{v_B}	$0.615\frac{s+6667}{s}$

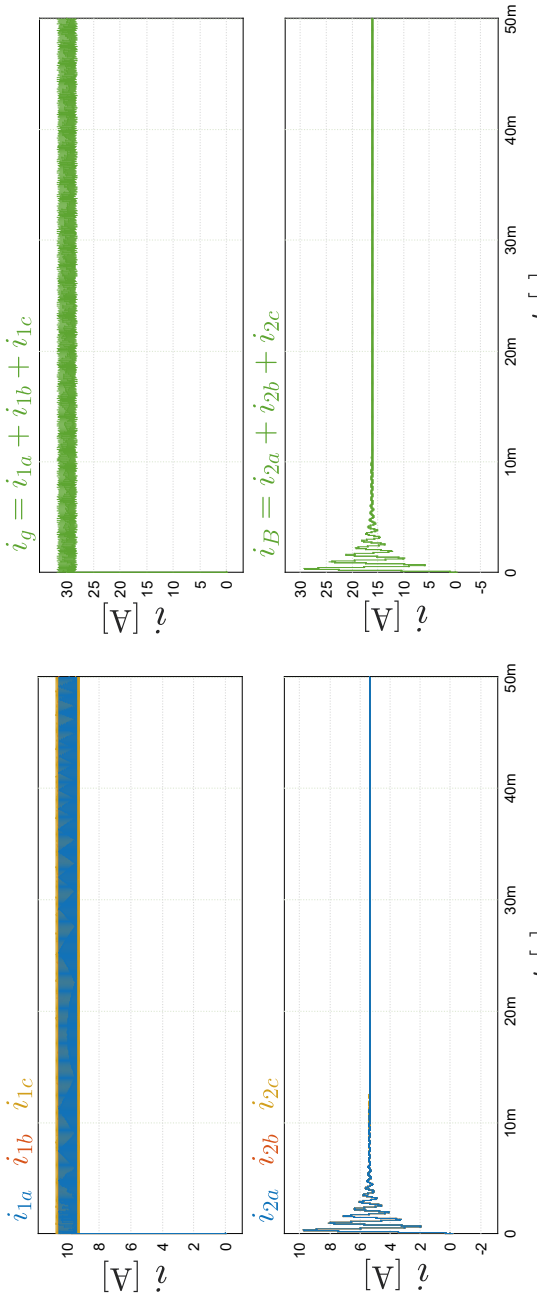

Fig. 5.7: Input and output current waveforms during start-up without soft transient in the LFR battery charger with three BOFs for CP phase. (a) Individual modules, (b) total contribution.

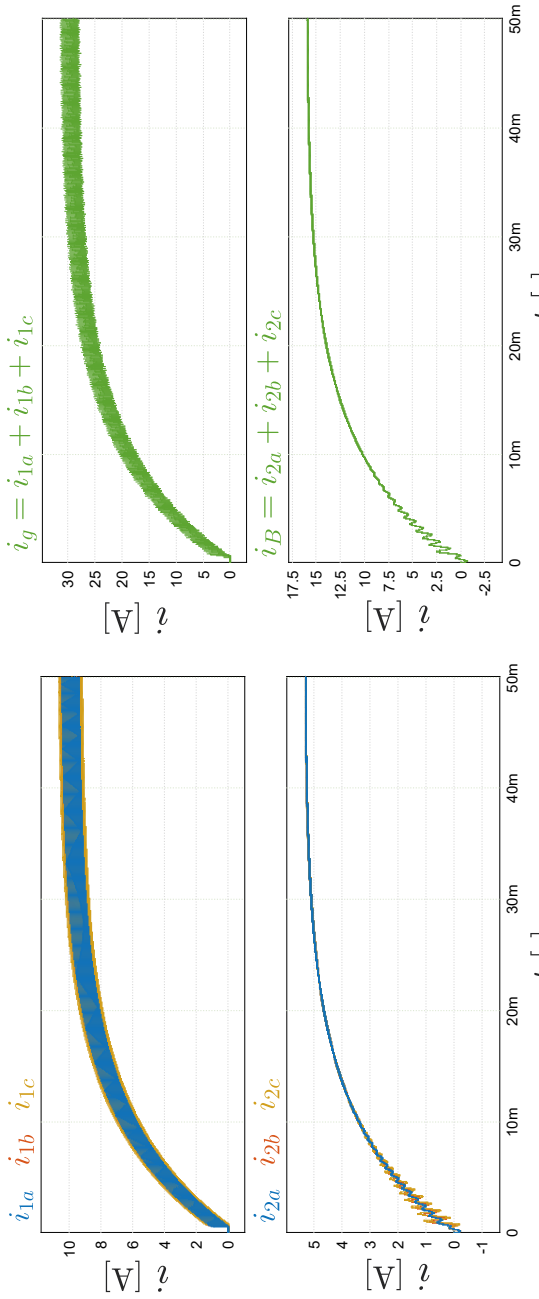

Fig. 5.8: Input and output current waveforms during start-up with soft-start circuit included in the LFR battery charger with three BOFs for CP phase. (a) Individual module, (b) total contribution.

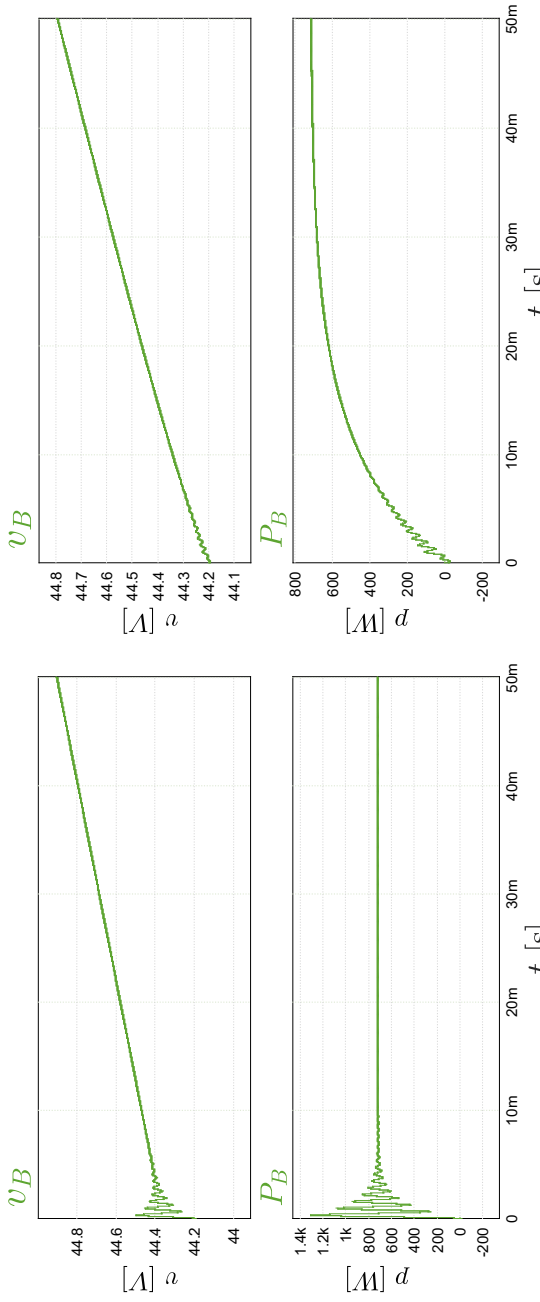

Fig. 5.9: Comparison of the voltage and power of the LFR battery charger for (a) without soft start, and (b) with soft start.

Finally, Figs. (5.10) and (5.11) present the charging process for CP-CV and CC-CV protocols, respectively. The initial battery voltage for all simulation test is 43.8 V, corresponding to a 60% of SOC, and it is charged until a 80% of SOC to 48 V.

In the LFR charger with CP stage, each converter provides 240 W for the battery, with a total power of 720 W and a variable total output current between 15 A and 17 A. In the input port, the total current is 30 A. Just a parasitic resistor of 0.1 Ω in each converter would cause 100W of input losses for this current level, decreasing the system efficiency by 12%.

For the G-gyrator charger a constant output current of 16 A has been calculated, which on average delivers the same power as in the previous case during the CC stage. This means that the delivered power to the battery increases and is higher at the end of the CC than the constant power during CP.

The CV stage is similar for both chargers, with the charging being completed after reaching a minimum value of k(t) in t_f that guarantees the existence of sliding motion in each converter: $k_1(t_f) = 0.016\ S$ and $k_2(t_f) = 0.03\ S$ for G-gyrator and LFR charger type, respectively.

Without taking int account the electrochemistry of the batteries, the simulations indicate that there is no significant difference in the duration of the CC stage with respect to the that of CP, and there is no effect on the subsequent CV stage either.

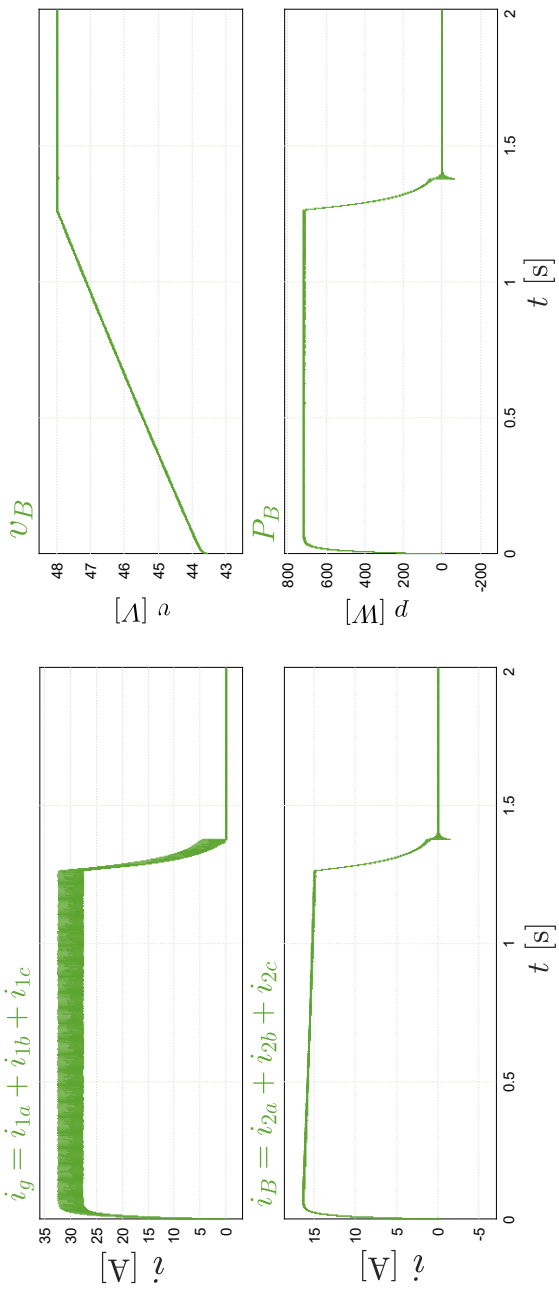

Fig. 5.10: CP-CV protocol with LFR charger type. (a) Input and output current of the charger and (b) voltage and power in the battery

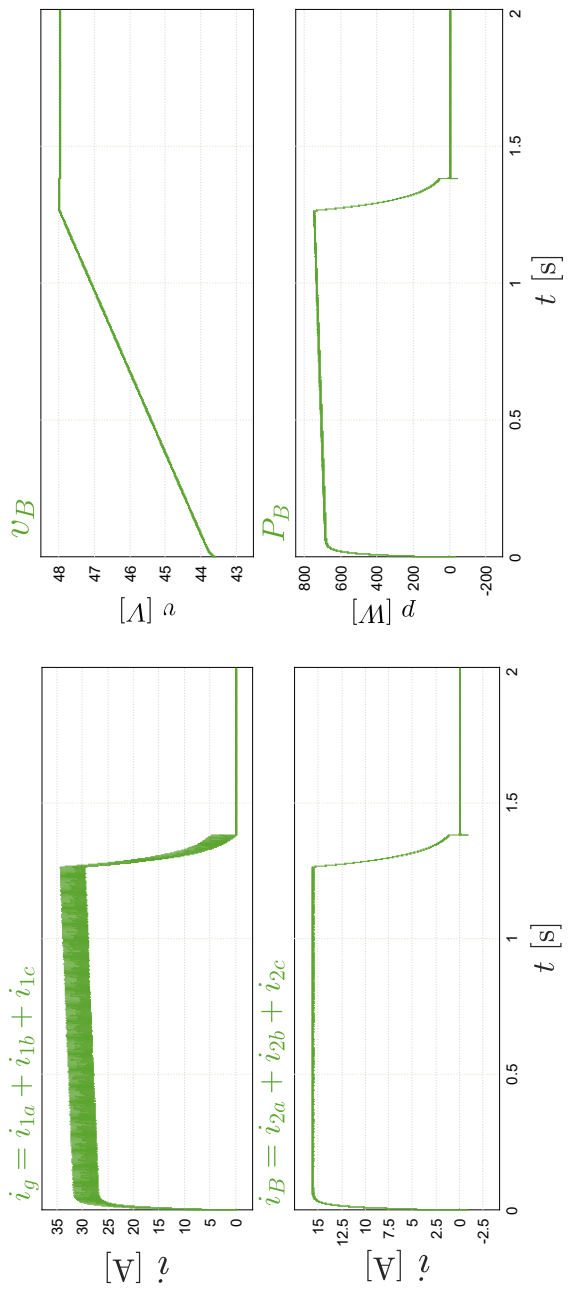

Fig. 5.11: CC-CV protocol with G-gyrator charger type. (a) Input and output current of the charger and (b) voltage and power in the battery.

5.4 SMC-based design of power source with buck converter

In section 5.3 of this chapter, we have demonstrated the versatility of the boost converter with output filter to cope with an static load of battery type while or operating as a current or and power source through an appropriate choice of a control law.

However, from an industrial perspective, BOF is not the best candidate to supply current or power to a battery. The property of reducing gain current respect to the input port forces to increase the converter power losses when large amounts of power are delivered to the battery in ultrafast charging protocols analyzed in this chapter.

It would be more natural to use a buck converter for this purpose but it has the obstacle that it is not possible to apply the LFR synthesis approach for the CP phase; instead, it can be used as a G-gyrator of type I [76] as current source in a CC phase.

Fig.5.12 shows the block diagram of a sliding-mode controlled buck unidirectional power source for battery charging with CP-CV protocol. Transistor Q and diode D are assumed ideal and no parasitics are considered. The model of the battery is illustrated in Fig. 5.13.

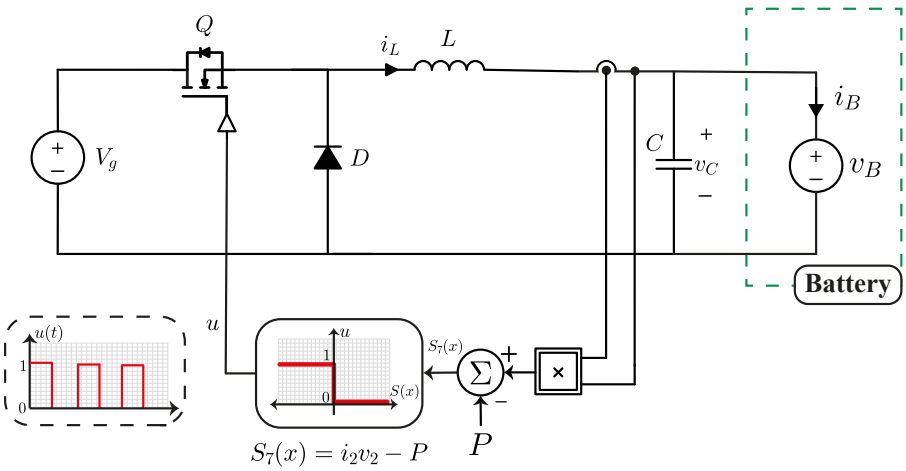

Fig. 5.12: Block diagram of a sliding-mode controlled buck-based unidirectional power source.

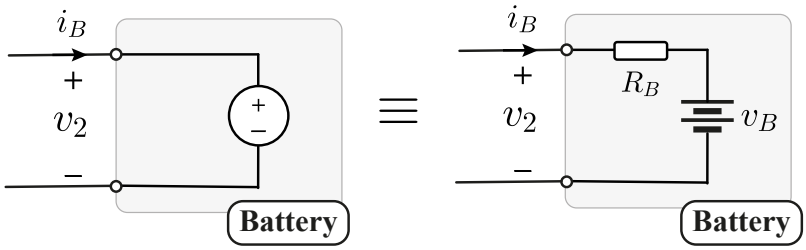

Fig. 5.13: Block diagram of a sliding-mode controlled buck-based unidirectional power source.

With the nomenclature used for the two-port circuit model, the inductor current i_L and capacitor voltage $v_C of$ the buck converter correspond to the output current i_2 and the output voltage v_2, respectively. Thus, the expression of the sliding surface $S_7(x)$ will be given by

$$S_7(x) = i_2 v_2 - P \tag{5.37}$$

The control law to keep the state trajectory switching above and below surface $S_7(x)$ is derived from the conditions for existence of sliding motions.

$$\frac{dS_7(x)}{dt} < 0 \quad \text{if} \quad S_7(x) > 0 \tag{5.38a}$$

$$\frac{dS_7(x)}{dt} > 0 \quad \text{if} \quad S_7(x) < 0 \tag{5.38b}$$

The above conditions are fulfilled when the switching law is given by

$$u = \begin{cases} 0, & \text{if, } S_7(x) > +\Delta \\ 1, & \text{if, } S_7(x) < -\Delta \end{cases} \tag{5.39}$$

5.4.1 State equations

In CCM the converter in Fig. 7 can be described in compact form by the following set of differential equations.

$$\frac{di_2}{dt} = \frac{V_g}{L}u - \frac{v_2}{L} \tag{5.40a}$$

$$\frac{dv_2}{dt} = \frac{i_2}{C} - \frac{v_2 - v_B}{CR_B} \tag{5.40b}$$

5.4.2 Existence of sliding motion

The time-derivate of $S_7(x)$ can be expressed as follows

$$\dot{S}_7\left(x\right) = \frac{V_g v_2 u}{L} - \frac{v_2^2}{L} + \frac{i_2\left(i_2 R_B - v_2 + v_B\right)}{v_2 R_B} \tag{5.41}$$

Imposing the conditions (5.39) in (5.41) leads respectively to expressions (5.42a) and (5.42b).

$$\lim_{S(x)\to 0^+} \dot{S}_7\ \left(x\right)\Big|_{u=0} - \frac{v_2^2}{L} + \frac{i_2\left(i_2 R_B - v_2 + v_B\right)}{v_2 R_B} < 0 \tag{5.42a}$$

$$\lim_{S(x)\to 0^-} \dot{S}_7(x)\Big|_{u=1} = \frac{V_g v_2}{L} - \frac{v_2^2}{L} + \frac{i_2\left(i_2 R_B - v_2 + v_B\right)}{v_2 R_B} > 0 \tag{5.42b}$$

The inequality (5.42a) implies

$$V_g > v_2 \tag{5.43a}$$

$$i_2 > \frac{v_2 - v_B}{R_B} \tag{5.43b}$$

The above constraints are part of the operation of a step-down power converter supplying direct current to the load and are always satisfied under normal operating conditions in the charging process. On the other hand, inequality

(5.42b) when $u = 0$ requires

$$v_{2\ min} > i_{2\ max}\sqrt{\frac{L}{C}} \tag{5.44}$$

5.4.3 Equivalent control and ideal sliding dynamics

In sliding mode, the converter dynamics is subjected to the constraints $S_7(x) = 0$ and $\dot{S}_7(x) = 0$. Therefore, equaling (5.41) to zero leads to the following expression of the equivalent control

$$u_{7\ eq} = \frac{v_2}{V_g} - \frac{Li_2\left(i_2R_B - v_2 + v_B\right)}{CV_g v_2 R_B} \tag{5.45}$$

Introducing expression (5.45)in the converter state equations given by (5.40) will yield the ideal sliding dynamics for the power source given by

$$\frac{di_2}{dt} = -\frac{i_2\left(i_2R_B - v_2 + v_B\right)}{Cv_2R_B} \tag{5.46a}$$

$$\frac{dv_2}{dt} = \frac{P}{Cv_2} - \frac{v_2 - v_B}{CR_B} \tag{5.46b}$$

where $i_2 = P/v_2$. In sliding motion, the order of the system is reduced by one. So, equations (5.46a) and (5.46a) are not independent.

5.4.4 Stability conditions

By equaling to zero equation (5.46a), the EP for the power source is obtained, where the asterisk stands for average value.

$$I_2^* = \frac{V_2^* - V_B^*}{R_B^*} \tag{5.47a}$$

$$U_{7\ eq}^* = \frac{V_2^*}{V_g} \tag{5.47b}$$

Linearizing equation (5.46a) around EP (5.45), the small-signal dynamics of power source is given by

$$\frac{d\tilde{i_2}}{dt} = \frac{\partial}{\partial i_2}\left(-\frac{i_2^3}{PC} + \frac{i_2}{R_B C} - \frac{v_B i_2^2}{P R_B C}\right)\Big|_{X_e} \tilde{i_2} = -\frac{B}{\Lambda}\tilde{i_2} \tag{5.48}$$

With

$$B = V2 * -V_B * 3V2 * -V_B * R_B - P \tag{5.49a}$$

$$[10pt]\Lambda = PR_B \tag{5.49b}$$

Since $\Lambda > 0$, we deduce from (5.48) and (5.49a) that the system will be stable if $B > 0$, which implies a minimum value for V_2^*. Therefore, for stability the follow condition must be satisfied.

$$V_2^* > \frac{2V_B^* + \sqrt{V_B^{*2} + 3PR_B}}{2} \triangleq V_{2\,min}^* \tag{5.50}$$

5.4.5 Battery charging control and simulation results

Fig. 5.14 present the diagram block of a battery charging control based on a power source. The CP phase just required a fixed power set point and does not require a soft start due to the linear behavior of the buck converter.

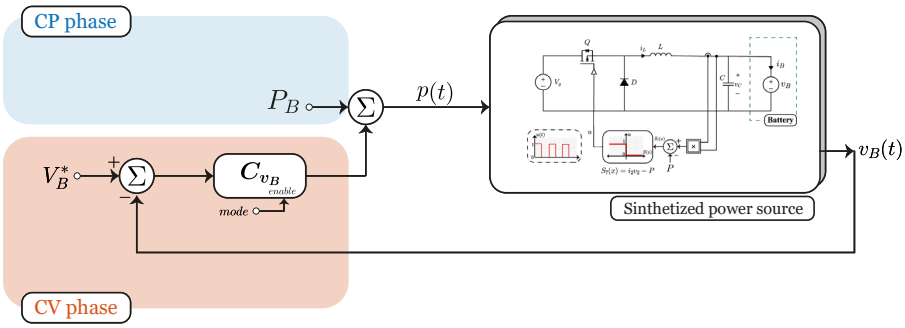

Fig. 5.14: Diagram block of Power source battery charging control.

In CV phase, the battery is regulated by means of the controller C_{v_B}, which operates over the delivered power to the battery.

In sliding motion, the small dynamics of power source based on a buck converter is a first order and is given by (5.51). In terms of control design, classical linear controllers may be used.

$$\frac{d\widetilde{v_2}}{dt} = -\frac{PR_B + V_2^{*2}}{V_2^{*2} R_B}\widetilde{v_2} \tag{5.51}$$

In order to test the power source charger and its control strategy, a simulation in PSIM© for the scheme presented in Fig. 5.14 has been carried out. Table 5.6 summarizes the values of buck converter components corresponding to their definition in Fig. 5.12, as well as the input voltage nominal value source, and the battery characteristics. Likewise for a charger based on canonical elements, the same power set point of 720 W and the controller C_{v_B} in Table 5.2 are used.

Table 5.6: Parameters of the standard BOF converter and battery model.

Parameter	**Values**
L	330 μH
C	1000 μF
Input voltage source V_g	100 V
Battery nominal voltage (CV set point, 80% SOC)	48 V
Battery voltage range (CV set point, 80% SOC)	[28 – 54] V
Nominal battery capacity	60 mAh
R_B	10 $m\Omega$

Fig. 5.15 shows current, voltage and power of the battery during the charging process. The CP phase is similar to that of the LFR charger type. However, the CV phase differs respect to that of the charger based on canonical elements, where the battery current decreases following a first order dynamics. This is due to the surface used for SMC, which is non-linear in the power source-based charger. As a result, the battery current decreases is following a straight line towards zero , and the duration of the CV phase for the power source charger is longer than the corresponding phase in the canonical elements.

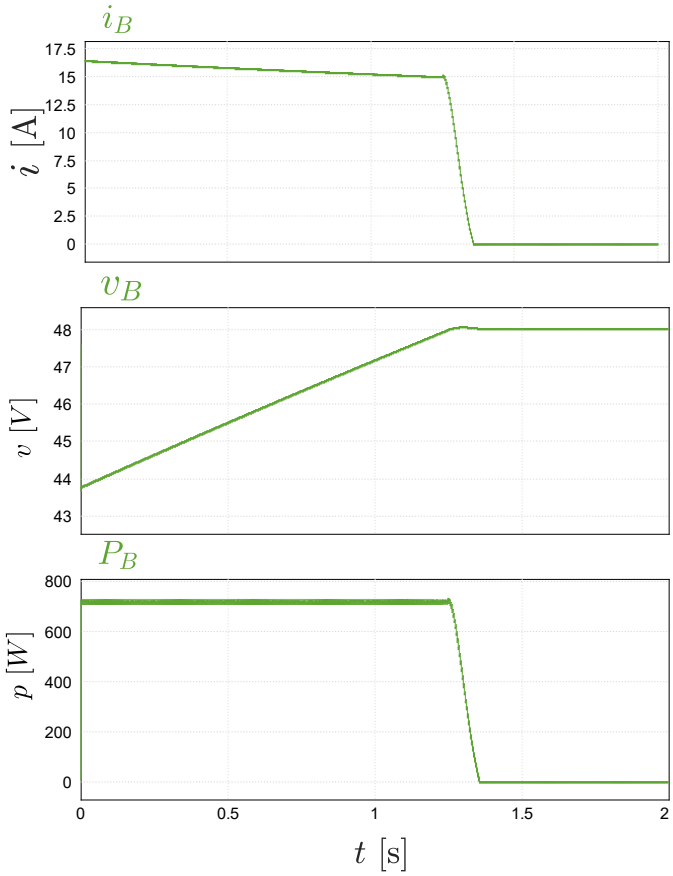

Fig. 5.15: CP-CV protocol with power source-based charger.

5.5 Conclusions

DC-DC switching converter modeling in terms of canonical elements for power processing is not only a conceptual issue, but it is provides a deep insight for power distribution design. Different control approaches can impose different characteristics in the same converter. Thus, based on a boost converter with output filter, the synthesis of the three canonical elements in power processing have been analyzed, i.e. the dc transformer, the power gyrator and the LFR.

In the specific application of battery charging, the BOF converter allows the use of the CC-CV and CP-CV charging protocols from the synthesis of a G-gyrator of type II and a LFR, respectively. In terms of control, the proposed gyrator requires a control loop for each charging stage, while the LFR can operate in open loop at the CP stage, thus decreasing the complexity of the implementation.

The analysis performed on the two elements in the first charging phase, the requirement of a current control loop in the gyrator suggests the possible design of a single LFR for both CP and CC phases, where the power output of the converter is dynamically controlled by output current.

For applications in which the dc bus voltage is higher than the battery voltage , the buck converter is an interesting choice, since it can perform the studied protocols, but at the cost of a more complex control.

UNIVERSITAT ROVIRA I VIRGILI
A SLIDING MODE APPROACH TO CONTROL POWER SINKS AND POWER SOURCES IN DC-DC SWITCHING CONVERTERS
David Alejandro Zambrano Prada

Chapter 6

General Conclusion

Constant power operation or constant power mode is often scattered in many industrial applications. The cascade connection of power converters is one example that leads to the notion of CPL, which is also the relevant feature in electric vehicles operating simultaneously with constant speed and torque. Both examples are referential cases of power sink, in which the supplying converters have to cope with the instability in open loop.

Dually, the concept of power sink is also the way to model PV systems operating at the maximum power point or the procedure to characterize the output of certain power converters whose input port exhibits resistive characteristics ; namely, LFRs.

In an attempt to unify the description of power sinks and power sources out of their natural context, i.e. a one –port device for CPL or a two-port circuit for LFR, this thesis has introduced in chapter 1 the notion of power element transformer (PET), which is a two-port circuit that models a switching converter when a power sink behavior is imposed in the input port or a power source characteristic is forced in the output port.

The thesis has separated the study of supplying a power sink from the analysis of generating a power source at the output port of a switching converter. Hence, two parts have been developed. The first part covers chapters 2 and 3 while the second one corresponds to chapters 4 and 5. The common language along the main body of the manuscript is provided by the sliding-mode control acting equally as voltage regulator, analytical tool for LFR applications or eventually gyrator or PET synthesizer.

It has been shown in chapter 2 that sliding surfaces of polynomial type constitute a simple and reliable alternative for SMC of a boost converter loaded with a CPL. Combining the natural unstable trajectories of the converter in the plane $i_L - v_C$ for ON and OFF states with an appropriate switching law in a polynomial–type sliding surface results in a stable trajectory leading the average dynamics to a desired EP.

From a generic formulation of the surface with the previous features, the analysis of the existing conditions for sliding motions and the study of the subsequent stability in polynomial curves of degree zero, degree one and degree two have demonstrated that all feasible surfaces must exhibit a negative incremental resistance $r(x)\big|_{X_e}$ at the EP smaller than an equivalent resistance imposed by the values of the CPL power, the input voltage and the desired output voltage.

The incremental resistance at the EP is also the main distinctive feature when measuring both static and dynamic performance of the regulated converter as reveals a comparative analysis among five switching functions, namely, an affine function, a current parabola, a voltage parabola, a cross-power hyperbola, and an ellipse. In particular, a conduction loss analysis for a plausible rank of values of the inductor parasitic series resistance has shown that the resulting output voltage steady-state error does not depend of the type of the sliding curve used in the control but it is rather proportional to the inductor current steady-state error, the proportionality constant being the incremental resistance at EP. Regarding the dynamic behavior, the ideal sliding dynamics is a first order system with a time constant proportional to the incremental resistance at EP. The mentioned comparative analysis has demonstrated that quadratic surfaces result in both small inrush current and settling time except the cross-power hyperbola that has presented a low general performance.

A final global assessment that takes into account static and dynamic performance as well as implementation allows concluding that the best polynomial alternative for the sliding surface is the affine function.

Adaptive sliding –mode has been studied in Chapter 3 in an attempt to extend the analysis of polynomial surfaces-based SMC to the case of uncertainty in the power value of the CPL. A linear power estimation consisting in the integral loop of the voltage error satisfies the conditions for existence of sliding motions and stability for an appropriate choice of the polynomial surface coefficients. The small-signal ideal sliding dynamics can be determined by the values of the

incremental resistance at EP and the gain of the power estimator. The addition of power losses in the converter model shows that the error estimation remains below 2% in all cases when normal operating conditions are considered.

Chapters 4 and 5 are devoted to power source realization covering exhaustingly the implementation of LFRs and marginally the design of power gyrators and PETs. Chapter 4 has defined a General Nonlinear Static Load (GNSL) from the observation of the type of load used in classical power electronics equipment (resistor) and in new applications like electric vehicles and microgrids (CPL, CCL and battery).

A realistic scenario in modern power distribution systems is a DC bus supplying a combination of the mentioned loads characterized by GNSL. The design of a boost converter with LFR characteristics in the role of a DC bus has allowed the transference of regulated power to the GNSL. The SMC approach has demonstrated that there is a single equilibrium point, which is unconditionally stable. The particularization of the GNSL in three cases of single load, six cases of couple of loads and four cases of three-load combination has also resulted in a stable equilibrium point in each case. The stability is guaranteed by the active damping introduced by the virtual resistance of the LFR.

The existence of a single stable equilibrium point in the connection of an LFR and a battery disclosed in Chapter 4 has been used to study a charging protocol of the type constant power (CP)-constant voltage (CV) in Chapter 5.

In order to compare on equal basis the standard protocol constant current (CC)-constant voltage (CV) with the new one CP-CV, a boost converter with output filter (BOF) has been selected. Such converter allows the implementation of a power gyrator to impose a constant current at the output and can also behave as LFR. The use of BOF constraints the charging to cases in which the dc bus voltage is smaller than the battery voltage. It has been shown that a DC-to-DC switching converter with loss-free resistor (LFR) behavior is an efficient and reliable solution to impose a CP-CV charging protocol OFFering similar performance to that of the conventional CC-CV procedure.

The solution in the case of dc bus voltage higher than the battery voltage has required a buck converter acting either as PET or as power gyrator. The CP-CV protocol implemented in the PET approach OFFers similar performance than the power gyrator solution for the CC-CV but requires a more complex implementation than that of the LFR in the BOF case.

UNIVERSITAT ROVIRA I VIRGILI
A SLIDING MODE APPROACH TO CONTROL POWER SINKS AND POWER SOURCES IN DC-DC SWITCHING CONVERTERS
David Alejandro Zambrano Prada

Chapter 7

List of Contributions

Journal Articles

Polynomial Sliding Surfaces to Control a Boost Converter with Constant Power Load

Zambrano-Prada, D. A., El Aroudi, A., Vazquez-Seisdedos, L., and Martinez-Salamero, L.

Transactions on Circuits and Systems I: Regular Papers

vol. 70, no. 1, pp. 530–543, January. 2023,

DOI: 10.1109/TCSI.2022.3214297.

Design of Loss-Free Resistors Terminated at a Generic Nonlinear Static Load

O. López-Santos, D. Zambrano-Prada, H. Valderrama-Blavi, A. Cid-Pastor, L. Vázquez-Seisdedos, A. El Aroudi,and L. Martínez-Salamero

Transactions on Circuits and Systems I: Regular Papers

(Accepted)

Conference Articles

Electrical architecture for ultrafast charging station

D. Zambrano-Prada, A. Blanch-Fortuna, J. A. Barrado-Rodrigo, L. Vázquez-Seisdedos, O. López-Santos, A. El Aroudi, and Luis Martinez-Salamero

8th International Electric Vehicle Conference (EVC 2023)

Edinbugh - UK 2023

DOI:

Unidirectional DC-DC Converters for Ultrafast Charging of Electric Vehicles

O. Lopez-Santos, D. Zambrano-Prada, L. Martinez-Salamero, A. El Aroudi, and L. Vazquez-Seisdedos

2023 IEEE International Conference on Electrical Systems for Aircraft, Railway, Ship Propulsion and Road Vehicles and International Transportation Electrification Conference

Venice - Italy 2023

DOI: 10.1109/TCSI.2022.3214297.

Adaptive Sliding Mode Control for a Boost Converter with Constant Power Load

D. Zambrano-Prada, A. El Aroudi, L. Vazquez-Seiszdedos, O. Lopez-Santos, R. Haroun, and L. Martinez-Salamero

IEEE Conference on Power Electronics and Renewable Energy, CPERE 2023

Luxor - Egipt 2023

DOI: 10.1109/CPERE56564.2023.10119573

Superficies de deslizamiento para controlar un convertidor boost con carga de potencia constante

D. Zambrano-Prada, A. El Aroudi, L. Vazquez-Seiszdedos, and L. Martinez-Salamero

XXVIII Seminario Anual de Automatica, Electronica Industrial e Instrumentacion (SAAEI)

LLeida - Spain 2022

DOI:

Arquitectura electrica para una estacion de carga ultrarrapida de baterias: consideraciones generales

D. Zambrano-Prada, A. El Aroudi, H. Valderrama-Blavi, J. Barrado, F. Gonzalez, L. Martinez-Salamero, F. Guinjoan, J. Garrido

XXVIII Seminario Anual de Automatica, Electronica Industrial e Instrumentacion (SAAEI)
Ciudad Real - Spain 2021
DOI:

UNIVERSITAT ROVIRA I VIRGILI
A SLIDING MODE APPROACH TO CONTROL POWER SINKS AND POWER SOURCES IN DC-DC SWITCHING CONVERTERS
David Alejandro Zambrano Prada

References

[1] R. W. Brockett and J. R. Wood, "Applications of lie group theory to nonlinear network problems," *Supplement to IEEE international symposium on Circuit theory*, pp. 1–11, Apr. 1974.

[2] M. Belkhayat, R. Cooley, and A. Witulski, "Large signal stability criteria for distributed systems with constant power loads," *PESC Record - IEEE Annual Power Electronics Specialists Conference*, vol. 2, pp. 1333–1338, 1995, ISSN: 02759306. DOI: 10.1109/PESC.1995.474987.

[3] A. Emadi and M. Ehsani, "Dynamics and control of multi-converter dc power electronic systems," *PESC Record - IEEE Annual Power Electronics Specialists Conference*, vol. 1, pp. 248–253, 2001, ISSN: 02759306. DOI: 10.1109/PESC.2001.954028.

[4] A. Emadi, A. Khaligh, C. H. Rivetta, and G. A. Williamson, "Constant power loads and negative impedance instability in automotive systems: Definition, modeling, stability, and control of power electronic converters and motor drives," *IEEE Transactions on Vehicular Technology*, vol. 55, pp. 1112–1125, 4 Jul. 2006, ISSN: 00189545. DOI: 10.1109/TVT.2006.877483.

[5] S. C. Smithson and S. S. Williamson, "Constant power loads in more electric vehicles - an overview," *IECON Proceedings (Industrial Electronics Conference)*, pp. 2914–2922, 2012. DOI: 10.1109/IECON.2012.6389432.

[6] F. D. Moralez, "Mitigación del efecto desestabilizador de la cpl en el sistema de conversión de potencia de un vehículo eléctrico mediante compensación activa basada en lfr," Universidat Rovira i Virgili, 2019.

[7] R. W. Erickson and D. Maksimović, *Fundamentals of Power Electronics*, 3rd ed. Springer International Publishing, 2020, ISBN: 978-3-030-43881-4. DOI: 10.1007/978-3-030-43881-4.

[8] T. Instruments, "Understanding inverting buck-boost power stages in switch mode power supplies application report understanding inverting buck-boost power stages in switch mode power supplies," Texas Instruments, 1999.

[9] S. Singer and R. W. Erickson, "Canonical modeling of power processing circuits based on the popi concept," *IEEE Transactions on Power Electronics*, vol. 7, pp. 37–43, 1 1992, ISSN: 08858993. DOI: 10.1109/63.124575.

[10] S. Singer, "Realization of loss-free resistive elements," *IEEE Transactions on Circuits and Systems*, vol. 37, pp. 54–60, 1 1990, ISSN: 00984094. DOI: 10.1109/31.45691.

[11] I. Barbi, "Series loss-free resistor: Analysis, realization, and applications," *IEEE Transactions on Power Electronics*, vol. 36, pp. 12 857–12 866, 11 Nov. 2021, ISSN: 19410107. DOI: 10.1109/TPEL.2021.3082509.

[12] B. A. Martinez-Trevino, A. El Aroudi, A. Cid-Pastor, G. Garcia, and L. Martinez-Salamero, "Synthesis of constant power loads using switching converters under sliding-mode control," *IEEE Transactions on Circuits and Systems I: Regular Papers*, vol. 68, pp. 524–535, 1 Jan. 2021, ISSN: 15580806. DOI: 10.1109/TCSI.2020.3031332.

[13] A. Cid-Pastor, L. Martinez-Salamero, A. El Aroudi, R. Giral, J. Calvente, and R. Leyva, "Synthesis of loss-free resistors based on sliding-mode control and its applications in power processing," *Control Engineering Practice*, vol. 21, pp. 689–699, 5 May 2013, ISSN: 0967-0661. DOI: 10.1016/J.CONENGPRAC.2012.02.007.

[14] R. Bonache-Samaniego, C. Olalla, L. Martínez-Salamero, and H. Valderrama-Blavi, "Design of self-oscillating resonant converters based on a variable structure systems approach," *IET Power Electronics*, vol. 9, pp. 111–119, 1 Jan. 2016, ISSN: 1755-4543. DOI: 10.1049/IET-PEL.2014.0964.

[15] R. Bonache-Samaniego, C. Olalla, H. Valderrama-Blavi, and L. Martínez-Salamero, "Analysis and design of self-oscillating resonant converters with loss-free resistor characteristics," *Energies 2020, Vol. 13, Page 3743*, vol. 13, p. 3743, 14 Jul. 2020, ISSN: 1996-1073. DOI: 10.3390/EN13143743.

[16] L. A. Kumar, S. A. Alexander, and R. Madhuvanthani, *Power Electronic Converters for Solar Photovoltaic Systems*. Elsevier, Nov. 2020, pp. 1–386, ISBN: 978-0-12-822730-5. DOI: 10.1016/C2019-0-04270-7.

[17] T. Esram and P. L. Chapman, "Comparison of photovoltaic array maximum power point tracking techniques," *IEEE Transactions on Energy Conversion*, vol. 22, pp. 439–449, 2 Jun. 2007, ISSN: 08858969. DOI: 10.1109/TEC.2006.874230.

[18] C. Cabal, L. Martínez-Salamero, L. Séguier, C. Alonso, and F. Guinjoan, "Maximum power point tracking based on sliding-mode control for output-series connected converters in photovoltaic systems," *IET Power Electronics*, vol. 7, pp. 914–923, 4 Apr. 2014, ISSN: 1755-4543. DOI: 10.1049/IET-PEL.2013.0348.

[19] R. Haroun, A. El Aroudi, A. Cid-Pastor, E. Vidal-Idiarte, H. Valderrama-Blavi, and L. Martinez-Salamero, "Modelling and control of modular dc-nanogrids based on loss-free resistors," *IEEE Access*, vol. 8, pp. 33 305–33 317, 2020, ISSN: 21693536. DOI: 10.1109/ACCESS.2020.2974036.

[20] J. G. J. Shi V. Utkin, *Sliding Modes in Electromechanical Systems*, 2nd editio. London, U.K.: Taylor and Francis, 2009, ISBN: 9781420065602.

[21] B. A. Martinez-Treviño, A. El Aroudi, E. Vidal-Idiarte, A. Cid-Pastor, and L. Martinez-Salamero, "Sliding-mode control of a boost converter under constant power loading conditions," *IET Power Electronics*, vol. 12, pp. 521–529, 3 Mar. 2019, ISSN: 1755-4543. DOI: 10.1049/IET-PEL.2018.5098.

[22] S. Srdic and S. Lukic, "Toward extreme fast charging: Challenges and opportunities in directly connecting to medium-voltage line," *IEEE Electrification Magazine*, vol. 7, pp. 22–31, 1 Mar. 2019, ISSN: 23255889. DOI: 10.1109/MELE.2018.2889547.

[23] C. Y. Wang, T. Liu, X. G. Yang, *et al.*, "Fast charging of energy-dense lithium-ion batteries," *Nature 2022 611:7936*, vol. 611, pp. 485–490, 7936 Oct. 2022, ISSN: 1476-4687. DOI: 10.1038/s41586-022-05281-0.

[24] A. Tomaszewska, Z. Chu, X. Feng, *et al.*, "Lithium-ion battery fast charging: A review," *eTransportation*, vol. 1, p. 100 011, Aug. 2019, ISSN: 2590-1168. DOI: 10.1016/J.ETRAN.2019.100011.

[25] A. Khaligh, A. M. Rahimi, and A. Emadi, "Modified pulse-adjustment technique to control dc/dc converters driving variable constant-power loads," *IEEE Transactions on Industrial Electronics*, vol. 55, pp. 1133–1146, 3 Mar. 2008, ISSN: 02780046. DOI: 10.1109/TIE.2007.909757.

[26] A. M. Rahimi and A. Emadi, "Discontinuous-conduction mode dc/dc converters feeding constant-power loads," *IEEE Transactions on Industrial Electronics*, vol. 57, pp. 1318–1329, 4 Apr. 2010, ISSN: 02780046. DOI: 10.1109/TIE.2009.2029514.

[27] A. M. Rahimi and A. Emadi, "Active damping in dc/dc power electronic converters: A novel method to overcome the problems of constant power loads," *IEEE Transactions on Industrial Electronics*, vol. 56, pp. 1428–1439, 5 2009, ISSN: 02780046. DOI: 10.1109/TIE.2009.2013748.

[28] Y. Li, K. R. Vannorsdel, A. J. Zirger, M. Norris, and D. Maksimovic, "Current mode control for boost converters with constant power loads," *IEEE Transactions on Circuits and Systems I: Regular Papers*, vol. 59, pp. 198–206, 1 2012, ISSN: 15498328. DOI: 10.1109/TCSI.2011.2161364.

[29] B. Choi, B. H. Cho, and S. S. Hong, "Dynamics and control of dc-to-dc converters driving other converters downstream," *IEEE Transactions on Circuits and Systems I: Fundamental Theory and Applications*, vol. 46, pp. 1240–1248, 10 Oct. 1999, ISSN: 10577122. DOI: 10.1109/81.795837.

[30] S. Arora, P. Balsara, and D. Bhatia, "Input-output linearization of a boost converter with mixed load (constant voltage load and constant power load)," *IEEE Transactions on Power Electronics*, vol. 34,

pp. 815–825, 1 2018, ISSN: 08858993. DOI: 10.1109/TPEL.2018.2813324.

[31] G. Sulligoi, D. Bosich, G. Giadrossi, L. Zhu, M. Cupelli, and A. Monti, "Multiconverter medium voltage dc power systems on ships: Constant-power loads instability solution using linearization via state feedback control," *IEEE Transactions on Smart Grid*, vol. 5, pp. 2543–2552, 5 Sep. 2014, ISSN: 19493053. DOI: 10.1109/TSG.2014.2305904.

[32] B. A. Martinez-Trevino, A. El Aroudi, A. Cid-Pastor, and L. Martinez-Salamero, "Nonlinear control for output voltage regulation of a boost converter with a constant power load," *IEEE Transactions on Power Electronics*, vol. 34, pp. 10 381–10 385, 11 Nov. 2019, ISSN: 19410107. DOI: 10.1109/TPEL.2019.2913570.

[33] C. N. Onwuchekwa and A. Kwasinski, "Analysis of boundary control for buck converters with instantaneous constant-power loads," *IEEE Transactions on Power Electronics*, vol. 25, pp. 2018–2032, 8 2010, ISSN: 08858993. DOI: 10.1109/TPEL.2010.2045658.

[34] C. N. Onwchekwa and A. Kwasinski, "Analysis of boundary control for boost and buck-boost converters in distributed power architectures with constant-power loads," *Conference Proceedings - IEEE Applied Power Electronics Conference and Exposition - APEC*, pp. 1816–1823, 2011. DOI: 10.1109/APEC.2011.5744843.

[35] L. Benadero, R. Cristiano, D. J. Pagano, and E. Ponce, "Nonlinear analysis of interconnected power converters: A case study," *IEEE Journal on Emerging and Selected Topics in Circuits and Systems*, vol. 5, pp. 326–335, 3 Sep. 2015, ISSN: 21563357. DOI: 10.1109/JETCAS.2015.2462017.

[36] S. Singh and D. Fulwani, "Constant power loads: A solution using sliding mode control," *IECON Proceedings (Industrial Electronics Conference)*, pp. 1989–1995, Feb. 2014. DOI: 10.1109/IECON.2014.7048775.

[37] S. Singh, D. Fulwani, and V. Kumar, "Robust sliding-mode control of dc/dc boost converter feeding a constant power load," *IET Power Electronics*, vol. 8, pp. 1230–1237, 7 Jul. 2015, ISSN: 1755-4543. DOI: 10.1049/IET-PEL.2014.0534.

[38] S. Singh, V. Kumar, and D. Fulwani, "Mitigation of destabilising effect of cpls in island dc micro-grid using non-linear control," *IET Power Electronics*, vol. 10, pp. 387–397, 3 Mar. 2017, ISSN: 1755-4543. DOI: 10.1049/IET-PEL.2015.0520.

[39] B. A. Unni and P. R. Kumar, "Higher order sliding mode control based duty-ratio controller for the dc/dc buck converter with constant power loads," *International Conference on Electrical, Electronics, and Optimization Techniques, ICEEOT 2016*, pp. 656–661, Nov. 2016. DOI: 10.1109/ICEEOT.2016.7754763.

[40] A. El Aroudi, B. A. Martínez-Treviño, E. Vidal-Idiarte, and A. Cid-Pastor, "Fixed switching frequency digital sliding-mode control of dc-dc power supplies loaded by constant power loads with inrush current limitation capability," *Energies 2019, Vol. 12, Page 1055*, vol. 12, p. 1055, 6 Mar. 2019, ISSN: 1996-1073. DOI: 10.3390/EN12061055.

[41] L. Martinez-Salamero, *Sliding Mode Control of Power Converters in Renewable Energy Systems*. ISBN: 9783039280988.

[42] L. Benadero, A. El Aroudi, E. Toribio, G. Olivar, and L. Martinez-Salamero, "Characteristic curves for analyzing limit cycle behaviour in switching converters," *Electronics Letters*, vol. 35, pp. 687–689, 9 Apr. 1999, ISSN: 00135194. DOI: 10.1049/EL:19990492.

[43] H. Sira-Ramirez, "Sliding motions in bilinear switched networks," *IEEE Transactions on Circuits and Systems*, vol. 34, pp. 919–933, 8 1987, ISSN: 00984094. DOI: 10.1109/TCS.1987.1086242.

[44] V. Repecho, N. Masclans, and D. Biel, "A comparative study of terminal and conventional sliding-mode startup peak current controls for a synchronous buck converter," *IEEE Journal of Emerging and Selected Topics in Power Electronics*, vol. 9, pp. 197–205, 1 Feb. 2021, ISSN: 21686785. DOI: 10.1109/JESTPE.2019.2960924.

[45] L. Martinez-Salamero, G. Garcia, M. Orellana, C. Lahore, and B. Estibals, "Start-up control and voltage regulation in a boost converter under sliding-mode operation," *IEEE Transactions on Industrial Electronics*, vol. 60, pp. 4637–4649, 10 2013, ISSN: 02780046. DOI: 10.1109/TIE.2012.2210375.

[46] H. Chen, H. Kim, R. Erickson, and D. Maksimovic, "Electrified automotive powertrain architecture using composite dc-dc converters," *IEEE Transactions on Power Electronics*, vol. 32, pp. 98–116, 1 Jan. 2017, ISSN: 08858993. DOI: 10.1109/TPEL.2016.2533347.

[47] M. Boukerdja, A. Chouder, L. Hassaine, B. O. Bouamama, W. Issa, and K. Louassaa, "H∞ based control of a dc/dc buck converter feeding a constant power load in uncertain dc microgrid system," *ISA Transactions*, vol. 105, pp. 278–295, Oct. 2020, ISSN: 0019-0578. DOI: 10.1016/J.ISATRA.2020.05.031.

[48] W. He, R. Ortega, J. E. Machado, and S. Li, "An adaptive passivity-based controller of a buck-boost converter with a constant power load," *Asian Journal of Control*, vol. 21, pp. 581–595, 1 Jan. 2019, ISSN: 19346093. DOI: 10.1002/asjc.1751.

[49] W. He, C. A. Soriano-Rangel, R. Ortega, A. Astolfi, F. Mancilla-David, and S. Li, "Energy shaping control for buck–boost converters with unknown constant power load," *Control Engineering Practice*, vol. 74, pp. 33–43, May 2018, ISSN: 09670661. DOI: 10.1016/j.conengprac.2018.02.006.

[50] W. He, M. M. Namazi, and J. M. Guerrero, "Adaptive energy-based control for buck converter with a class of nonlinear loads," *IEEE Transactions on Circuits and Systems II: Express Briefs*, pp. 1–1, May 2022, ISSN: 1549-7747. DOI: 10.1109/TCSII.2022.3176258.

[51] W. He, M. M. Namazi, H. R. Koofigar, M. A. Amirian, and J. M. Guerrero, "Voltage regulation of buck converter with constant power load: An adaptive power shaping control," *Control Engineering Practice*, vol. 115, p. 104 891, Oct. 2021, ISSN: 09670661. DOI: 10.1016/j.conengprac.2021.104891.

[52] W. He, M. M. Namazi, H. R. Koofigar, M. A. Amirian, and F. Blaabjerg, "Stabilization of dc–dc buck converter with unknown constant power load via passivity-based control plus proportion-integration," *IET Power Electronics*, vol. 14, pp. 2597–2609, 16 Dec. 2021, ISSN: 1755-4543. DOI: 10.1049/PEL2.12205.

[53] W. He, Y. Shang, M. M. Namazi, and R. Ortega, "Adaptive sensorless control for buck converter with constant power load," *Control Engineering Practice*, vol. 126, p. 105 237, Sep. 2022, ISSN: 0967-0661. DOI: 10.1016/J.CONENGPRAC.2022.105237.

[54] Q. Xu, Y. Yan, C. Zhang, T. Dragicevic, and F. Blaabjerg, "An offset-free composite model predictive control strategy for dc/dc buck converter feeding constant power loads," *IEEE Transactions on Power Electronics*, vol. 35, pp. 5331–5342, 5 May 2020, ISSN: 19410107. DOI: 10.1109/TPEL.2019.2941714.

[55] C. Zheng, T. Dragicevic, J. Zhang, R. Chen, and F. Blaabjerg, "Composite robust quasi-sliding mode control of dc-dc buck converter with constant power loads," *IEEE Journal of Emerging and Selected Topics in Power Electronics*, vol. 9, pp. 1455–1464, 2 Apr. 2021, ISSN: 21686785. DOI: 10.1109/JESTPE.2020.3021942.

[56] W. He and R. Ortega, "Design and implementation of adaptive energy shaping control for dc-dc converters with constant power loads," *IEEE Transactions on Industrial Informatics*, vol. 16, pp. 5053–5064, 8 Aug. 2020, ISSN: 19410050. DOI: 10.1109/TII.2019.2953694.

[57] M. Hassan, C. L. Su, F. Z. Chen, and K. Y. Lo, "Adaptive passivity-based control of a dc-dc boost power converter supplying constant power and constant voltage loads," *IEEE Transactions on Industrial Electronics*, vol. 69, pp. 6204–6214, 6 Jun. 2022, ISSN: 15579948. DOI: 10.1109/TIE.2021.3086723.

[58] Q. Xu, C. Zhang, C. Wen, and P. Wang, "A novel composite nonlinear controller for stabilization of constant power load in dc microgrid," *IEEE Transactions on Smart Grid*, vol. 10, pp. 752–761, 1 Sep. 2017, ISSN: 1949-3053. DOI: 10.1109/TSG.2017.2751755.

[59] B. A. Martinez-Trevino, A. E. Aroudi, H. Valderrama-Blavi, A. Cid-Pastor, E. Vidal-Idiarte, and L. Martinez-Salamero, "Pwm nonlinear control with load power estimation for output voltage regulation of a boost converter with constant power load," *IEEE Transactions on Power Electronics*, vol. 36, pp. 2143–2153, 2 Feb. 2021, ISSN: 19410107. DOI: 10.1109/TPEL.2020.3008013.

[60] A. Marcos-Pastor, E. Vidal-Idiarte, A. Cid-Pastor, and L. Martínez-Salamero, "Loss-free resistor-based power factor correction using a semi-bridgeless boost rectifier in sliding-mode control," *IEEE Transactions on Power Electronics*, vol. 30, pp. 5842–5853, 10 Oct. 2015, ISSN: 08858993. DOI: 10.1109/TPEL.2014.2369431.

[61] N. Rathore, D. Fulwani, A. K. Rathore, and A. R. Gautam, "Adaptive sliding mode based loss-free resistor for power-factor correction application," *IEEE Transactions on Industry Applications*, vol. 55, pp. 4332–4343, 4 Jul. 2019, ISSN: 19399367. DOI: 10.1109/TIA.2019.2912799.

[62] C. Y. Chan, "Power factor correction based on adaptive modified current-mode control approach," *IEEE Transactions on Circuits and Systems II: Express Briefs*, vol. 69, pp. 1462–1466, 3 Mar. 2022, ISSN: 15583791. DOI: 10.1109/TCSII.2021.3119705.

[63] O. Lopez-Santos, G. Garcia, L. Martinez-Salamero, *et al.*, "Analysis, design, and implementation of a static conductance-based mppt method," *IEEE Transactions on Power Electronics*, vol. 34, pp. 1960–1979, 2 Feb. 2019, ISSN: 08858993. DOI: 10.1109/TPEL.2018.2835814.

[64] J. A. Garriga-Castillo, H. Valderrama-Blavi, J. A. Barrado-Rodrigo, and Àngel Cid-Pastor, "Analysis of sliding-mode controlled impedance matching circuits for inductive harvesting devices," *Energies 2019, Vol. 12, Page 3858*, vol. 12, p. 3858, 20 Oct. 2019, ISSN: 1996-1073. DOI: 10.3390/EN12203858.

[65] O. López-Santos, L. Martínez-Salamero, G. García, H. Valderrama-Blavi, and D. O. Mercuri, "Efficiency analysis of a sliding-mode controlled quadratic boost converter," *IET Power Electronics*, vol. 6, pp. 364–373, 2 Feb. 2013, ISSN: 1755-4543. DOI: 10.1049/IET-PEL.2012.0417.

[66] D. A. Zambrano-Prada, A. El Aroudi, L. Vázquez-Seisdedos, and L. Martínez-Salamero, "Polynomial sliding surfaces to control a boost converter with constant power load," *IEEE Transactions on Circuits and Systems I: Regular Papers*, vol. 70, no. 1, pp. 530–543, 2023. DOI: 10.1109/TCSI.2022.3214297.

[67] G. Tamai, "What are the hurdles to full vehicle electrification? [technology leaders]," *IEEE Electrification Magazine*, vol. 7, pp. 5–11, 1 Mar. 2019, ISSN: 23255889. DOI: 10.1109/MELE.2018.2889544.

[68] J. Jiang and C. Zhang, "Fundamentals and application of lithium-ion batteries in electric drive vehicles," *Fundamentals and Application of Lithium-ion Batteries in Electric Drive Vehicles*, pp. 1–280, Jan. 2015. DOI: 10.1002/9781118414798.

[69] C. Chen, Z. Wei, and A. C. Knoll, "Charging optimization for li-ion battery in electric vehicles: A review," *IEEE Transactions on Transportation Electrification*, vol. 8, pp. 3068–3089, 3 Sep. 2022, ISSN: 23327782. DOI: 10.1109/TTE.2021.3135525.

[70] Z. Guo, B. Y. Liaw, X. Qiu, L. Gao, and C. Zhang, "Optimal charging method for lithium ion batteries using a universal voltage protocol accommodating aging," *Journal of Power Sources*, vol. 274, pp. 957–964, Jan. 2015, ISSN: 0378-7753. DOI: 10.1016/J.JPOWSOUR.2014.10.185.

[71] M. Brenna, F. Foiadelli, C. Leone, and M. Longo, "Electric vehicles charging technology review and optimal size estimation," *Journal of Electrical Engineering and Technology*, vol. 15, pp. 2539–2552, 6 Nov. 2020, ISSN: 20937423. DOI: 10.1007/S42835-020-00547-X/TABLES/3.

[72] O. Lopez-Santos, D. Zambrano-Prada, L. Martinez-Salamero, A. E. Aroudi, and L. Vazquez-Seisdedos, "Unidirectional dc-dc converters for ultrafast charging of electric vehicles," *2023 IEEE International Conference on Electrical Systems for Aircraft, Railway, Ship Propulsion and Road Vehicles and International Transportation Electrification Conference, ESARS-ITEC 2023*, 2023. DOI: 10.1109/ESARS-ITEC57127.2023.10114830.

[73] S. ĆUK and R. D. Middlebrook, "Advances in switched-mode power conversion part i," *IEEE Transactions on Industrial Electronics*, vol. IE-30, pp. 10–19, 1 1983, ISSN: 15579948. DOI: 10.1109/TIE.1983.356697.

[74] S. Singer, "Gyrators application in power processing circuits," *IEEE Transactions on Industrial Electronics*, vol. IE-34, pp. 313–318, 3 1987, ISSN: 15579948. DOI: 10.1109/TIE.1987.350978.

[75] S. Singer, "Application of 'loss-free resistors' in power processing circuits," *PESC Record - IEEE Annual Power Electronics Specialists Conference*, vol. 2, pp. 843–846, 1989, ISSN: 02759306. DOI: 10.1109/PESC.1989.48568.

[76] A. Cid-Pastor, L. Martinez-Salamero, C. Alonso, G. Schweitz, J. Calvente, and S. Singer, "Classification and synthesis of power gyrators," *IEE Proceedings: Electric Power Applications*, vol. 153, pp. 802–808, 6 2006, ISSN: 13502352. DOI: 10.1049/IP-EPA:20050413.

UNIVERSITAT
ROVIRA i VIRGILI